# Supramolecular Structure of Monohydroxy Alcohols

**Dissertation**
zur Erlangung des Doktorgrades der Naturwissenschaften
der Fakultät Physik der Technischen Universität Dortmund

vorgelegt von
**Thomas Büning**
geboren in Haltern am See

Oktober 2016

1. Gutachter : Prof. Dr. Metin Tolan

2. Gutachter : Prof. Dr. Roland Böhmer

# Contents

# Chapter 1

# Introduction

Hydrogen bonds (H-bonds) are essential for the microscopic structure of e.g. proteins, water, and alcohols and of vital importance for any living organism. For example, proteins are stabilized by H-bonds and their interaction with water molecules governs their functionality. Although water is a simple molecule, it has a surprisingly complex phase diagram. Among others, water has an anomalously large dielectric constant which is exploited in microwave ovens. It has been shown recently, that this can be seen in analogy to the Debye-like absorption peak of monohydroxy alcohols (MAs).

Alcohols are used as solvents and are essential in many industrial processes. They have been studied from the early beginning of x-ray science. Furthermore, they are used as a model system on a medium complexity level between huge macromolecules and water. Here, MAs allow studying two fundamental interactions: the interplay of H-bonds and steric hindrance of alkyl chains. Especially, the strong electrical absorption, distinguishing water, and MAs from most other liquids, asks for an explanation on a molecular level. This question is simplified with MAs since fewer H-bonds per molecule are possible, resulting in structures and dynamics that are dependent on both hydrogen bonding and steric hindrance. Nevertheless, insights into the microscopic structure formation mechanisms of MAs might help to rationalize the behavior of other H-bonded liquids as well. It is already known that H-bonds form and stabilize different kinds of supramolecular structures beyond the first shell of neighbors. This structuring on a larger length scale than in non-associating liquids is manifold because of the complex interplay of hydrogen bonding and steric screening, which has not been understood well so far and is still being critically discussed.

The focus of this thesis lies on investigations of structuring in MAs employing different x-ray scattering techniques such as x-ray diffraction and x-ray Raman scattering. The medium range order causes a prepeak on the low momentum transfer side of the main diffraction peak of the static structure factor that also appears in other amorphous materials. These prepeaks yield unique information about supramolecular structures in MAs, mixtures of MAs and in mixtures of MAs with halogen alkanes. Besides, the temperature and pressure dependence of the Debye process in MAs has raised questions about how H-bonds stabilize structures at extreme conditions. X-ray diffraction can

contribute to this field of science since it is possible to learn something about different supramolecular topologies and characteristic length scales in MAs. These insights are valuable to complement measurements conducted with other techniques, such as dielectric spectroscopy, nuclear magnetic resonance and others, and to test results from molecular dynamic simulations. Moreover, the dynamic structure factors of several MAs were gained by x-ray Raman scattering at the oxygen K-edge to obtain additional information about the H-bond network.

An ultimate goal in the study of H-bonded liquids is to observe the forming and breaking of supramolecular structures on a femtosecond timescale. This asks for a new kind of light source delivering highly coherent hard x-rays with a short pulse length and extraordinary brilliance. A machine fulfilling these requirements in principle is the free-electron laser for hard x-rays set up in Hamburg at DESY. To achieve femtosecond time scales an extremely fast sample injection system, delivering a very thin sample of a few microns, is necessary. Inelastic scattering methods established at synchrotron light sources that require scanning of the incident photon energy, like x-ray Raman scattering, are more difficult to conduct at free-electron laser light sources due to the fixed energy of the produced photons. Therefore, completely new experimental techniques have to be established. A chance to overcome this problem is employing a dispersive von Hamos spectrometer. A Combination of these two concepts allows bringing x-ray Raman scattering on liquid sample systems to FELs. One possibility to gain a fast liquid jet with a sufficiently small thickness is a *Microliquids FlatJet* system. This device generates a thin and flat liquid sheet by colliding two cylindrical liquid jets. Such a device was purchased, characterized and tested. Moreover, first test measurements using the von Hamos spectrometer and the liquid jet system simultaneously at synchrotron light sources are presented in this thesis.

The chapters of this thesis are ordered as follows:

- First, MAs with the focus on hydrogen bonding and the Debye process are introduced.

- In chapter 3 a short review on x-ray diffraction and x-ray Raman scattering on liquid alcohols is given.

- The experimental setups are presented in chapter 4.

- The results are discussed in chapter 5.

- Finally, a fast liquid jet system allowing to perform time-resolved inelastic x-ray scattering methods on fluids is introduced in chapter 6.

# Chapter 2

# Sample system - Monohydroxy alcohols

## 2.1 Hydrogen bonding in monohydroxy alcohols

The hydrogen bond is defined as „an attractive interaction between a hydrogen atom from a molecule or a molecular fragment X–H in which X is more electronegative than H, and an atom or a group of atoms in the same or a different molecule, in which there is evidence of bond formation" (Arunan et al., 2011). This kind of bonding occurs in many materials additionally to the strong covalent and ionic bindings. Despite its relatively low binding energy, it is of vital importance for life on earth. H-bonds form the microscopic structure of e.g. water, aqueous solutions, and alcohols and cause the surprisingly complex phase diagram of water (Amann-Winkel et al., 2016). Furthermore, H-bonds stabilize the complex structure elements of macromolecules like proteins (Pauling et al., 1951; Pauling and Corey, 1951). The functionality of a protein is strongly dependent on its structure. The interaction of proteins with water molecules as a solvent is important for any living organism. MAs set up a model system that allows studying H-bonds on a medium complexity level since the molecules are relatively simple compared to macromolecules. MAs consist of a carbon chain and one hydroxyl group. The structure of all MAs can be described as R-OH in which R stands for the carbon chain and OH for the hydroxyl group. This also visualizes the structural similarity to the most common H-bonded liquid, water. Water can be seen as an MA with an additional hydroxyl group instead of a carbon chain with the consequence that water can be part of four H-bonds in contrast to MAs which can only build up two H-bonds. Therefore, water builds a complex net-like structure for which a quantum mechanical description is required (Li et al., 2011). In alcohols chain-, ring- or lasso-like structures prevail, which can be rationalized with classical physics (Brot, 1989; MacCallum and Tieleman, 2002; Sillrén et al., 2012). The more central the OH group is positioned in an MA, the better it is shielded from other hydroxyl groups by the alkyl chain. This has a major influence on the structure and dynamics in MAs. Because MAs allow investigating the interplay between these two fundamental forces, they have been studied from the early
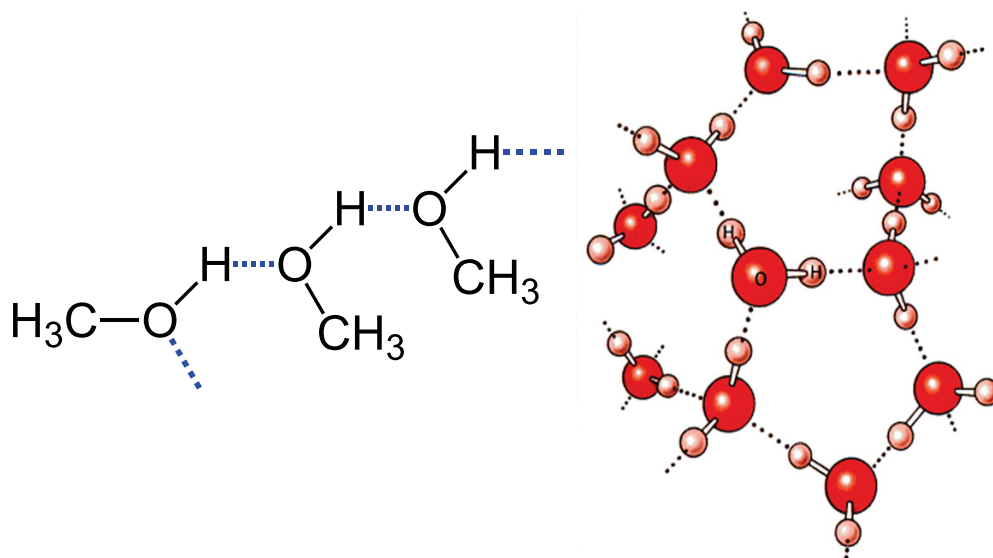
**Figure 2.1:** Comparison of hydrogen bonding in methanol (left) and water (right). Adapted from wikipedia.org (Jü, 2013; Roger Eckert, 2002).

beginnings of x-ray science (Stewart and Morrow, 1927). Supramolecular clusters are formed in long chained branched MAs with the H-bonded oxygen cores inside and alkyl chains looming outwards, which gives rise to a typical length scale causing a distinct prepeak at medium momentum transfer values in x-ray and neutron diffraction patterns (Pierce and MacMillan, 1938; Weitkamp et al., 2000; Yamaguchi et al., 2000). This prepeak can be assigned to the correlation between oxygen atoms in the liquids (Tomsic et al., 2007). This prepeak yields information about the topology of supramolecular arrangements (Franks et al., 1993). It has intensively been investigated in various alcohols building up different supramolecular structures, which will be summarized later. The approach of this thesis is to investigate hydrogen bonding of branched MAs with long alkyl chains for which significantly different supramolecular structures are suggested from e.g. dielectric spectroscopy studies. Open questions are if different supramolecular arrangements manifest in the prepeak or oxygen K-edge characteristics and how these structures depend on temperature and pressure. This is directly linked to hydrogen bonding and steric hindrance.

Moreover, there have been several studies using inelastic scattering methods to probe bulk properties of alcohols. It has been shown that the oxygen K-edge is sensitive to H-bond networks in liquid systems (Juurinen et al., 2014; Nilsson et al., 2010; Lehmkühler et al., 2016). The combined results of molecular dynamic simulations and x-ray Raman scattering has shown that hydrogen bonding produces a spectral signature that can help to understand the local arrangements in MAs (Pylkkänen et al., 2010).

## 2.2 Debye process in monohydroxy alcohols

The Debye process describes a dielectric relaxation response in liquid alcohols and water which has been investigated for over 100 years. Water and MAs do feature a so-called Debye-like absorption peak, which was introduced by Peter Debye based on the assumption of the response of ideal free dipoles to an external electric field (Debye, 1929). However, recent studies have shown that in contrast to the common knowledge the Debye-like absorption in liquid water is due to the collective dipole moment of supramolecular structures formed by H-bonds (Hansen et al., 2016), similar to MAs (Böhmer et al., 2014). Hence, it is surprising that even such a prominent process exploited by microwave ovens (Franks, 1972) is not jet understood completely on a molecular level. Additionally, to the Debye process distinguishing MAs and water from most other liquids, a so-called $\alpha$-process is located on the high-frequency flank of the Debye process. The $\alpha$-process is associated with unbounded MA molecules and is connected to their structural relaxation (Murthy and Tyagi, 2002). This process also appears in many other liquids (Nielsen et al., 2009). Figure 2.2 shows a typical dielectric absorption spectrum of three MAs and propylene carbonate (PC). The dielectric loss of the MAs shows a clear two-peak structure that is usually explained by intermolecular structuring. The hydrogen bonded oxygen atoms form the core of these intermolecular clusters, while the alkyl chains are radiating outwards. The strength of the Debye process differs about two orders of magnitude in the octanol isomers 2-ethyl-1-hexanol (2E1H) and 4-methyl-3-heptanol (4M3H), which indicates the formation of chainlike arrangements in 2E1H and ringlike clusters in 4M3H (Singh and Richert, 2012; Gainaru et al., 2011). This shows that the overall topology of these structures depends on the position of the OH-group. If the OH group is positioned in the center of the molecule, ringlike clusters are prevailed in which the resulting dipole is weak (Dannhauser, 1968a,b). If the OH-group is located in a terminal position, chainlike clusters seem to be the dominant species producing a large collective dipole moment. These assumptions are obvious but dielectric spectroscopy measures the orientation polarization. To get more reliable information about the structure, dielectric spectroscopy has been combined with results from 2E1H obtained by e.g. nuclear magnetic resonant (NMR) and near infrared measurements (NIR) to verify the microscopic model (Gainaru et al., 2011). However, the nature of these structures, their size, topology, and dynamics, especially over a wide range of pressure, temperature and in mixtures with other liquids have been a topic of recent science. A straight forward way to get deeper information at a molecular level is performing computer simulations. It has been tried to determine the number of rings and chains in monoalcohols by computer simulations, but the results are wide spreading (Gómez-Álvarez et al., 2013; Vrhovšek et al., 2011; Matisz et al., 2011; Benmore and Loh, 2000).
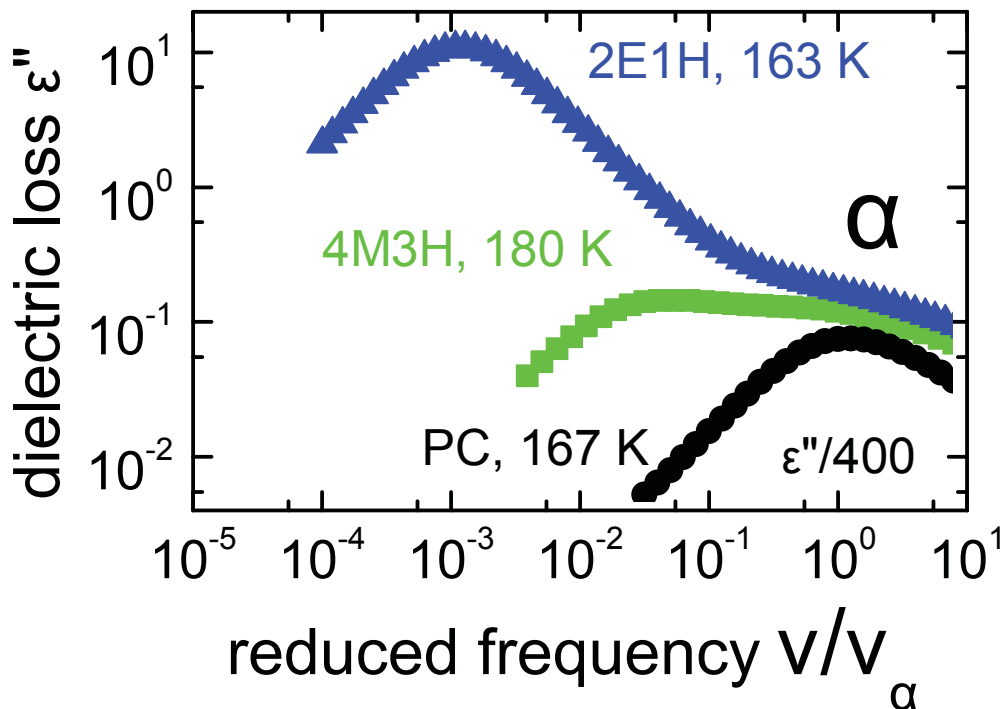
H



**Figure 2.2:** Dielectric loss spectrum of 2E1H, 4M3H and propylene carbonate (PC). Reprinted with permission from C. Gainaru, R. Figuli, T. Hecksher, B. Jakobsen, J.C. Dyre, M. Wilhelm, and R. Bohmer, Phys. Rev. Lett. 112, 098301, (2014), Copyright (2016) by the American Physical Society. Permission to edit the figure guaranteed by C. Gainaru (2016).

## 2.3 Problems to be addressed

The goal of this thesis is to find a fingerprint in the static and dynamic structure factor of supramolecular rings and chains in sample systems that are known to form predominantly one species of supramolecular structure by employing x-ray diffraction (XRD) and x-ray Raman scattering (XRS). Namely, the flowing questions are addressed in this thesis:
At First, it is convenient to observe the destruction of supramolecular arrangements by admixture of halogen alkanes, which yields unique information on how the prepeak changes if supramolecular arrangements get disturbed. In particular, there are dynamic measurements on mixtures of 2E1H with halogen alkanes leading to a nonlinear decrease of the strength of the Debye process (Preuß et al., 2012). The origin of this decrease remains uncertain since either a decrease in the overall chain length or a reducing of the overall number of clusters is possible. An aim of the XRD study presented in this work is to clarify this question.
As a next step, a transformation from ring- to chainlike arrangements due to the mixture

of ring-building MAs will be tracked by XRD to find a fingerprint of a ring to chain transition in the static structure factor (Bierwirth et al., 2014).

Moreover, an NMR study on the monoalcohol n-butanol has led to the proposal of transient self-reconstructing supramolecular chains explaining the different time scales of the two processes, referred to as the transient chain model (TCM) (Gainaru et al., 2010). This model is based on the assumption, that the Debye process is not directly a result of the forming and breaking of H-bonds. It can be understood as a changing of the overall dipole moment due to the attachment and detachment of molecules to the end of the supramolecular chains, which happens on a much faster timescale. The transient chains are supposed to be composed of $N = 5 - 10$ molecules. Similar observations have also been made for 2E1H and it has been found that this formation is strongly dependent on temperature (Gainaru et al., 2011) and pressure (Pawlus et al., 2013). Especially a change of the hydrogen bond equilibrium at a temperature of $250\,\mathrm{K}$ and an oppositional behavior due to the application of pressure in 4M3H and 2E1H have been surprising results. The TCM hypothesizes typical length scales in the liquid that can be probed via XRD. Additionally, different structures of the H-bonded network can be studied by XRS.

# Chapter 3

# Theory

## 3.1 X-ray diffraction at liquids

In the following chapter, an overview of the theoretical background of x-ray diffraction (XRD) on liquid or amorphous materials will be given which describes the elastic scattering of x-rays to obtain the pair distribution function (PDF). XRD is a powerful tool to investigate the structure of matter. X-rays were used for more than a hundred years to determine the structure of crystalline materials (Bragg and Bragg, 1913; Debye and Scherrer, 1916). Progress in science and technology allowed to determine more complex systems such as the helical structure of DNA (Watson et al., 1953) and biologically relevant substances of a macromolecular size such as viruses in solution (Kratky, 1982; Choi and Morais, 2014). However, mentioning all the progress that has been achieved by XRD applications would go too much into detail. Peculiar attention will be paid to the aspects that need to be considered in the special case of scattering of x-rays on liquid samples. XRD is a well-established method to obtain information about the structure of liquids such as bond lengths, angles and the local coordination (Benmore, 2012; Fukasawa and Sato, 2011). In particular, the intensity of elastically scattered monochromatic x-rays is proportional to the static structure factor $S(q)$, which can be transformed into the PDF. A detailed derivation based on the book „Elements of Modern x-ray Physics" (Als-Nielsen and McMorrow, 2011) is given in the following chapter. The differential cross-section of the elastic x-ray scattering process is given by

$$\frac{d\sigma}{d\Omega} = \frac{I_{\text{sc}}}{\Phi_0 \Delta\Omega}.$$  (3.1)

$\Phi_0$ is the incident flux, which means the number of photons passing through a unit area per second. $I_{\text{sc}}$ are the scattered photons measured by a detector covering the solid-angle increment $\Delta\Omega$. Thus, this cross-section defines the efficiency of the experiment. In the case of elastic x-ray scattering on one electron, the cross-section becomes

$$\frac{d\sigma}{d\Omega} = r_{\text{e}}^2 |\epsilon \cdot \epsilon'|^2$$  (3.2)

with the polarization of the incident field $\epsilon$, the polarization of the radiated field $\epsilon'$ and the free electron radius $r_{\text{e}} = \frac{e}{4\pi\epsilon_0 m_{\text{e}} c^2}$ defining a fundamental length scale in this
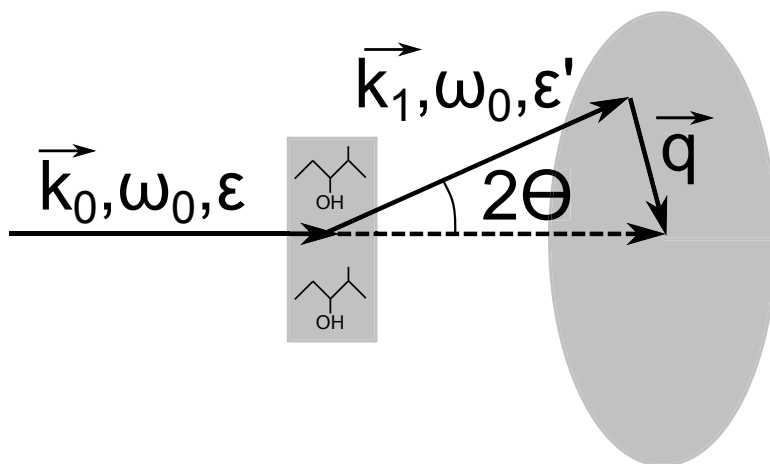
**Figure 3.1:** Scattering geometry of the elastic x-ray scattering process. A vessel with MAs and an image plate detector are sketched in gray. The wave vector transfer $\vec{q} = \vec{k}_0 - \vec{k}_1$ is the difference between the incoming and the scattered wave vector.

problem based on a non-quantum relativistic model of the electron calculated from universal constants (electric charge $e$, permittivity of free space $\epsilon_0$, mass of the electron $m_\mathrm{e}$, speed of light $c$). This is referred to as the Thomson differential scattering cross-section, which is important for the outline of scattering experiments because the x-rays produced by synchrotron light sources are linearly polarized in the horizontal plane. It follows directly that scattering experiments should be performed in vertical scattering geometry and that the polarization has to be corrected if image plate detectors are used, which will be described in the data treatment section. A sketch of a typical diffraction experiment is depicted in figure 3.1. Monochromatic x-rays with the wave vector $\vec{k}_0$ are elastically scattered without energy transfer to the system $\hbar\omega_0 = \hbar\omega_1$ and the scattered photons with wave vector $\vec{k}_1$ are detected by a detector system. The wave vector transfer $\vec{q} = \vec{k}_0 - \vec{k}_1$ is dependent on the scattering angle $2\Theta$ given by $|\vec{q}| = \frac{4\pi}{\lambda}\sin(\Theta)$. According to Als-Nielsen, the intensity scattered at an ensemble of identical atoms can be written as the interference of spherical waves emitted by all atoms $n,m$

$$I_\mathrm{coh}(\vec{q}) = f(\vec{q})^2 \sum_n \sum_m \mathrm{e}^{i\vec{q}\cdot(\vec{r}_n - \vec{r}_m)}, \tag{3.3}$$

with the atomic form factor $f(\vec{q})$ which is given as the Fourier transformation

$$f(\vec{q}) = r_\mathrm{e} \int d^3 r \rho_\mathrm{atomic}(\vec{r}) \mathrm{e}^{i\vec{q}\cdot\vec{r}}, \tag{3.4}$$

of the electron density distribution $\rho_\mathrm{atomic}(\vec{r})$ in an atom. The atomic form factors for neutral atoms with atomic number $Z = 2 - 92$ were calculated by Wang et al. (1993). As a next step, the summation with $n = m$ is separated from the rest and takes the

form:

$$I_{\mathrm{coh}}(\vec{q}) = N f(\vec{q})^2 + f(\vec{q})^2 \sum_n \sum_{m \neq n} \mathrm{e}^{i\vec{q}\cdot(\vec{r}_n - \vec{r}_m)}. \tag{3.5}$$

The total number of scattering atoms is given by $N$. The first term conforms to the scattering of a single atom and does not consist of any interference effects. As a next step the summation over $n \neq m$ is replaced by the integral over the volume element $dV_m$ and the density $\rho_n(\vec{r}_{nm})$ is introduced, which contains the number of atoms in the volume element at the position $\vec{r}_m - \vec{r}_n$. Additionally, a term proportional to the average number density $\rho_{\mathrm{at}}$ is added and subtracted

$$\begin{aligned} I_{\mathrm{coh}}(\vec{q}) = N f(\vec{q})^2 + f(\vec{q})^2 \sum_n \int_V (\rho_n(\vec{r}_{nm}) - \rho_{\mathrm{at}}) \, \mathrm{e}^{i\vec{q}\cdot(\vec{r}_n - \vec{r}_m)} dV_m \\ + f(\vec{q})^2 \rho_{\mathrm{at}} \sum_n \int_V \mathrm{e}^{i\vec{q}\cdot(\vec{r}_n - \vec{r}_m)} dV_m. \end{aligned} \tag{3.6}$$

The third term only contributes to the scattering for $|\vec{q}| \to 0$ because for finite $|\vec{q}|$ rapid oscillations of the phase factor lead to destructive interference. This estimation is not trivial at all. A detailed discussion using the example of a spherical sample can be found in the literature (Warren, 1969). This small angle regime provides valuable information on large-scale structures such as polymers and proteins and is the basis for a wide field of science (small angle x-ray scattering or SAXS) but will be neglected in the following. The average over all different choices of origin $< \rho_n(\vec{r}_{nm}) > \to \rho(\vec{r})$ leads to

$$I_{\mathrm{coh}} = N f(\vec{q})^2 + N f(\vec{q})^2 \int_V (\rho(\vec{r}) - \rho_{\mathrm{at}}) \, e^{i\vec{q}\cdot\vec{r}} dV. \tag{3.7}$$

The expectation of an isotropic sample without any preferred orientation allows the replacement $\rho(\vec{r}) \to \rho(r)$ with $r$ representing the length of the vector. The scalar product can be written as $\vec{q} \cdot \vec{r} = rq \cos(\Theta)$, which enables employing spherical polar coordinates ($\int_V dV \to \int_0^\infty dr \int_0^{2\pi} d\phi \int_0^\pi d\Theta r^2 \sin(\Theta)$) and leads to

$$I_{\mathrm{coh}} = N f(q)^2 + N f(q)^2 \int_0^\infty (\rho(r) - \rho_{\mathrm{at}}) \, 4\pi r^2 \frac{\sin(qr)}{qr} dr, \tag{3.8}$$

with the $r$-integration remaining. The structure factor of a monoatomic amorphous solid or liquid is defined as

$$S(q) = \frac{I_{\mathrm{coh}}}{N f(q)^2} = 1 + \frac{4\pi}{q} \int_0^\infty r \, (\rho(r) - \rho_{\mathrm{at}}) \sin(qr) dr, \tag{3.9}$$

which can be transformed into the radial distribution function (RDF) via a Fourier sine transformation. The RDF is defined as $g(r) = \rho(r)/\rho_{\mathrm{at}}$, and describes the probability to find an atom at a distance $r$ from a randomly chosen atom. The insertion of $g(r)$ in 3.9 and application of the Fourier sine transformation of $qS(q)$ leads to

$$g(r) = 1 + \frac{1}{2\pi^2 r \rho_{\mathrm{at}}} \int_0^\infty q \, (S(q) - 1) \sin(qr) dq. \tag{3.10}$$

Usually, the PDF which contains the same information as the RDF, is used in the literature. Both functions are connected via

$$G(r) = 4\pi r \rho_{at} \left(g(r) - 1\right).$$ (3.11)

In the following, the concept needs to be extended because up to now only monoatomic systems have been considered.
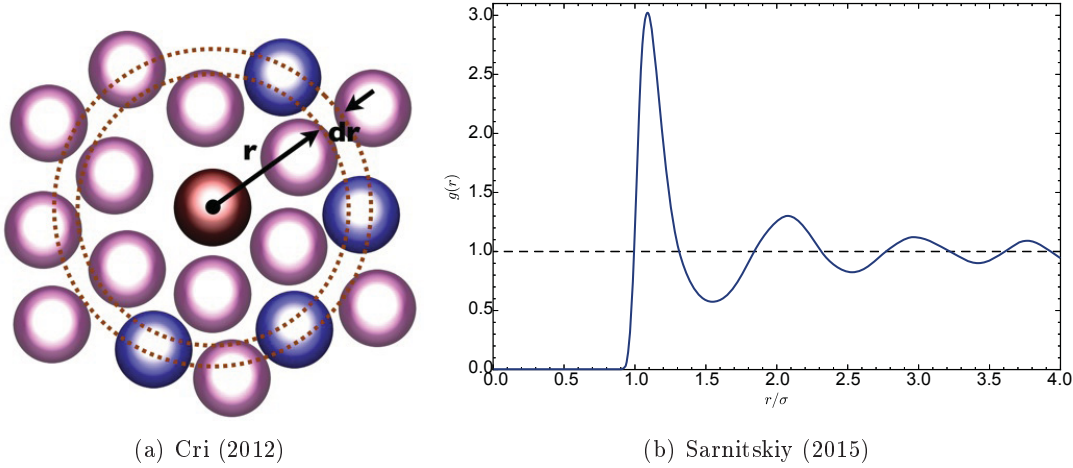


(a) Cri (2012)  (b) Sarnitskiy (2015)

**Figure 3.2:** (a) Sketch for determination of the radial distribution function, (b) radial distribution function of a Lennard-Jones fluid ($\sigma$ is the distance at which the Lennard-Jones potential has a null spot).

To obtain the partial correlation functions $g_{ij}$ between the atoms of species $i$ and $j$ the structure factor needs to be modified to

$$S(q) = \frac{\sum_i \sum_j c_i c_j f_i(q) f_j(q) S_{ij}(q)}{\left(\sum_i c_i f_i(q)\right)^2},$$ (3.12)

including the partial structure factors

$$S_{ij}(q) = 1 + \frac{4\pi}{q} \int_0^\infty r(\rho_{ij} - \rho_{j0}) \sin(qr) dr,$$ (3.13)

of the species $i,j$, which are weighted with their concentration in the liquid $c_{i,j}$. In this formula $\rho_{ij}$ represents the density of $j$-type atoms with a mean distance $r$ to an atom of species $i$ and $\rho_{0j}$ represents the average density of $j$- type atoms. The structure factor can be calculated from the measured intensity $I_{coh}(q)$ by

$$S(q) = \frac{I_{coh}(q) - \left(\sum_k c_k f_k^2(q) - \left(\sum_k c_k f_k(q)\right)^2\right)}{\left(\sum_k c_k f_k(q)\right)^2}$$ (3.14)

and then transformed into a PDF with the same Fourier transformation as a monoatomic liquid (3.10). This transformation requires the coherently scattered intensity which is

difficult to access from the measured data. Various multiplicative and additive corrections have to be applied to the data which is also strongly dependent on the experimental conditions.

## 3.2  X-ray Raman scattering

X-ray Raman scattering (XRS) is an inelastic scattering method. Such methods are very powerful for studying electronic and structural properties of matter (Schülke, 1991). In contrast to elastic scattering methods, there is an energy transfer to the system which allows to investigate absorption edges of light elements employing hard x-rays (Nagasawa et al., 1989). The incoming photon with wave vector $\vec{k}_1$ and energy $\hbar\omega_1$ is scattered into a photon with wave vector $\vec{k}_2$ and energy $\hbar\omega_2$. The wave vector transfer $\vec{q} = \vec{k}_1 - \vec{k}_2$ depends on the scattering angle $2\theta$ via $q = |\vec{q}| = \sqrt{(\omega_1^2 + \omega_2^2 - 2\omega_1\omega_2\cos(2\theta))}/c$. The energy transfer to the sample is given by $\hbar\omega = \hbar\omega_1 - \hbar\omega_2$. The interaction between the incident x-rays and the electrons of the sample can be described in lowest order perturbation theory by the Hamiltonian $H_{\text{int}}$ (Hämäläinen and Manninen, 2001)

$$H_{\text{int}} = \sum_j \frac{e^2}{2m_{\text{e}}c^2}\vec{A}_j^2 + \sum_j \frac{e}{m_{\text{e}}c}\vec{p}_j \cdot \vec{A}_j. \tag{3.15}$$

In this formula is $e$ the electron's charge, $m_{\text{e}}$ the electron mass, $\vec{A}_j$ the vector potential of the electromagnetic field of the x-rays and $\vec{p}_j$ the momentum of the $j$-th electron. The first term describes the non-resonant inelastic scattering process and in the special case of $\omega_1 = \omega_2$ x-ray diffraction. The second term is related to the absorption processes and resonant scattering. In this thesis only non resonant x-ray scattering with core electron excitation is employed. The resonant inelastic x-ray scattering cross-section can be obtained from the second term by second order perturbation theory and the Kramers-Heisenberg formula (Kramers and Heisenberg, 1925). In the special case of non-resonant scattering the differential scattering cross-section may be expressed via Fermi's golden rule as

$$\frac{\mathrm{d}\sigma}{\mathrm{d}\Omega\mathrm{d}\omega_2} = r_{\text{e}}^2|\epsilon \cdot \epsilon'|^2 \left(\frac{\omega_2}{\omega_1}\right) \sum_{i,f} P_i \left|\langle f| \sum_j e^{i\vec{q}\cdot\vec{r}_j} |i\rangle\right|^2 \delta(E_f - E_i - \hbar\omega) \tag{3.16}$$

where $r_{\text{e}}$ is the free electron radius, $P_i$ the probability to find the system in the initial state $|i\rangle$ and $|f\rangle$ the final state, $E_i$ and $E_f$ are the corresponding energies and $\vec{r}_j$ is the position of the $j$-th electron. The term containing all the accessible information about the many-body system is defined as the dynamic structure factor

$$S(\vec{q},\omega) = \sum_{i,f} P_i \left|\langle f| \sum_j e^{i\vec{q}\cdot\vec{r}_j} |i\rangle\right|^2 \delta(E_f - E_i - \hbar\omega). \tag{3.17}$$

Depending on the energy of the incident photons different excitations can be investigated such as phonons, electron-hole excitations and plasmons. Furthermore, XRS is used to
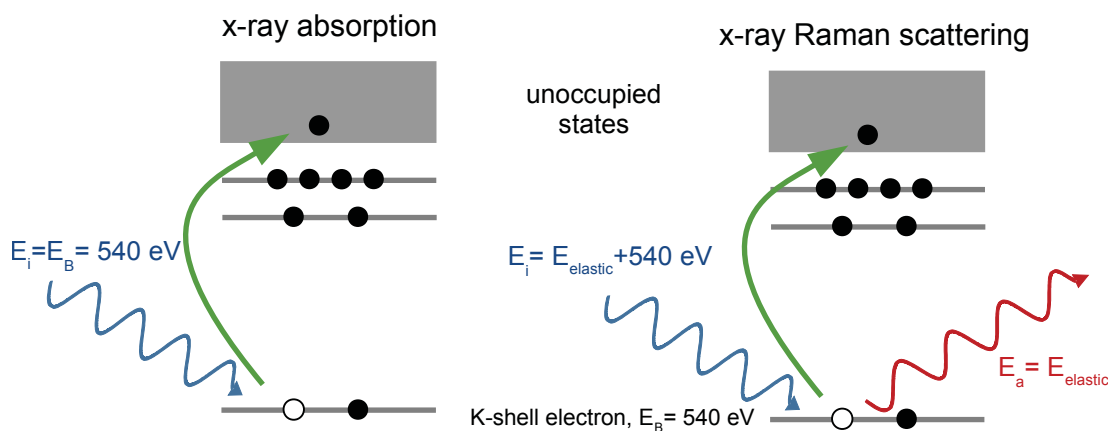
**Figure 3.3:** XAS and XRS process at the oxygen K-edge.

study inner-shell excitations. Therefore the energy transfer has to be similar to the binding energy of the probed core electron $\hbar\omega = E_B$. It can be shown that the inelastic scattering cross-section is proportional to the absorption coefficient at low-momentum-transfer excitations from inner-shell electrons ($|\vec{q} \to 0|$) (Mizuno and Ohmura, 1967). At high momentum-transfer, non-dipole transitions would contribute significantly to the spectra. The absorption edges of matter are routinely measured with x-ray absorption spectroscopy (XAS), which means that the incident photon energy is scanned over $E_B$ and the ratio of incoming and outgoing x-rays is detected. The natural limit for XAS is that soft x-rays are necessary to probe absorption edges of low Z-elements which are strongly absorbed by most materials such as surrounding air, the sample vessel or even the sample itself. The XAS and XRS processes are compared in figure 3.3. XRS can deliver similar information as XAS (Schülke et al., 1988; Manninen and Hämäläinen, 1992) but with the advantage of a free choice of the incident energy because only the energy transfer has to be in the order of the binding energy $E_B$. The incident energy $E_i = E_{elastic} + E_B$ is chosen to be the sum of the binding energy of the electron of the K-shell electrons and the energy fulfilling the Bragg-condition of the analyzer crystals which will be introduced in detail in the experimental section. This allows investigating absorption edges of low Z-elements with binding energies in the soft x-ray regime bulk sensitively using high-energy x-rays. Hence, it is possible to penetrate through complex sample environments (Sternemann and Wilke, 2016) and to investigate for example hydrogen bonded liquids like water under extreme temperatures (Cai et al., 2005), pressures (Sahle et al., 2013) and at the vicinity of alcohol molecules (Juurinen et al., 2014). In the special case of this thesis the oxygen K-edge at $540\,\text{eV}$ is measured in branched alcohols to obtain hints about the role of hydrogen bonding in these systems (Pylkkänen et al., 2010). This would also be possible with soft x-rays (Kunnus et al., 2012) but a full vacuum environment would be required due to the high absorption of soft x-rays in air, which is not feasible for among other things measurements at deep
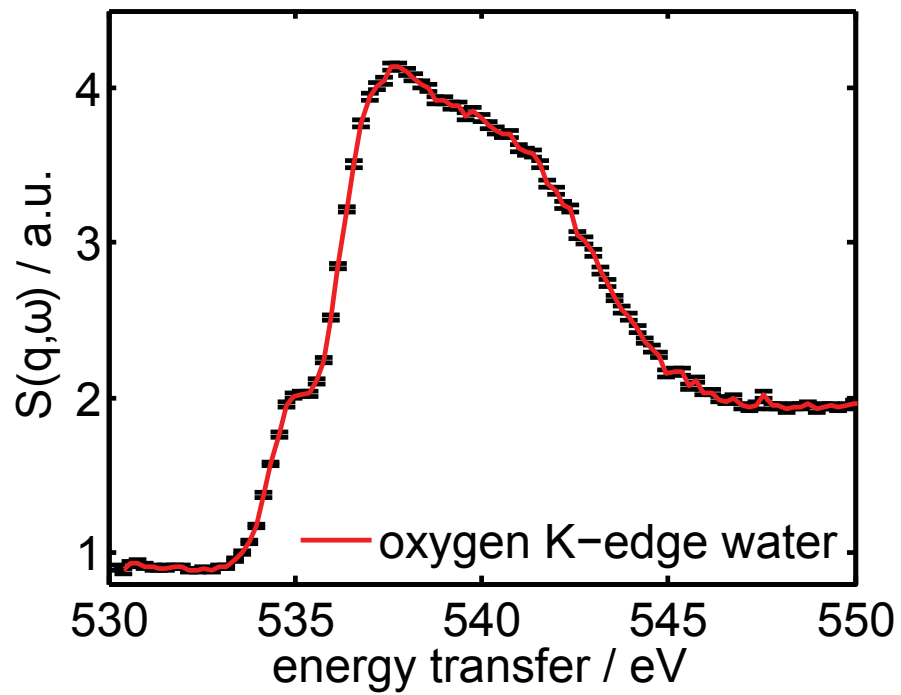
**Figure 3.4:** Oxygen K-edge of water measured at ambient conditions by XRS.

temperatures. Moreover, the penetration depth of soft x-rays does not allow to study the bulk properties of liquid alcohols. Figure 3.4 shows the oxygen K-edge of water measured at ambient conditions as an example.

# Chapter 4

# Experimental setups

All the experiments were carried out using hard x-rays with photon energies of the order of $10\,\mathrm{keV}$. These can be generated by a laboratory x-ray tube or an insertion device at a synchrotron radiation source. In contrast to x-ray tubes synchrotron radiation sources allow to tune the photon energies over a wide energy range and deliver a higher photon flux. In this thesis, both types of sources were used for elastic x-ray scattering experiments. In the following, the x-ray diffraction beamline BL9 for small and wide angle scattering of DELTA (Dortmund Electron Accelerator) in Dortmund, Germany and the high-resolution powder diffraction beamline ID22 at the ESRF (European Synchrotron Radiation Facility) in Grenoble, France are presented in detail. Furthermore, a short introduction into the *Bruker D8* laboratory diffractometer available at TU (Technische Universität) Dortmund is given. The x-ray Raman scattering (XRS) experiments could only be performed at synchrotron radiation facilities with an extremely high photon flux due to the small efficiency of the inelastic scattering process. Such facilities are for example the ESRF and PETRA III (Positron-Electron Tandem Ring Accelerator) in Hamburg. Experimental setups for inelastic x-ray scattering are available at P01 at PETRA III and at ID 20 at the ESRF. These setups are introduced in the following.

## 4.1   X-ray diffraction setup at BL9 of DELTA

Part of the x-ray diffraction measurements were performed at beamline BL9 of DELTA using the setup for wide and small angle x-ray scattering. DELTA is a synchrotron facility with an electron energy of 1.5 GeV and a typical ring current of 130 mA. The radiation is generated by a superconducting asymmetric wiggler (SAW) and monochromatized by a Si(311) monochromator. The resulting photon flux is approximately $5 \cdot 10^7 \frac{\mathrm{photons}}{\mathrm{s\,mm^2\,mA}}$ (Krywka et al., 2007). The beam is focused horizontally to a size of $1\,\mathrm{mm}$ and is vertically reduced by a slit system to a resulting beam size of $1 \times 1\,\mathrm{mm^2}$. The scattered x-rays are detected by a MAR345 image plate detector with a pixel size of $100 \times 100\,\mu\mathrm{m^2}$. Typical exposure times for a single diffraction pattern were five minutes.

### 4.1.1  Temperature dependent measurements

For temperature dependent measurements a custom sample cell was designed in collaboration with the design office and constructed by the mechanical workshop, which are both part of the TU Dortmund. Figure 4.1 shows the engineering detail drawing. The copper sample holder is contained by a cuboid shaped tank that can be evacuated to thermally decouple the sample from the environment. It has two Kapton windows for the incoming and outgoing x-rays allowing a maximum scattering angle of $\approx 33°$. The window for the incoming x-rays is significantly smaller to prevent contribution of scattered x-rays from the air in front of the sample cell to the XRD signal. This is important because of the absorption of the sample. Background scattering contributions that originate in front of the sample would be difficult to correct because different absorption coefficients have to be considered. The sample cell is equipped with three lead troughs for wiring and coolant. The sample holder can be cooled by a liquid nitrogen flow and heated by a *MINCO* heating foil. The temperature is measured by two PT100 temperature sensors and their signal is analyzed by a *Lakeshore* temperature controller which adjusts the heating power employing a closed loop proportional–integral–derivative controller (PID controller) to obtain a stable temperature. In this configuration, the sample cell provides a temperature range from $130\,\mathrm{K}$ to $350\,\mathrm{K}$ with a temperature stability of $\pm 0.5\,\mathrm{K}$. The liquid alcohols were filled into capillaries from borosilicate glass with a diameter of $2\,\mathrm{mm}$, sealed leak-tight with hot glue and set into the sample holder. It took approximately ten minutes to stabilize the temperature. When the correct temperature was reached, the sample was exposed to the synchrotron radiation for five minutes. A photon energy of $10\,\mathrm{keV}$ and a distance of $350\,\mathrm{mm}$ between sample and detector turned out to provide the best results in terms of accessible scattering angle and signal to noise ratio. The gaugeable $q$-range is limited by the beamstop and the radius of the detector i.e. a short distance provides a higher maximal $q$-value at expense of the small angle region and the other way around at large sample-detector distance. Besides, the signal to noise ratio decreases with increasing distance simply because increased amount of air-scattering producing a stronger background signal.
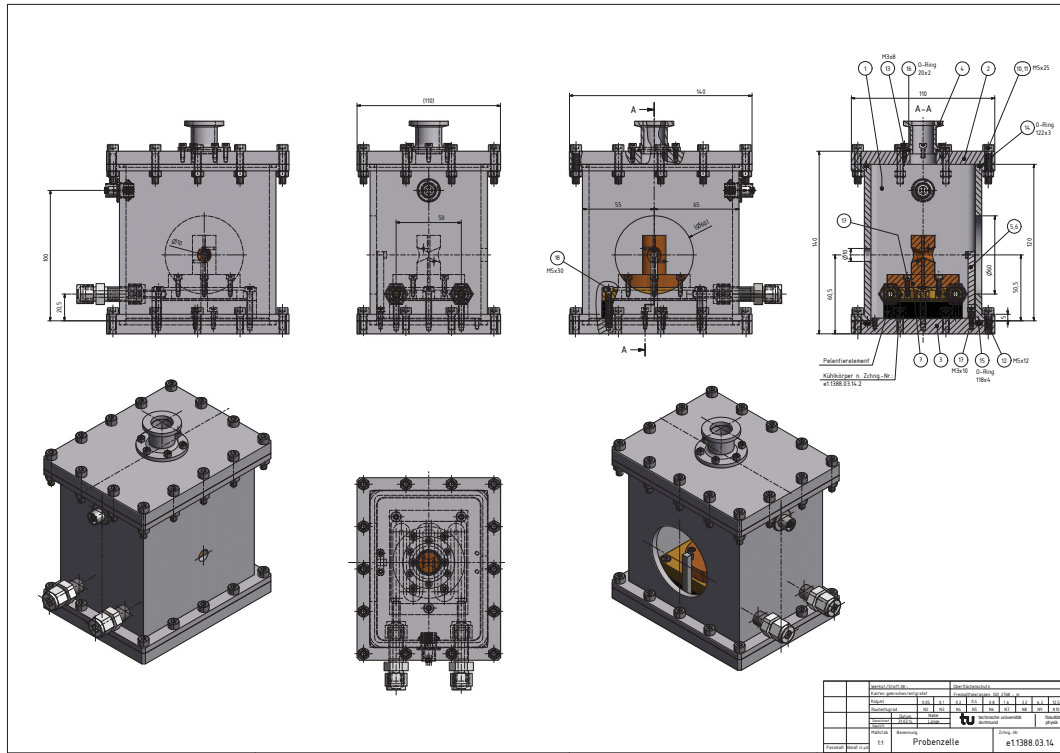
**Figure 4.1:** Engineering detail drawing of the sample cell.

### 4.1.2 Pressure dependent measurements

Generating high hydrostatic pressure within the sample volume is challenging and therefore a specially designed sample cell is necessary. Such a cell is available at BL9 and used regularly for high pressure studies (Krywka et al., 2007, 2008; Nowak et al., 2016; Berghaus et al., 2016). This cell allows experiments at pressures up to 4500 bar at temperatures between 273 K and 360 K. A picture of the setup and an engineering detail drawing are presented in figure 4.3. It is used routinely at BL9, a detailed description is given in the PhD thesis of Christina Krywka (Krywka, 2008). The pressure was increased via a high pressure connection at the top of the pressure cell employing a hand spindle pump and was measured by two pressure detectors in the cell and in the pump separately. The windows for the x-rays have to resist the high pressure and are therefore made from diamond because it is relatively transparent for high energy x-rays i.e. 83 % is transmitted through a 2 mm diamond at a photon energy of 24 keV (Henke et al., 1993). This photon energy is close to the limit of the energy range of the beamline and achieved at the cost of photon flux. This energy was the best compromise because of the rapidly decreasing transmittance with decreasing photon energy, for example only
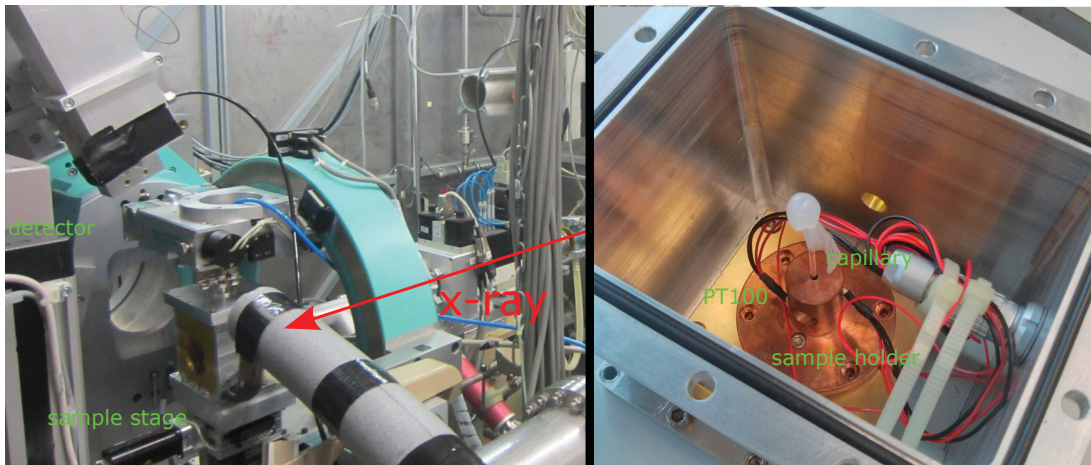
**Figure 4.2:** Picture of beamline BL9 (left) and the custom made temperature cell (right).

21 % of the beam is transmitted at 10 keV. A distance of 700 mm between sample and detector provided sufficient data quality in the medium $q$-range, allowing to compare pressure and temperature dependent measurements. This significantly reduces the signal to noise ratio due to increased background air scattering because twice the distance between sample and detector was necessary. Usually, an evacuated flight path is used to avoid air scattering in small angle x-ray scattering experiments but a flight path of the required length and diameter was not available at that time. The liquid sample was filled in a special sample holder with two Kapton windows through which the pressure is transmitted by water and separates this water from the liquid sample. These Kapton windows were substituted after each change of the sample liquid. Therefore Kapton foil was trimmed to the correct size and then glued to the sample holder by epoxy resin glue. To increase the stability of the epoxy resin, the sample holder was baked in an oven at 100°C. Then the liquid was filled into the sample holder using a syringe. Afterward, the holder was sealed with a nylon screw and placed in the corresponding orifice of the pressure cell. Then the pressure cell was closed with a screw and an O-ring to obtain high-pressure stability. When the sample was placed correctly and all the connections were closed leak-tight, the actual measurements started. During a measurement, the temperature was controlled by a chiller and additionally the temperature was measured employing a thermocouple at the outside of the sample cell. Each measurement started at ambient pressure after the adjusted temperature was reached. Then the sample was exposed to the synchrotron radiation for about five minutes followed by approximately two minutes of detector readout.
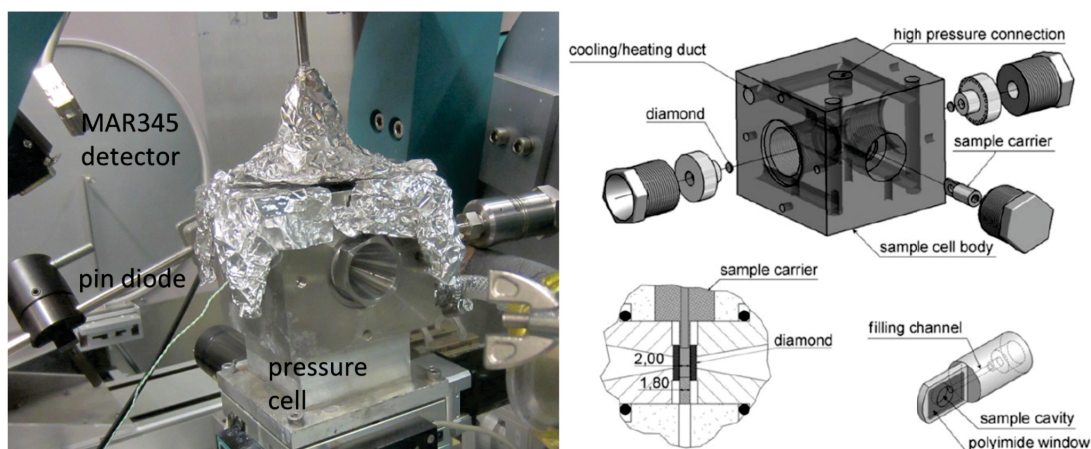
**Figure 4.3:** Picture of the pressure cell taken between two measurements (left) and an engineering detail drawing (right), reprinted with permission from C. Krywka, Ch. Sternemann, M. Paulus, M. Tolan, C. Royer, R. Winter, ChemPhysChem, 9 2809-2815 (2008), Copyright (2008) by John Wiley and Sons.

## 4.2 High energy x-ray diffraction setup at ID22 of ESRF

The highest possible energy at BL9 at DELTA is $27\,\text{keV}$. Beamline ID22 at the ESRF in Grenoble allows scattering experiments with energies up to $80\,\text{keV}$, which increases in principle the accessible maximum $q$-value. To perform a pair distribution function analysis it is necessary to integrate over the whole reciprocal space (see equation 3.10). Such an experiment is feasible at ID22 of the ESRF. A picture taken of the setup is presented in figure 4.4. Since it is not possible to display the infinite reciprocal space on a finite image plate detector, the $q_{max}$ value gives rise to a resolution limit $r_{\min} = 2\pi/q_{\max}$ in real space. The maximum $q$-value at ID22 was $180\,\text{nm}^{-1}$, which is about three times more than possible at DELTA, where an incident energy of $27\,\text{keV}$ allows to reach $60\,\text{nm}^{-1}$. The detector at ID22 has a sensitive area of $4096 \times 4096$ pixels with a pixel size of $100\,\mu\text{m}^2$ and was positioned at a distance of $590\,\text{mm}$ to the sample. The liquids were filled into borosilicate glass capillaries and were mounted in the center of the diffractometer. The mount was rotated on its horizontal axis during the measurements. This is usually done at powder diffraction experiments to average over all crystal orientations and not necessary for liquid samples but in order to spread the dose of radiation it was decided to use this option. To cool and heat the sample a cryostream system was used which covers the capillary with a stream of gaseous nitrogen that evaporates from a Dewar containing liquid nitrogen. Within the measurements the temperature range from $135\,\text{K}$ to $370\,\text{K}$ was investigated in steps of $10\,\text{K}$ with a stability of $\pm0.1\,\text{K}$. Because the maximum exposure time of the detector is five seconds 25 pictures were taken per temperature and averaged afterwards. The same was done

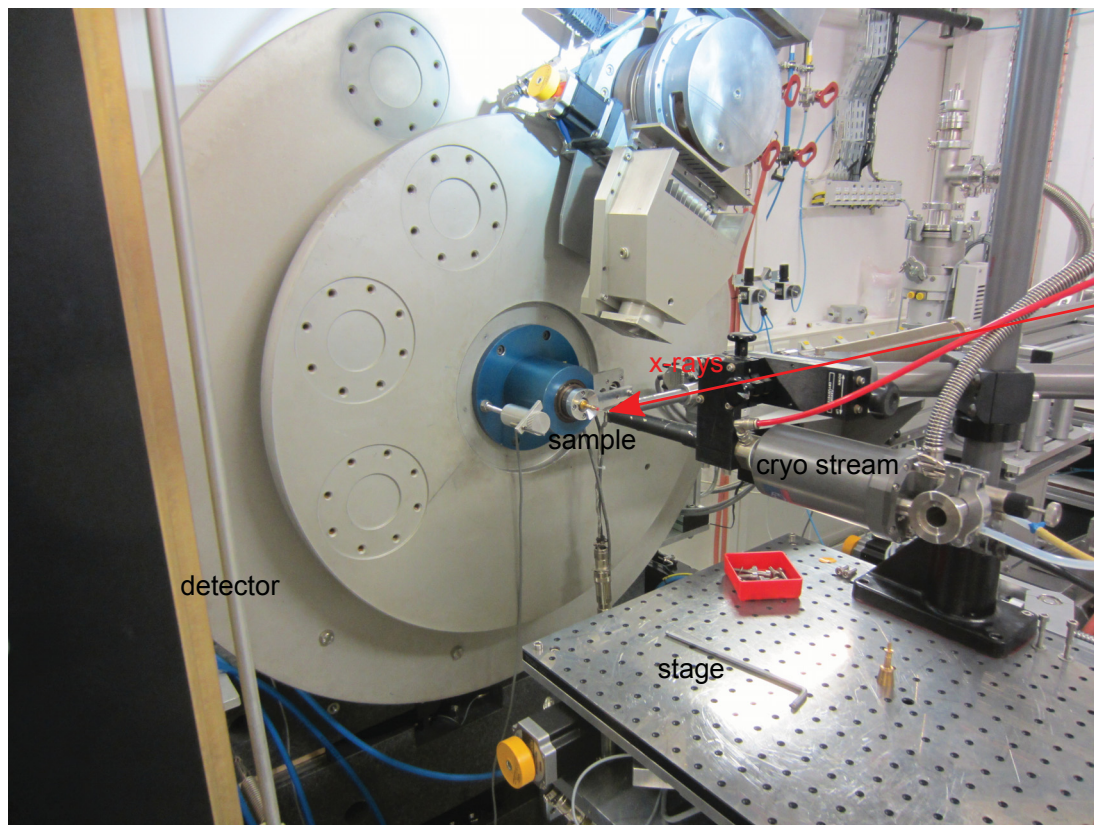with an empty capillary and without any capillary to measure the scattering of the air in the x-ray path.

**Figure 4.4:** Picture of the high resolution x-ray diffraction setup at beamline ID22 at the ESRF.

## 4.3   Laboratory diffraction setup

The *Bruker D8* laboratory diffraction setup is equipped with a copper anode that provides x-rays with an energy of 8.048 keV. These x-rays were focused by Montel optics and a Ni filter is used for $K_\beta$ suppression. The beam size was reduced by slits to $1 \times 1 \, \text{mm}^2$ mm. A picture of the *D8* is presented in figure 4.5. The scattered x-rays are detected by a *LynxEye* line detector. In contrast to the experiments done at the BL9 at DELTA, no image plate detector is used. So the *LynxEye* detector is mounted to an arm that has to be moved to scan different scattering angles. The main effect on the measurements is a significant increase of the exposure time. Moreover, the radiation of the x-ray tube is two orders of magnitude less intense than the radiation supplied by

the wiggler SAW at BL9. A typical exposure time for one diffraction pattern was two hours. For these experiments, the same sample cell as mentioned before was used.
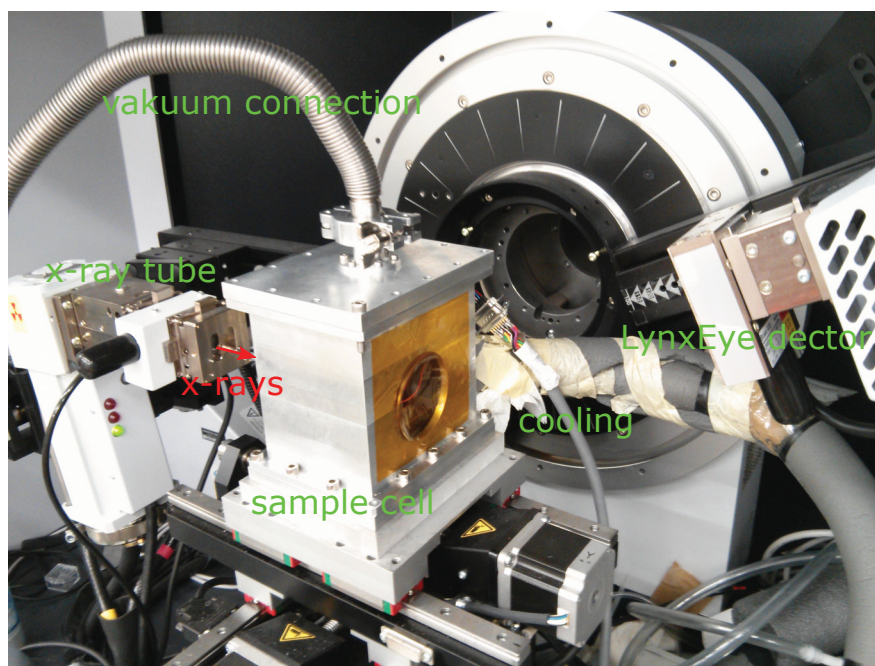


**Figure 4.5:** Picture of the sample cell mounted at the *Bruker D8* laboratory diffraction setup.

## 4.4   Density measurements

To measure the density of the liquid MAs, an *Anton Paar DSA 5000 M* was used which is available in the Chemistry department in the group of Prof. Dr. H. Rehage at TU Dortmund. A picture of the device is presented in figure 4.6. It employs the oscillating U-tube method for which a U-tube filled with alcohol is excited in resonance frequency (Anton-Paar, 2014). The resonance frequency changes in relation to the density of the liquid. A mathematical conversion is already implemented in the device and supplies the density immediately. When pouring the liquid with a syringe, air bubble formation had to be avoided. After each use, the device had to be cleaned with compressed air and acetone. The apparatus was gauged by measuring an empty U-tube and the density of water. A Peltier element that allows measuring different temperatures in the range from $273 - 300\,\mathrm{K}$ is implemented in the device.
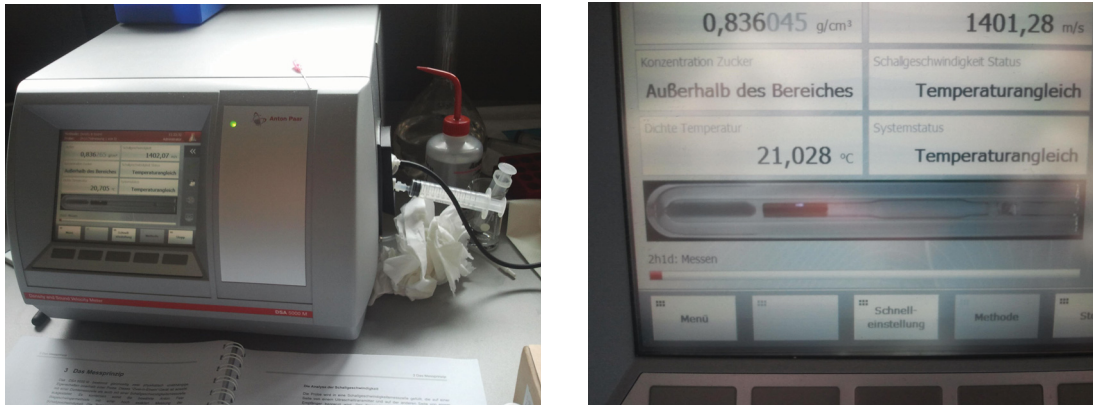
**Figure 4.6:** Picture of the Anton Paar DSA 5000 M for density measurements (left). U-tube made from borosilicate glass in which the liquid sample was filled.

## 4.5   X-ray Raman spectroscopy at ID20 at the ESRF

For XRS a synchrotron light source delivering a high photon flux is needed since the cross section is about a factor of $10^{-5}$ less than in an x-ray absorption spectroscopy experiment (Bradley et al., 2011). The ESRF in Grenoble is one of the brightest x-ray light sources in the world. The experiments were performed at beamline ID20, which is dedicated and optimized for inelastic scattering experiments. Four U26 undulators were used to generate a high photon flux. The x-rays were monochromatized by a Si(111) double crystal high-heat-load monochromator. Afterward, a Si(311) channel-cut monochromator was used to further decrease the bandwidth of the x-rays. Finally, the x-rays are focused by a mirror system. The inefficient cross section must be compensated by collecting as much of the scattered photons as possible. Because of the momentum transfer dependence of XRS spectra, averaging over a wide solid angle may lead to inaccurate results. Furthermore, a good energy resolution is required. This problem can be solved by using several spherical bend analyzer crystals positioned at a fixed scattering angles, focusing the scattered photons on a detector. Such an instrument employing six analyzer chambers equipped with 12 analyzer crystals and one detector arranged on a Rowland circle of 1 m diameter is available at ID20. The Si(660) analyzer crystals are spherical bend to focus the scattered photons on to a photon counting Maxipix 2D pixel detector (Ponchut et al., 2011). This split up of analyzing and detecting has the advantage of a good resolution of the wave vector transfer, which is given by the size of the surface of the analyzer, and energy which is dependent on the quality of the Bragg reflection. The use of an image plate detector allows applying XRS in 3D imaging over macroscopic length scales sensitively to composition and chemical environment of light elements (Huotari et al., 2011). This was convenient to check if the highly intense x-ray beam damaged the sample. Figure 4.7 shows a sketch of the

experimental setup. Sample, detector and analyzer crystals are arranged on Rowland circle to obtain the best focus on the detector.
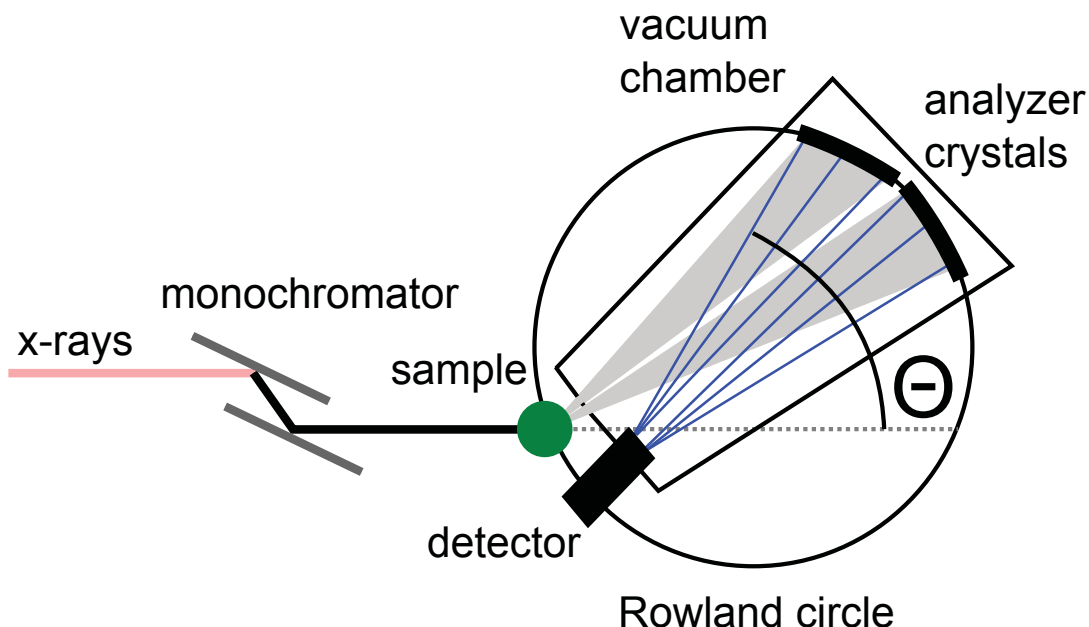


**Figure 4.7:** Schematic drawing of the scattering geometry of an XRS experiment.

The overall energy resolution of this setup depends on the quality of the analyzer crystals and the width of the incident radiation and ranges from 0.4 to 2 eV (Verbeni et al., 2009). In the special case of Si(660) the Bragg reflection occurs at $E_{\mathrm{elastic}} = 9690$ eV. The averaged energy resolution of the incident beam and all analyzer crystals is 0.7 eV. Figure 4.8 shows a picture taken of the experimental setup at ID20. The incident energy $E_{\mathrm{i}}$ has to be varied around $E_{\mathrm{elastic}} + E_{\mathrm{B}}$ to measure the energy transfer, the binding energy of K-shell electrons in oxygen is $E_{\mathrm{B}} \approx 540$ eV. To optimize the time management, the different regions of the edge were scanned with different step sizes and scanning times. The region around the edge was scanned from 520 keV to 532 keV in steps of 0.2 eV with 3 seconds per point, in the range from 532 eV to 540 eV with a step size of 0.16 eV with 8 seconds and from 540 eV to 555 eV with a step size of 0.23 eV and 6 seconds per data point. Such energy scans were repeated for about four hours until a sufficient data quality was reached. The raw spectra of each analyzer array were corrected from the underlying background which „exhibits a strong momentum-transfer dependence ranging from plasmon and particle–hole pair excitations to Compton scattering of core and valence electrons" (Sternemann et al., 2008) as described in the literature (Sahle et al., 2015b). Afterward, the data measured at the same momentum transfer were summed up to increase statistics and normalized

to a constant area. The sample cell was constructed by Yury Forov[1] and is similar to the diffraction cell described before but due to the different scattering geometry it is cylindrical and has orifices that allow to position four analyzer arrays at low scattering angle of 41° which equates to a wave vector transfer of $q = 3.6\,\text{Å}^{-1}$. It is important to shield the incident beam path between source and sample to reduce air scattering. This increases the signal to noise ratio. Furthermore, a proper beam stop built-in the sample cell in necessary for the same reason. Moreover, a good vacuum environment of the sample is useful but not necessary, if high energy photons are used. This is the major advantage of this technique.
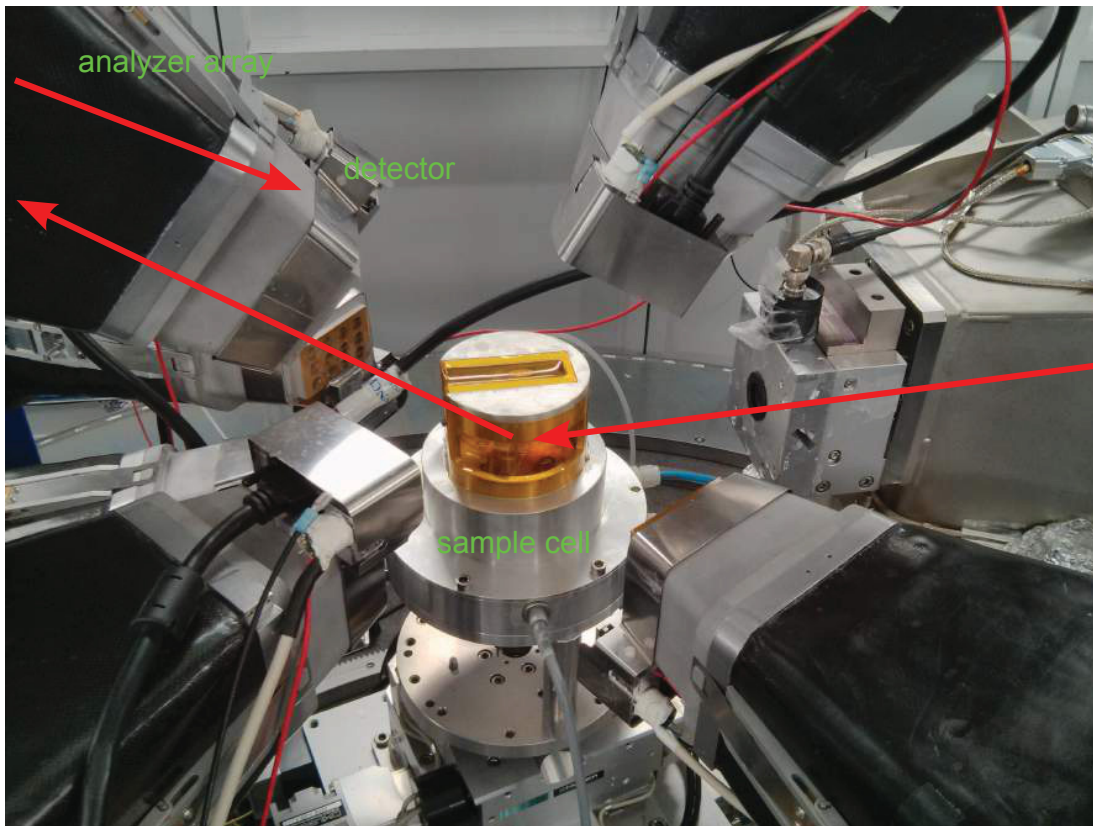


**Figure 4.8:** Picture of the experimental setup at ID20 at the ESRF, the red arrows indicate the path of the x-rays for one analyzer array.

---

[1]Master thesis of Yury Forov

# Chapter 5

# Structure formation in monohydroxy alcohols

As mentioned before, x-ray diffraction (XRD) is sensitive to the local structure in liquid alcohols via the pair distance distribution function (PDF) which requires measuring high $q$-values. This is not always achievable due to experimental restrictions limiting the maximal scattering angle. However, the static structure factor features a prepeak at $q \approx 5\,\mathrm{nm}^{-1}$ that is caused by a medium range order in e.g. glasses, liquids and especially MAs (Pierce and MacMillan, 1938; Vahvaselkä et al., 1995). This peak has been measured in various MAs (Hédoux et al., 2013; Shmyt'ko et al., 2010) and other hydrogen-bonded liquids such as m-toluidine (Morineau and Alba-Simionesco, 1998) and it is well known that it vanishes if the alcohols are diluted (MacCallum and Tieleman, 2002) or additional OH-groups are added. The typical medium-range-order distance in the liquid can be calculated from the prepeak position via $d_{\mathrm{pp}} = 2\pi/q_{\mathrm{pp}}$ and is related to a typical distance between the oxygen cores of the monohydroxy clusters separated by the carbon chains (MacCallum and Tieleman, 2002). Its width gives the coherence length in the liquid while the intensity represents the mean number of clusters or their lifetime (Morineau and Alba-Simionesco, 1998). An overview of the state of the XRD investigations on MAs is given later. To access this information the diffraction patterns will be fitted by a superposition of two Pearson VII functions and the incoherently scattered x-rays listed in the database of Wang et al. (Wang et al., 1993) will be taken. In the following, the results of an XRD study on MAs are presented. At first, an introduction into the data treatment and refinement is given. Then an experimental study on the prepeaks' behavior of long chained branched MAs due to mixing with halogen alkanes and with other MAs is presented. Afterward, the prepeak is investigated over a wide range of pressure and temperature conditions in the MAs 2-ethyl-1-hexanol (2E1H) and 4-methyl-3-heptanol (4M3H). Furthermore, a PDF analysis is done for these two alcohols at different temperatures.

## 5.1 Data treatment and refinement

In the following, the data handling will be described. The treatment of the raw data is quite similar for the different beamlines where the diffraction images were collected by image plate detectors. A diffraction picture of an alcohol taken by an image plate detector at ID22 is presented in figure 5.1. The beam was focused at a corner of the detector to get a wider scattering angle range. Dead pixels, shaded regions and the beamstop were masked to avoid artifacts, which is indicated in red. Afterward, the pictures were azimuthally integrated and corrected employing the Fit2D program (Hammersley et al., 1996). The masked areas were excluded from this process. To get the exact position of the beam and to correct the tilt of the detector, silicon or lanthanum hexaboride powder was measured as a reference. These reference samples create distinct Debye-Scherrer rings which are well known and are used to calibrate the scattering angle. The tilt is corrected via the shape of the rings of the reference samples. If the detector is tilted the diffraction rings are distorted and elliptical curves are observed. The x-rays from an insertion device at a synchrotron light source are linear polarized which has to be corrected in the resulting picture and is also implemented in Fit2D. After the correction of the pictures the scattered intensity is integrated azimuthally and the scattering angle is converted into the wave vector transfer $q$, which is independent of the wavelength of the used x-rays. This makes it easier to compare the diffraction patterns taken at different light sources with different photon energies.
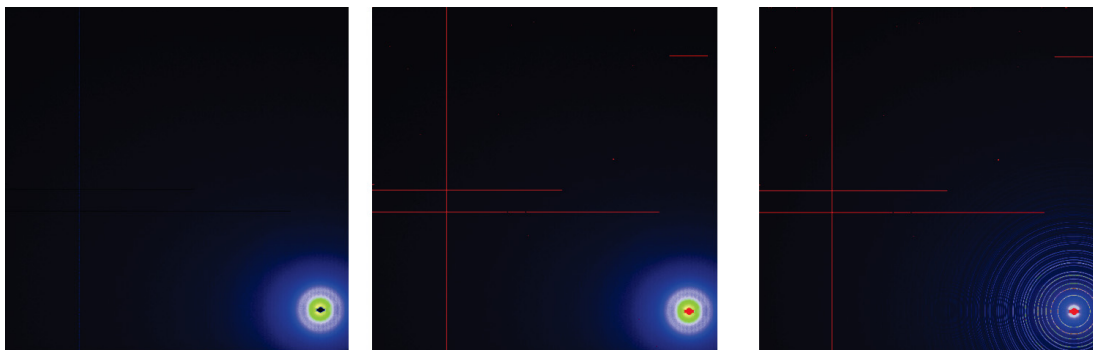


**Figure 5.1:** Image plate detector pictures that were taken of 4-methyl-3-heptanol at ambient conditions taken at ID22 (left picture unmasked, picture in the middle employs a mask for dead pixels and beamstop) and an image plate detector picture of a lanthanum hexaboride calibration sample (right).

As mentioned before, the contributions to the background signal are dependent on the sample environment but the main contribution to the scattering signal origins from scattering of air if no evacuated beampath is used. Additionally, a signal arising from the utilized sample container is measured. Therefore, it is necessary to measure an empty sample container whose signal has to be subtracted carefully. This has to be repeated

after every change of the experimental conditions, for example using capillaries with a different diameter or from a different material. If the sample cell contains a Kapton foil in the beam path, like for example the temperature and the pressure cell do, an additional peak appears in the diffraction patterns. Its angular position is dependent on the relative position of the sample. After a proper background subtraction, this peak should not be visible anymore, see the picture a) of figure 5.2. At ID22 the background scattering is only caused by air and the amorphous borosilicate capillary, as presented in figure 5.2 b) which shows a diffraction pattern of 4M3H measured at ambient conditions. However, the important question is how to scale the scattered intensity properly in any case because the background subtraction is crucial for a further analysis of the diffraction patterns. Anyway, it is important to do the background subtraction uniformly and to check the resulting diffraction patterns for consistency. Reasonable results were achieved by choosing a scaling factor in a way that the Kapton peak disappears. In the case of ID22, where no Kapton peak is observed and the main diffraction signal is caused by air, the background signal and the scattering from a capillary filled with alcohol were scaled in a way that they are equal at the lowest $q$-value where the main contribution is due to air scattering. Because of the decaying beam current at DELTA and ESRF, the x-ray intensity decreases continuously between two injections. Hence, the background corrected diffraction patterns need to be normalized to the incoming x-ray intensity $I_0$ and the transmission of the sample cell $T$. The normalized signal is

$$I_{\text{norm}}(q) = \frac{I_{\text{exp}}(q)}{I_0} \cdot \frac{1}{T} = \frac{I_{\text{exp}}}{I_0} \cdot \frac{I_0}{I_{\text{T}}} = \frac{I_{\text{exp}}}{I_{\text{T}}} \quad (5.1)$$

wherein the transmission of the sample cell is expressed as the ratio of incoming $I_0$ and transmitted intensity $I_{\text{T}}$. The consequence of this is that only the transmitted intensity is necessary for the normalization which can be approximately calculated by integrating the whole scattering signal in the analyzable $q$-range. It was convenient to normalize the diffraction patterns in the range from $4-20\,\text{nm}^{-1}$ to a constant area. After a careful subtraction of the background and normalization, the diffraction patterns were fitted in the medium $q$-range by a superposition of two Pearson VII functions

$$I_{\text{fit}} = \sum_{\text{mp,pp}} a_{\text{mp,pp}} \cdot (1 + ((q - b_{\text{mp,pp}})/c_{\text{mp,pp}})^2)^{(-d_{\text{mp,pp}})} + e \cdot C(q) + f, \quad (5.2)$$

a contribution of scaled incoherent Compton scattering

$$C(q) = \left( \frac{N_{\text{C}}}{N_{\text{mol}}} \cdot F_{\text{incoherent,C}} + \frac{N_{\text{O}}}{N_{\text{mol}}} \cdot F_{\text{incoherent,O}} \right) \quad (5.3)$$

and a constant $f$. The incoherent scattering functions $F_{\text{incoherent,C}}$ and $F_{\text{incoherent,O}}$ are taken from the literature (Wang et al., 1993) and were weighted with their portion in the molecules ($N_{\text{C}}$ and $N_{\text{O}}$ number of carbon and oxygen atoms and $N_{\text{mol}}$ sum of carbon and oxygen atoms in the molecule). For example, and mostly applied in this thesis, octanols are composed of eight carbon atoms and one oxygen atom. The contribution of hydrogen atoms was neglected because they consist of just one electron and therefore

their contribution to the scattering signal is weak. If the fit converges, it delivers the value of the peaks' positions $b = q_{mp,pp}$ and full width at half maximum (FWHM) $\sigma_{mp,pp} = 2c \cdot \sqrt{(2^{(1/d)} - 1)}$. The error bars of these values are given by the fitting routine and propagation of uncertainties. Furthermore, the total scattering intensities of both peaks are calculated by numerical integration (trapezoidal rule) of each fitted peak over the whole area. The relative error of the intensity is assumed to be $2\%$ which was estimated by different fits with varying start parameters and integration constraints. To be sure about the error bars, both peaks were also fitted by single peak-shaped functions with and without different functions fitting the background signal. The error bars were in the same order of magnitude and the results of the measurements were not affected by the employed fitting routine. Especially the comparison of the peak intensities requires the same fitting routine and normalization for every experiment. Accordingly, this model was fitted to the medium range $q$-range of each investigated sample.
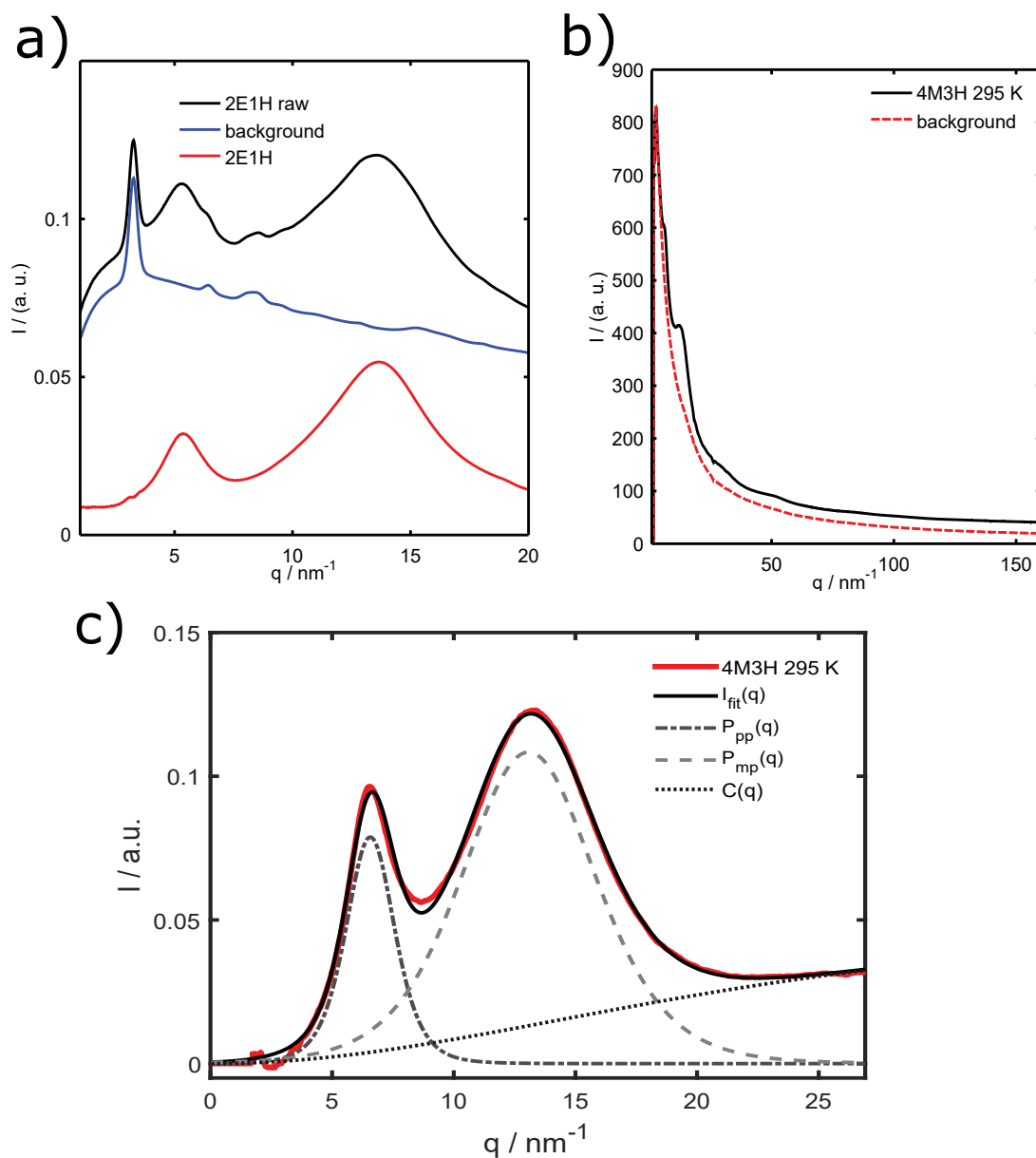
**Figure 5.2:** a) Raw data of 2-ethyl-1-hexanol measured in a temperature cell, background and the resulting diffraction pattern. The peak at $q \approx 2.5\,\text{nm}^{-1}$ is caused by scattering from Kapton foil. b) Scattered intensity of 4-methyl-3-heptanol and background measured at ID22. c) Diffraction pattern after a carefully done background subtraction and a fit of a superposition of two Pearson VII functions and scaled incoherent scattering.

## 5.2 State of the art of elastic x-ray and neutron scattering on alcohols

MAs have intensively been investigated by XRD and the observation of an inner diffraction halo has been discussed (Stewart and Morrow, 1927; Pierce and MacMillan, 1938). In contrast to the main diffraction peak which had already been connected to the distance between neighboring molecules, there has not been an explanation for the origin of the prepeak unless it has somehow been connected to the length of the alcohol molecule (Pierce and MacMillan, 1938). A newer approach is to combine XRD with molecular dynamic simulations (Akiyama et al., 2004), which enables to differentiate between intra- and intermolecular contributions to the scattering signal. This has led to the assumption that the inner diffraction peak or prepeak is mainly due to the oxygen-oxygen correlation in the liquid (Tomsic et al., 2007). Additionally, a wealth of studies employing neutron scattering has been done. This is a similar approach but due to the different scattering lengths of protons and deuteron, neutron scattering has the advantage that in principle all partial structure factors $S_{XY}$ are accessible, which has been demonstrated for various alcohols such as methanol (Weitkamp et al., 2000; Yamaguchi et al., 2000). There are obvious experimental limitations because the number of partial structure factors increases rapidly with the number of carbon atoms. There are 10 structure factors necessary for a complete description of methanol, 21 for ethanol and 36 for propanol, which explains why long-chained alcohols are mainly investigated by XRD. The prepeak is well resolved in x-ray data except for methanol and barely visible in neutron data. Because the oxygen atoms and their hydrogen bonds are responsible for the structure in the liquid, it contains the most interesting information about the structure in liquids. For example in long-chained primary alcohols, such as n-octanol, spherical clusters are formed with the oxygen atoms inside and the hydrocarbon chains radiating outwards (Franks et al., 1993). The dependence of the prepeak position on the length of the molecule is explained by fully extended alkyl chains acting as a spacer between the oxygen cores of the clusters. The main diffraction peak corresponds to the density of the liquid. It is mainly caused by the carbon correlation, and therefore it contains hints about the local structure. If long stretched molecules are aligned parallel, the density is higher than in branched alcohols, where the degree of local order between the carbon chains is smaller. This thesis deals with the structure of long chained branched MAs with different dielectric absorption strengths, which are supposed to be caused by different supramolecular structures that can be investigated via the prepeak of the liquid. The overall shape of the structure in the liquids is still unknown and XRD does not have the possibility to access the complete information about the structures in MAs. Even the combination of different computational methods has the disadvantage that different structure models can lead to similar structure factors. The question will be if the prepeak proofs pictures of structural motives that are proposed for MAs and if further information can be gained which are only accessible with XRD, such as length scales on a molecular level, and if a more general statement about the occurrence of such a remarkable feature in an important group of liquids is possible.

## 5.3 Mixtures of monohydroxy alcohols and halogen alkanes

The idea to compare an alcohol with its corresponding halogen alkane has been used to get insights into the structure of 2-iso-propanol (Zetterström et al., 1994a) and 2-chloro-and bromopropane (Zetterström et al., 1994b) employing neutron diffraction. In the following study, mixtures of monohydroxy alcohols with halogen alkanes were investigated to explore the effect on the prepeak if the number of hydroxyl groups is reduced systematically. Therefore, the alcohol is diluted with the corresponding halogen alkane in which the hydroxyl group is replaced by a halogen atom like bromine or chlorine. Such a dilution leads to a reduction of the Debye process in the mixtures, interpreted as a reduction of the supramolecular chain length or a decrease in the overall number of supramolecular chains (Preuß et al., 2012; Lueg, 2014). To get further insights into this rearrangement on a molecular level and to obtain information about the typical length scales, XRD was applied. Figure 5.3 shows the diffraction patterns of 2-ethyl-1-hexanol (2E1H) and 2-ethyl-1-hexyl chloride (2E1Cl) and mixtures at various concentrations.
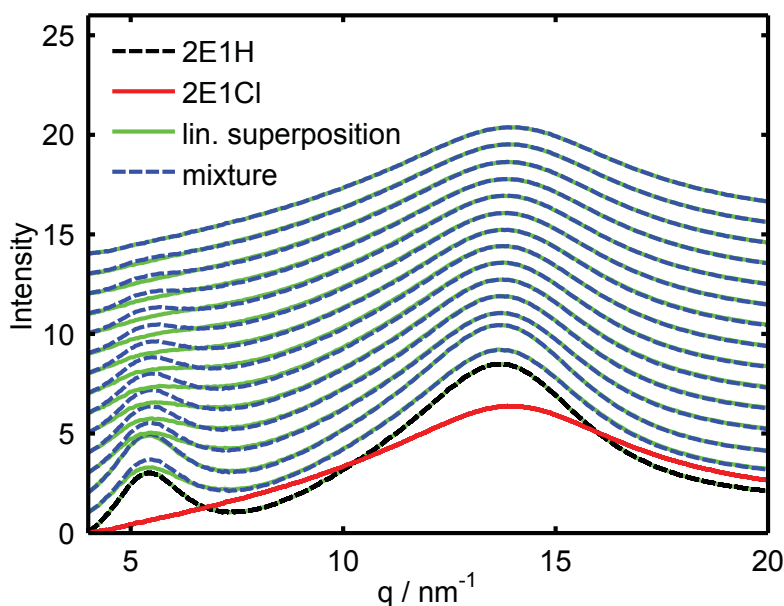


**Figure 5.3:** XRD patterns of 2E1H, 2E1Cl and mixtures, the green curves display a fitted linear superposition of the XRD patterns of the neat liquids.

The diffraction patterns cannot be displayed as a linear superposition of the neat liquids over the whole $q$-range. The most significant deviation can be observed at $q < 7\,\mathrm{nm}^{-1}$ where the diffraction patterns are dominated by the prepeak. This also applies for the mixture with 2-ethyl-1-hexyl bromide (2E1Br) but is not shown. The prepeak's intensity decreases with decreasing alcohol concentration and its position

varies. In contrast to that, the main diffraction peak can be modeled by a superposition of the neat liquids. It can be inferred that any changes of the supramolecular structure do not reflect in the main diffraction peak and the visible change of intensity and position of the main peak is caused by changes in the mixtures densities. The halogen alkanes have a higher density than 2E1H because the atomic weight of the bromine and the chlorine atom is higher than that of the hydroxyl group. The densities of the liquids are $\rho_{2E1Br} = 1.086\,\text{g/cm}^3$, $\rho_{2E1Cl} = 0.862\,\text{g/cm}^3$ and $\rho_{2E1H} = 0.833\,\text{g/cm}^3$. The diffraction
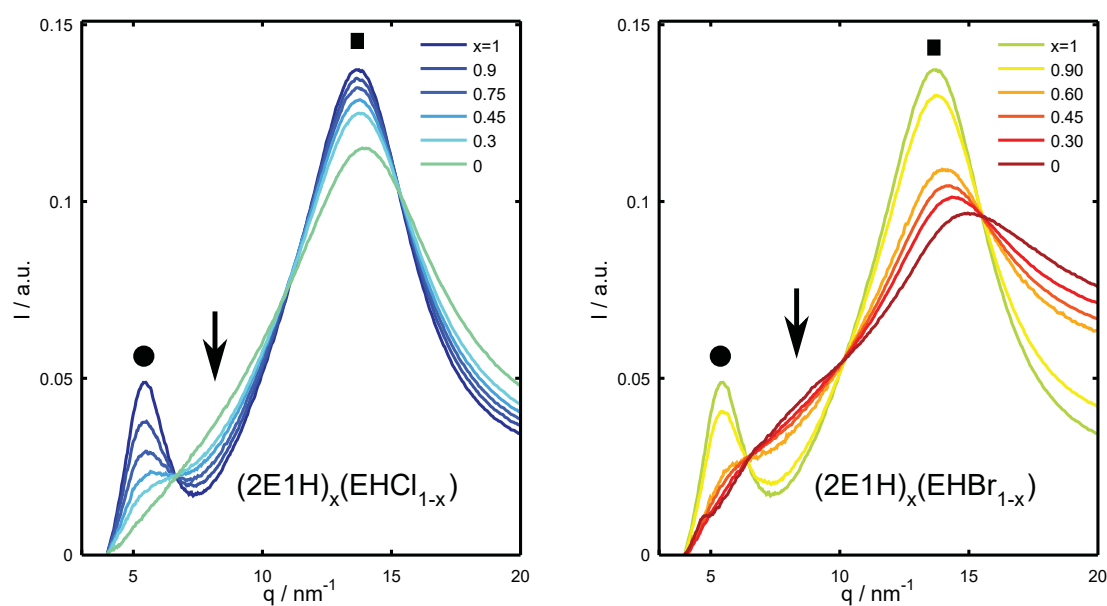


**Figure 5.4:** XRD patterns of 2E1H, 2E1Cl, 2E1Br and mixtures at selected concentrations. The discussed features are marked individually, the alcohol prepeak with a dot, the halogen alkane prepeak with an arrow and the main diffraction peak with a square.

patterns of mixtures of 2E1H with 2E1Cl and 2E1Br are both presented in figure 5.4. 2E1Br is by far the densest liquid, which is also reflected in the diffraction patterns in terms of the largest difference in the main peak region due to the strong contribution of the bromine partial structure factor at higher $q$. All the diffraction patterns were fitted over the whole $q$-range using two Pearson VII functions and the scaled incoherently scattered background. It is remarkable that even for the pure halogen alkanes two peaks were necessary to fit the diffraction patterns properly. All the parameters defining the prepeak $I_{pp}$, $d_{pp}$ and $\sigma_{pp}$ are presented in figure 5.5.
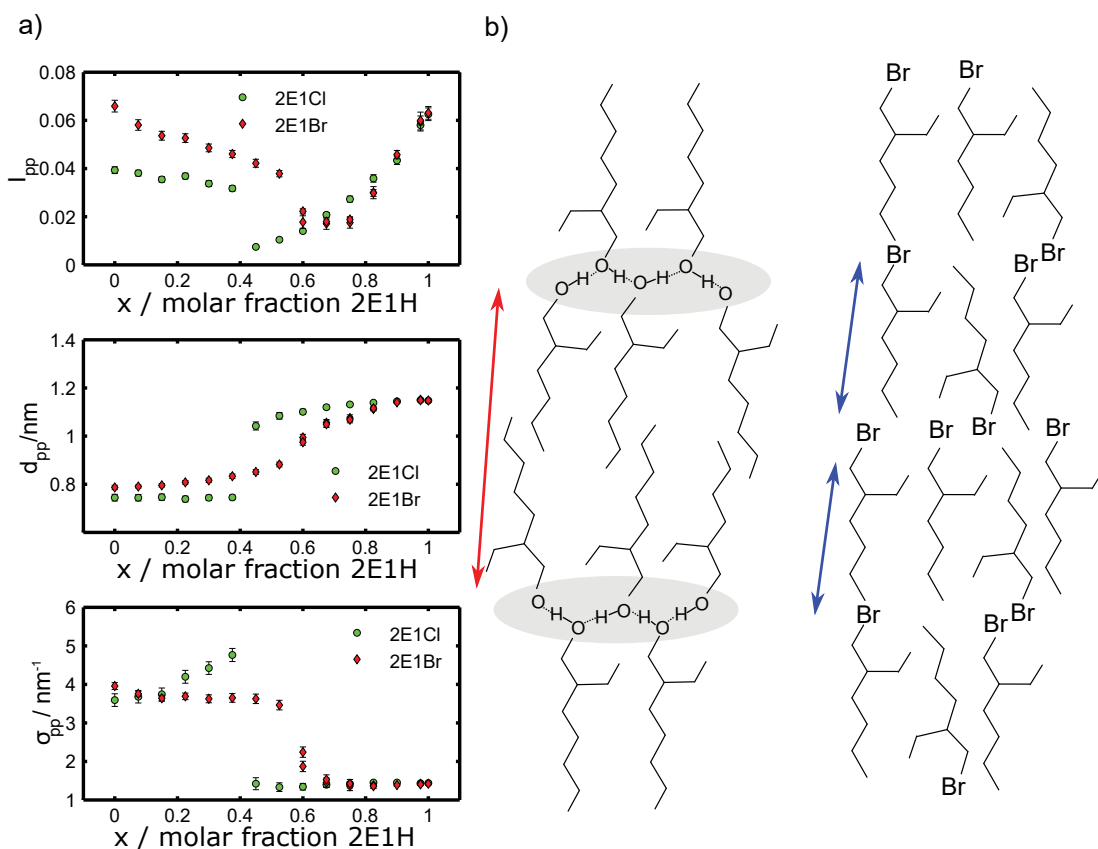
**Figure 5.5:** a) Integrated intensity $I_{pp}$, correlation length $d_{pp}$ and FWHM $\sigma_{pp}$ of the prepeak over the whole concentration range at which $x = 1$ is neat 2E1H and $x = 0$ is the neat halogen alkane. b) Sketch of structure arrangements in 2E1H and 2E1Br, the typical distances causing the prepeak are indicated by arrows.

The integrated intensity of the prepeak $I_{pp}$ correlates with the number of supramolecular structures (Hédoux et al., 2013). In pure 2E1H it is clearly resolved, while the prepeak is just a broad shoulder in the halogen alkanes but the intensity is similar (see figure 5.5). Furthermore, the peak arises at different positions in 2E1H than in the halogen alkanes. This can be explained because the prepeak's position represents a typical distance in the liquid. In pure 2E1Cl a distance of $d_{pp,\,2E1Cl} = 0.75\,\mathrm{nm}$ was measured and in pure 2E1Br $d_{pp,\,2E1Br} = 0.78\,\mathrm{nm}$. The distance between two carbon atoms in such a chain is $0.125\,\mathrm{nm}$. So the length of the molecules is $\approx 0.75\,\mathrm{nm}$ (Pierce and MacMillan, 1938), which is in the order of the distance calculated from the prepeak position of the halogen alkanes. The fact that the distance is larger in 2E1Br than in 2E1Cl can be explained by the larger bromine atom. If the molecules are bounded via H-bonds, the typical distance related to the prepeak is approximate twice the length of

35

the carbon chain. The measured value for $d_{pp}$ in 2E1H is $1.48\,\text{nm}$, which is shorter than the double length of the alkane chain and can be explained by interlocking alkyl chains. A sketch of such a structuring is presented in figure 5.5. This picture is also supported by the fact that the FWHM $\sigma_{pp}$ is much bigger in the halogen alkanes than in 2E1H because the structuring is not caused by intermolecular bonding. The structuring in halogen alkanes is caused by packing of the elongated molecules. Because there are two different structures present in the pure liquids, it is interesting to investigate the behavior in the mixture. As presented in figure 5.5 a) the transition in the mixture happens at a concentration of about $x_{2\text{E1H}} \approx 0.4$ in mixtures with 2E1Cl and at a concentration of $x_{2\text{E1H}} \approx 0.6$ in mixtures with 2E1Br. The developing of the prepeak is discontinuous in the mixture.

This leads to the idea of fitting both prepeaks in the mixtures at the same time to verify the critical concentrations more precisely. Because the prepeak position in the halogen alkanes is given by the length of the molecules, these values can be fixed to the measured ones in the neat alcohol. Some selected fits obtained with this procedure are presented in figure 5.6. This allows to obtain the portion of both structures in the mixture at the same time via the intensities of the prepeaks. These prepeaks are presented in 5.7. It is obvious that the contribution of the halogen alkanes vanishes linearly, while the intensity of the alcohol prepeak shows a discontinuity at $x_{2\text{E1H}} \approx 0.6 - 0.8$ in both cases. It decreases rapidly with decreasing alcohol concentration and decreases only slowly beyond this critical concentration. The decrease of the alcohol prepeak due to dilution of the alcohol with halogen alkane molecules even at high alcohol concentration is an indication for a reduction of the mean number of clusters or their lifetime (Hédoux et al., 2013). Therefore, these measurements indicate that a reduction of the number of chains is responsible for the decreasing Debye process. This is also supported by the fact that the FWHM changes abruptly at the critical concentration. The FWHM defines the degree of local order of the structure that causes the prepeak in the alcohol mixture (Shmyt'ko et al., 2010).

The simultaneous increase of the halogen alkane prepeak is simply caused by the increase of the number of molecules. It seems that the effect due to dilution with 2E1Br is slightly stronger than with 2E1Cl, which might be explained by a larger molecule size. It can be concluded that the reduction of the Debye process due to the dilution of 2E1H with 2E1Br or 2E1Cl is indeed a phenomenon of structural rearrangement. This disintegration of supramolecular structures takes place on a medium range order in the liquid. Even small concentrations of the halogen alkanes have a major impact on the structure formation. At alcohol concentrations beyond a critical concentration, the structuring via H-bonds is suppressed efficiently.
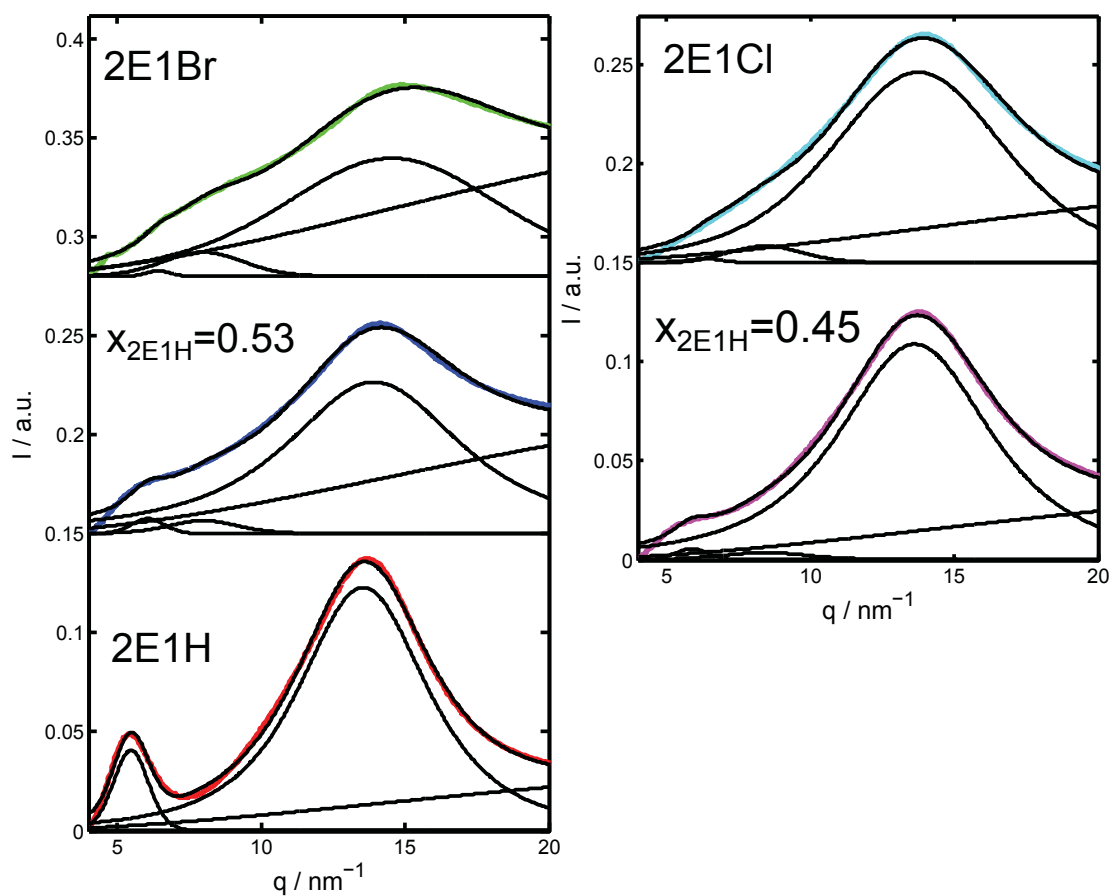
**Figure 5.6:** XRD patterns of 2E1H, 2E1Br, 2E1Cl, a mixture of 2E1H and 2E1Br at a concentration of $x_{2E1H} = 0.53$ and a mixture of 2E1H and 2E1Cl at a concentration of $x_{2E1H} = 0.45$. The measured data are displayed in colors and the fit and the different contributions to the fit are pictured in black.
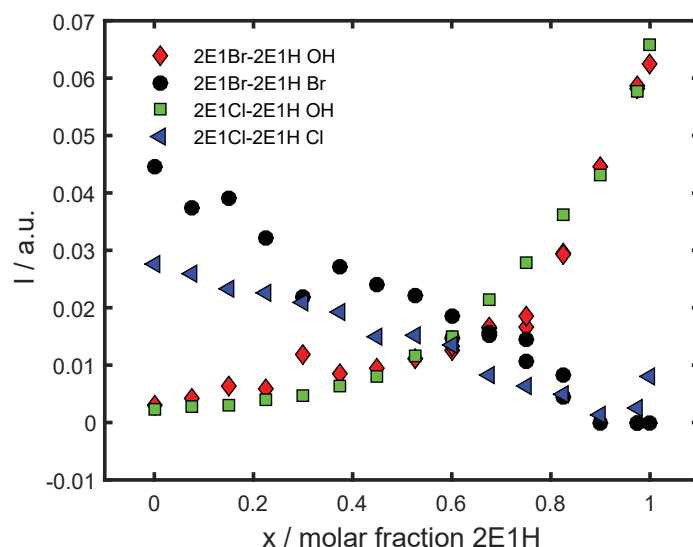
**Figure 5.7:** Prepeak intensities in mixtures of 2E1H with 2E1Br and 2E1Cl. OH describes the the prepeak measured in neat 2E1H. Br/Cl characterizes the prepeak related to intermolecular Br and Cl distances in the neat haologen alkanes 2E1Br and 2E1Cl.

## 5.4 Mixtures of ring building monohydroxy alcohols

Mixing of two ring building MAs can lead to an up to tenfold enhancement of the Debye process. This effect was discovered by Bierwirth et al. (2014) and is remarkable because most of the studies manipulating the hydrogen bond network have led to a decrease of the Debye process. Examples for this are the dilution with halogen alkanes as investigated in the previous section, the admixture of ions (Wang et al., 2005), hydration (Franks et al., 1993) or confinement (Abdel Hamid et al., 2016). Only a few studies are dealing with the amplification of the Debye process. An enhancement of 4.5% could be achieved by inducing a ring-to-chain transition by applying an electric field (Singh and Richert, 2012). An intensification of 50% has been observed in mixtures of 2-ethyl-1-butanol (2E1B) and 4-methyl-2-pentanol (4M2P), but results of calorimetric measurements have not shown striking proof for new H-bonded structures of unlike molecules (Gong et al., 2012). For mixtures of ring building MAs, an increase in strength of the Debye process of about one order of magnitude has been observed recently, which is supposed to be caused by a transition from ring- to chainlike supramolecular structures. Such a dramatic restructuring asks for an explanation on molecular level. XRD has been used to analyze the medium range structure with the goal to find a fingerprint of chain- and ringlike supramolecular structures in MAs and to complement the results from dielectric spectroscopy. The combined findings support a ring to chain transition due to mixing and were published in Bierwirth et al. (2014), which is the basis for this section. Mixtures of the MAs 4-methyl-3-heptanol (4M3H) with 2-hexyl-1-decanol (2H1D) and

2-butyl-1-octanol (2B1O) were investigated at ambient conditions. The mixtures of 2B1O and 4M3H were measured at beamline BL9 at DELTA[1], the mixtures of 2H1D and 4M3H were investigated at the laboratory diffraction setup and 2E1H was measured as a reference for a chain building MA at both sources. However, only the data obtained at DELTA are presented in this chapter because of the higher data quality that can be achieved at a synchrotron compared to the laboratory setup. All the samples were purchased from Sigma-Aldrich and used without any further treatment. 2H1D, 2B1O and 2E1H are of the same homologous series of branched alcohols. The structures of these alcohols are presented in figure 5.8. The number of carbon atoms increases from eight in 2E1H to twelve in 2B1O and sixteen in 2H1D but the degree of branching does not change. The structure consists of the main carbon chain and a shorter side chain which is joined to the second carbon atom of the main chain. This leads to a decreasing density of hydroxyl groups and therefore to fewer hydrogen bonds. 4M3H is an octanol isomer which is not part of this homologous series, its structure is also presented in figure 5.8. 2E1H is known to exhibit chainlike supramolecular structures.
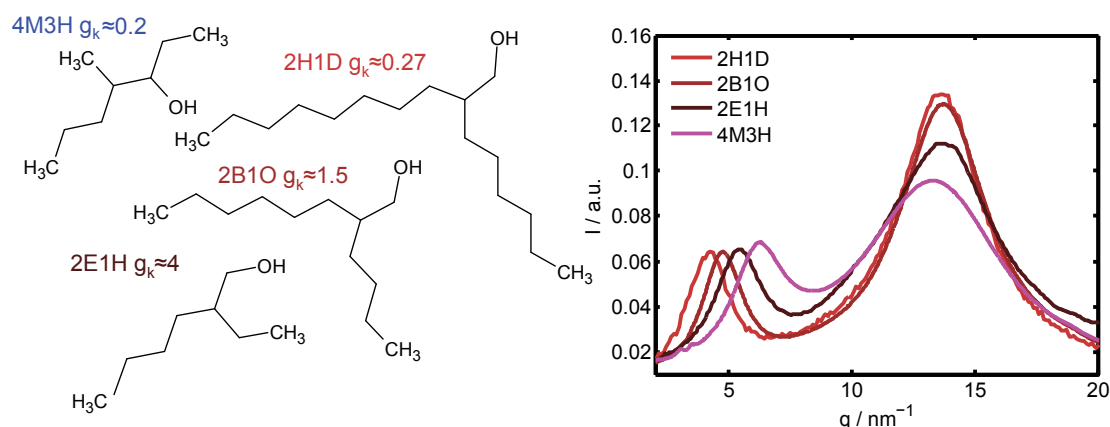


**Figure 5.8:** Sketch and diffraction patterns of the MAs 4M3H, 2H1D, 2B1O and 2E1H.

The resulting dipole moment of such supramolecular arrangements can be characterized by the so-called Kirkwood-factor $g_K$. It describes the orientational correlation of dipole moments of single molecules building up a supramolecular structure. Chain building alcohols like 2E1H exhibit a parallel alignment of adjacent dipole moments resulting in $g_K > 1$. If the number of hydroxyl groups decreases, $g_K$ decreases as well because the formation of supramolecular chains is hindered. In 2B1O a Kirkwood-factor of $g_K \approx 1.5$ is observed which is slightly bigger than the value expected for non-associating liquids $g_K = 1$. For ring building alcohols and perfect rings Kirkwood-factors of $g_K < 1$ and $g_K = 0$ respectively, are expected. The largest molecules of the homologous series, 2H1D ($g_K \approx 0.27$) and 4M3H ($g_K \approx 0.2$), fall into this category. The diffraction patterns of these alcohols are shown in figure 5.8. At first glance, it is obvious that 4M3H is not

---

[1]Bachelor thesis of Jennifer Bolle

part of the series. The diffraction patterns were fitted by two peak shaped Pearson VII functions as described in the data treatment section and the results of this analysis are presented in figure 5.9. The values obtained for 2E1H are averaged results from measurements at DELTA and the ESRF. The prepeak position $q_{pp}$ was transformed into the correlation length via $d_{pp} = 2\pi/q_{pp}$ and the main peak into the correlation volume $V_{mp} = d_{mp}^3$. It is expected that the correlation length of the prepeak depends linearly on the effective length $l_{eff}$ of the molecules' carbon chains because they act as a spacer between the hydrogen bonded oxygen cores of the clusters. The effective carbon chain length of each molecule can be calculated assuming the distance between two carbon atoms to be 0.125 nm. To consider the branching, the main- and side-chain lengths have to be averaged. Figure 5.9 shows that $d_{pp}$ and $V_{mp}$ vary linearly with the effective chain length $l_{eff}$ and the densities $\rho$ of the liquids, respectively. The prepeak's FWHMs
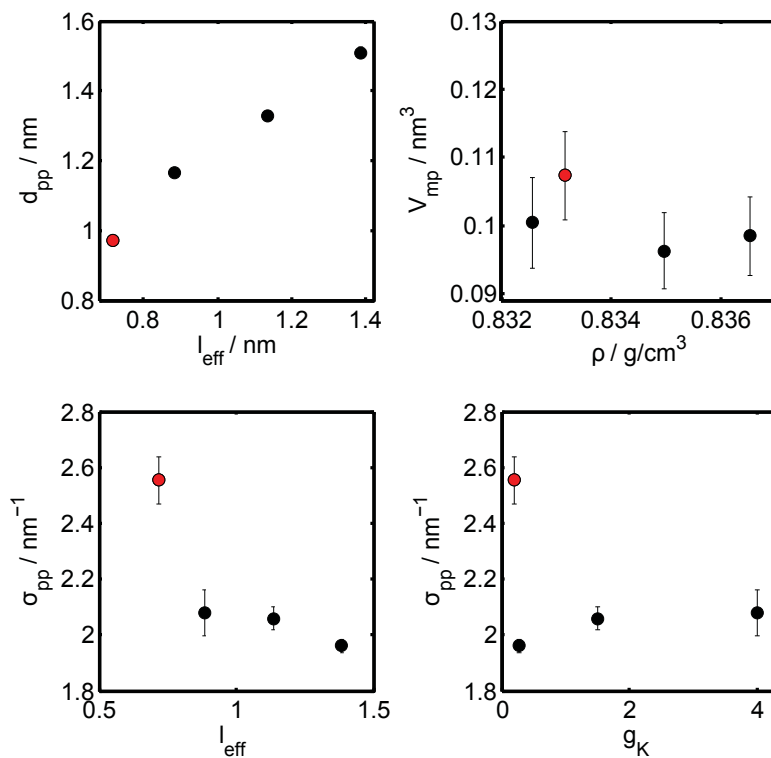


**Figure 5.9:** Fitting results of the MAs 4M3H, 2H1D, 2B1O and 2E1H. The peak positions are transformed into $d_{pp}$ and $V_{mp}$ and are plotted against the effective chain length $l_{eff}$ and the density $\rho$ measured at $T = 293$ K. The intensities $I$ and FWHMs $\sigma$ are plotted against $g_K$. The members of the homologous series are displayed in black and 4M3H is presented in red.

$\sigma_{pp}$ are plotted against $l_{eff}$ and $g_K$. There is a weak dependence between the effective chain length $l_{eff}$ and $\sigma_{pp}$. The prepeak becomes narrower with increasing $l_{eff}$, indicating a sharper structuring. This might be explained by smaller structures due to the better screened hydroxyl groups by the longer carbon chains. This is also reflected by an in-

creasing $\sigma_{pp}$ at increasing $g_K$ in the homologous series. A larger $g_K$ might be connected with an increasing $\sigma_{pp}$ because of longer, less defined structures but such a conclusion is not possible if different liquids are compared because the width is also dependent on $l_{eff}$. Moreover, it is difficult to compare the width of peaks that were measured in different experimental setups since the width depends on the bandwidth of the incident photons. In a nutshell, the increase of carbon atoms in the molecules by not changing the general molecule structure leads to a decrease of $g_K$, indicating a transition to ringlike structures which is guided by an increase of $\sigma_{pp}$. However, an interpretation beyond the homologous series is not possible because of the values measured for 4M3H. Table 5.1 contains the correlation lengths of both peaks of the neat alcohols, extracted from figure 5.10, as well as the densities. The next step is to measure mixtures of these MAs, for

| Alcohol | $d_{pp}$ /nm | $d_{mp}$ /nm | $\rho/$ g/cm$^3$ | $l_{leff}$/nm |
|---------|--------------|--------------|------------------|---------------|
| 4M3H | 0.977 | 0.484 | $0.8332 \pm 0.0001$ | 7.18 |
| 2E1H | 1.167 | 0.465 | $0.8326 \pm 0.0001$ | 8.85 |
| 2B1O | 1.320 | 0.457 | $0.8350 \pm 0.0001$ | 11.35 |
| 2H1D | 1.503 | 0.461 | $0.8369 \pm 0.0001$ | 13.85 |

**Table 5.1:** Tabular containing the measured values of $d_{pp}$ /nm, $d_{mp}$ /nm at $T = 298$ K. And the densities $\rho$ at $T = 293$ K of the neat alcohols.

example, 2H1D and 4M3H which express similar $g_K$. In the mixtures, ringlike clusters are supposed to be disfavored. This leads to a transition into more chainlike clusters with a higher dipole moment causing a significantly enhanced Debye process (Bierwirth et al., 2014). Hence, it is possible to observe the effect of an increasing Debye process on the XRD patterns and to distinguish between the effect of an increasing $l_{eff}$. To track changes in the supramolecular configurations on a molecular level and to access typical length scales, mixtures of 2B1O and 2H1D with 4M3H were measured at eleven different concentrations. The XRD measurements of the mixture with 2H1D and 2B1O were measured at $T = 295$ K. The concentrations $x$ are given in the molar fraction of one of the alcohols, so the concentrations $x = 0$ and $x = 1$ are representing the neat alcohols. Figure 5.10 shows the measured diffraction patterns normalized to a constant area as described in the data treatment section. The mixtures are not a linear superposition of the neat alcohols, especially the prepeak region differs significantly. The prepeak of the mixture broadens and its height decreases in the mixture, while the main peak varies smoothly. To verify these impressions it was necessary to fit the whole diffraction pattern and to compare the resulting parameters with each other. In the following, the deviation of the correlation lengths $d$ of the different mixtures from a linear mixing behavior $\Delta d = d - d_{lin}$ is discussed. For this purpose, the correlation lengths of both peaks $d_{mp}$ and $d_{pp}$ of the neat MAs were extracted and the corresponding correlation lengths of the mixtures were calculated assuming a linear mixing behavior. This could be achieved by calculating the linear function that connects the $d$ values of the neat alcohols. These values were subtracted from all the measured values and the resulting values $\Delta d$ are presented in figure 5.11. This has the advantage of pronouncing small deviations and a better comparability between the two different mixtures. To check
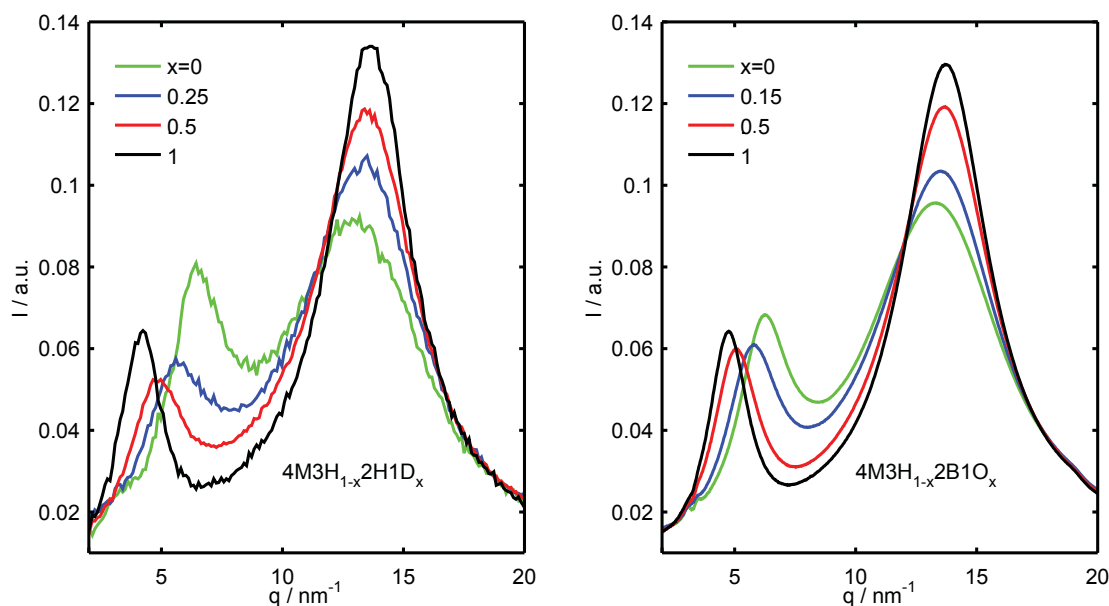
**Figure 5.10:** XRD patterns of selected mixtures of 4M3H with 2H1D (laboratory diffraction setup) and 2B1O (DELTA beamline Bl9) as well as of the neat alcohols. The diffraction patterns were taken at ambient conditions ($T = 298\,\mathrm{K}$ mixtures with 2H1D, $T = 295\,\mathrm{K}$ mixtures with 2B1O). Reprinted with permission from S. P. Bierwirth et al, Physical Review E, 90 052807 (2014) Copyright (2014) by the American Physical Society.

if the microscopic distances in the mixtures reflect in the overall density of the liquid, these values were compared to the macroscopic densities which were transformed into the deviation from a linear mixing behavior $\Delta\rho$ in the exact same manner and are also shown in figure 5.11. In the case of $\Delta d_\mathrm{mp}$ the distance is shorter than expected from the linear mixing behavior, which reflects the increased density in the mixture that can be observed via $\Delta\rho$. The macroscopic densities $\rho$ were measured by employing the Anton Paar DSA 5000. The non-linear behavior of $\Delta d_\mathrm{mp}$ was observed for both mixtures and might be due to the different sizes of the corresponding neat alcohols causing a more efficient packing of the molecules which is supported by the fact that the deviation is stronger in mixtures with 2H1D which is a bigger molecule than 2B1O. In contrast to that, the distance between the oxygen atoms characterized by $d_\mathrm{pp}$ deviates in the oppositional direction. So the overall liquid becomes denser but the distance between the oxygen atoms increases. This can be explained by a chain-to-ring transition in the mixture. Figure 5.12 illustrates the different supramolecular arrangements in neat 4M3H, and in a mixture of 4M3H and 2H1D and the increasing distance between the oxygen atoms of these arrangements. In ringlike supramolecular structures, the outwards radiating alkyl chains produce a more open hydrophobic shell around their polar hydroxyl cores than in chainlike aggregates. In the chain like mixtures, the alkyl chains
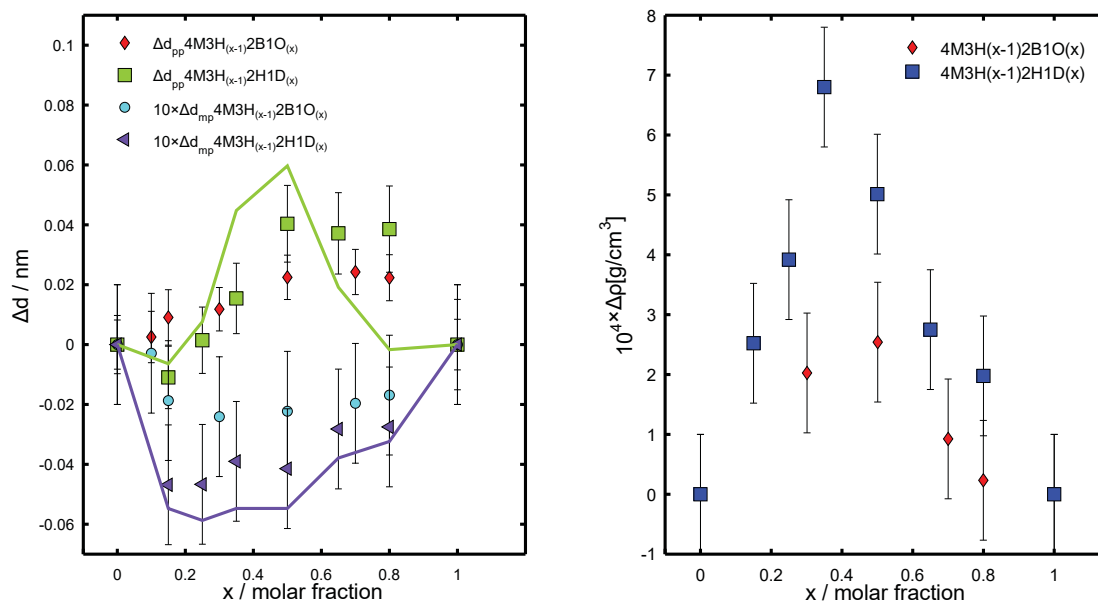
**Figure 5.11:** Deviation from a linear mixing behavior of the correlation lengths belonging to the main and prepeak of the mixtures of 4M3H with 2B1O and 2H1D $\Delta d_{pp}$ and $\Delta d_{mp}$. The lines present the results obtained by a different fitting routine to verify the error bars (left), and the deviation from a linear mixing behavior of the macroscopic density $\Delta \rho$ of the same mixtures (right). Reprinted with permission from S. P. Bierwirth et al, Physical Review E, 90 052807 (2014) Copyright (2016) by the American Physical Society.

are well ordered and so they act as a better spacer between the oxygen cores of the supramolecular clusters as depicted in figure 5.11. The deviation of $d_{pp}$ from a linear mixing behavior is stronger in mixtures of 4M3H with 2H1D for which also a stronger enhancement of the Debye process is known compared to the mixing of 4M3H with 2B1O. The transformation from rings to chains also reflects in the mixing behavior of $\sigma$ and $I$ of both peaks. The relative change of $I$ and $\sigma$ of both peaks due to diluting neat 4M3H with 2H1D and 2B1O is presented in figure 5.13. The prepeak intensity decreases due to mixing. A nonlinear behavior similar to the behavior of $d_{pp}$ could be observed. Additionally, $\sigma_{pp}$ broadens in the mixture, so that it can be concluded that the chainlike structures are less defined than the ringlike structures, which is in line with the assumed structure model (presented in figure 5.12) and has also been observed in the homologous series. A decrease of the prepeak intensity and a broadening is found to be a signature of a transition to chainlike clusters. In contrast to that, $I_{mp}$ increases slightly due to diluting with 2H1D and 2B1O, which is accompanied by a linear variation of $\sigma_{mp}$ in both cases. So the local ordering between the carbon atoms is less affected than the correlation between the oxygen atoms.
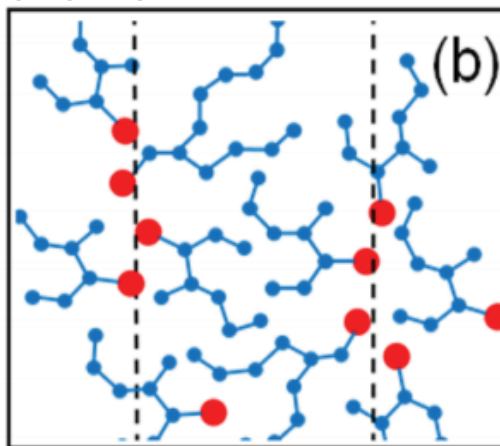
# rings
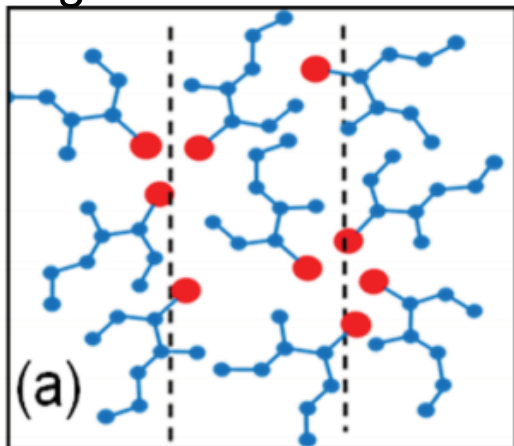
# chains



**Figure 5.12:** Illustration of the typical distance between oxygen cores of the supramolecular clusters which are indicated by lines. Reprinted with permission from S. P. Bierwirth et al, Physical Review E, 90 052807 (2014) Copyright (2016) by the American Physical Society.
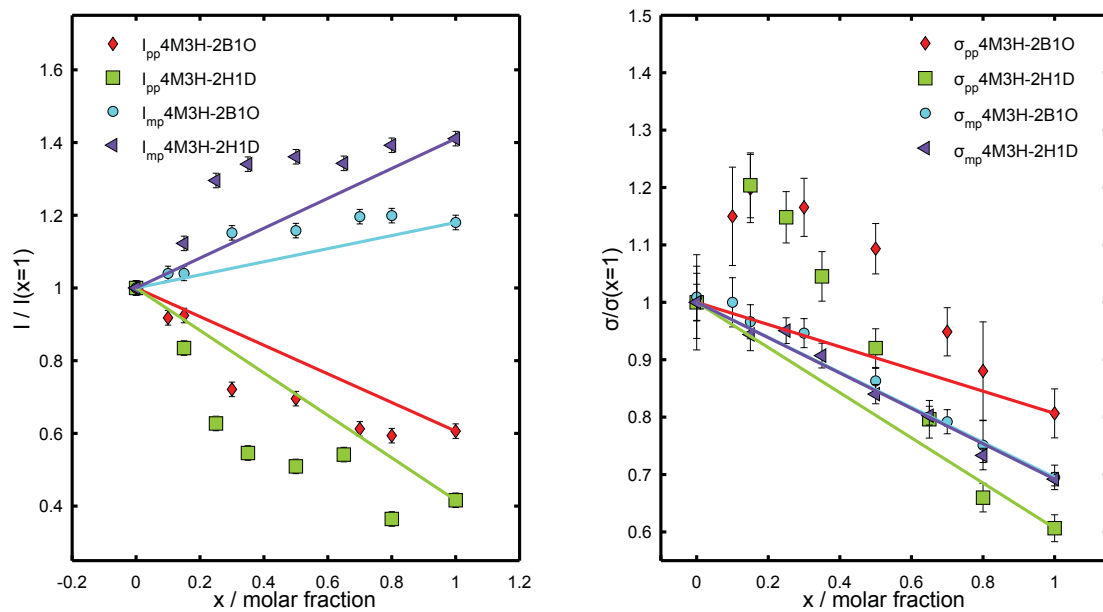
**Figure 5.13:** Relative change of $I$ and $\sigma$ of the prepeak and the main peak due to diluting neat 4M3H with 2H1D and 2B1O. The lines are connecting the neat liquids displaying a linear mixing behaviour.

## 5.5 Temperature and pressure dependence of 4M3H and 2E1H

In this section, the results of the XRD measurements on the isomers of octanol, 2-ethyl-1-hexanol (2E1H) and 4-methyl-3-heptanol (4M3H) over a wide range of pressure $p$, temperature $T$ and wave vector transfer $q$ are presented. From e.g. dielectric spectroscopy it is known that these alcohols form supramolecular structures via H-bonds with different topologies due to the different positions of the hydroxyl group in the molecule. In 2E1H it is located in a terminal position leading to chainlike supramolecular structures (Gainaru et al., 2010), while 4M3H is forming ringlike clusters because the hydroxyl group is located in the center of the molecule and thus screened by the alkyl chain (Singh and Richert, 2012). Figure 5.14 shows a sketch of this model system. It gives rise to the typical two-peak structure in the low $q$-regime which has already been investigated in the sections before. Both peaks yield information about the correlation on a medium range order, e.g. its position can be transformed into a real space distance by $d = 2\pi/q$.
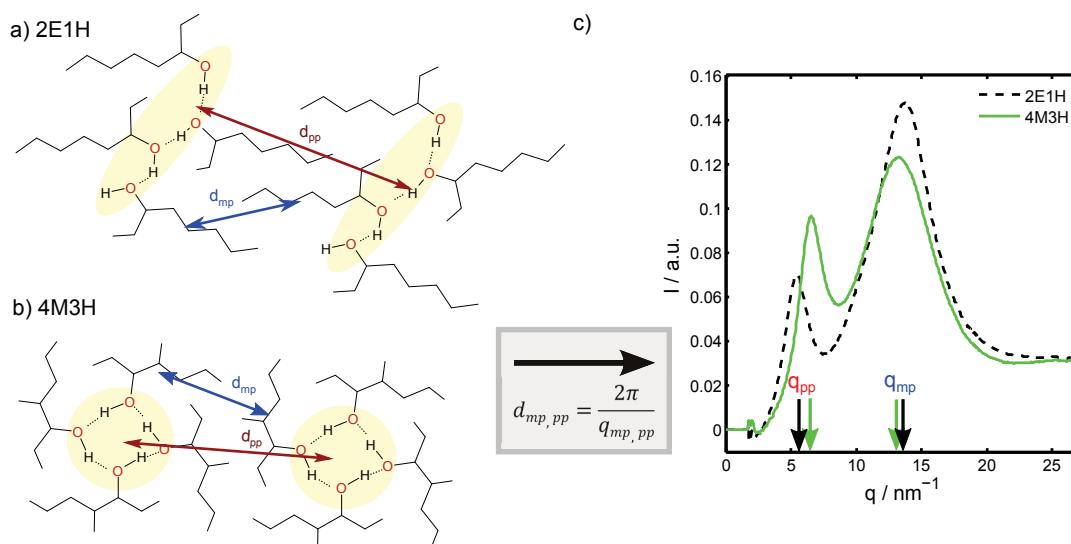


**Figure 5.14:** a,b) Supramolecular chains (a) and rings (b) formed by 2E1H (a) and 4M3H (b) molecules. The typical distance between carbon atoms $d_{\mathrm{mp}}$ and oxygen atoms $d_{\mathrm{pp}}$ in supramolecular clusters are indicated by arrows.

Studying linear alcohols by computer simulations has shown that the molecules form chainlike supramolecular arrangements (Lehtola et al., 2010) which is the origin of the two-peak structure in the liquid structure factor. Since the main peak is caused by the correlation of the carbon chains and the prepeak is due to the oxygen-oxygen correlation (Tomsic et al., 2007), exploring the behavior of both peaks can provide insights into the

H-bonded structure formation on a medium range level. Additionally, XRD patterns of 4M3H and 2E1H measured over a wide $q$-range up to $q = 160\,\mathrm{nm}^{-1}$ are presented, which allows performing a PDF analysis to study short-range ordering.

It is known from literature that ring forming arrangements take a higher volume per molecule than chainlike structures i.e. they are less dense (Böttcher, 1973; Vij et al., 1981). In particular, a higher density in 2E1H is expected, but surprisingly the density is slightly higher in 4M3H at room temperature, where $\rho_{2\mathrm{E1H}} = 0.8326 \pm 0.0001\,\mathrm{g/cm}^3$ and $\rho_{4\mathrm{M3H}} = 0.8332 \pm 0.0001\,\mathrm{g/cm}^3$ were measured at $T = 293\,\mathrm{K}$ but it has to be pointed out that the difference was just slightly out of the errorbars. Interestingly, there was a deviation from the values that can be found in the literature, $\rho_{2\mathrm{E1H, lit}} = 0.830\,\mathrm{g/cm}^3$ and $\rho_{4\mathrm{M3H, lit}} = 0.7940\,\mathrm{g/cm}^3$ (Yaws, 2014), and on various websites of e.g. chemical suppliers $\rho_{2\mathrm{E1H, web}} = 0.833\,\mathrm{g/cm}^3$ and $\rho_{4\mathrm{M3H, web}} = 0.827\,\mathrm{g/cm}^3$ (ChemicalBook, 2016), all measured at $T = 298\,\mathrm{K}$. Consequently, it cannot be verified if there is a real difference between the densities of the liquids[2]. Figure 5.15 shows, that the difference between the densities increases with decreasing temperature from $298\,\mathrm{K}$ to $278\,\mathrm{K}$.

However, on a microscopic scale the diffraction images of 2E1H and 4M3H at room temperature (see figure 5.14) support the idea of different supramolecular structures. The main peak is observed at higher $q$-values in 2E1H than in 4M3H, supporting the idea of chainlike supramolecular structures where the carbon chains are supposed to be denser packed. The prepeak appears at lower $q$-values because the carbon chains act as a better spacer between the oxygen cores. In a nutshell, the microscopic structure exploited by XRD supports the assumption of supramolecular chains in 2E1H and rings in 4M3H but a connection to the macroscopic density cannot be verified. In the following, an XRD study in the temperature range from $135 - 380\,\mathrm{K}$ and in the pressure range from ambient up to $4500\,\mathrm{bar}$ is presented. From dielectric spectroscopy it is known that the Debye process develops in oppositional directions due to the application of high pressures (Pawlus et al., 2013). It increases in 4M3H and decreases in 2E1H, which is widely accepted to be an indication of a change of the dominant supramolecular structure measured via the collective dipole moment of the clusters. Following this, it is hypothesized that the supramolecular chains in 2E1H are destabilized leading to shorter chain fragments and the rings in 4M3H break up into chainlike ring fragments. While dielectric spectroscopy measures dynamic properties, XRD is valuable to obtain static information about typical distances that may support or contradict these assumptions. Furthermore, it is applicable over a wide range of temperature where the dynamics are too fast for dielectric spectroscopy.

---

[2]It is necessary to consider the experimental and systematic uncertainties in the estimation of the densities. Therefore, the density measurement should be performed with a different equipment in a different place with chemicals obtained from different suppliers, which was not possible within the time frame of this thesis
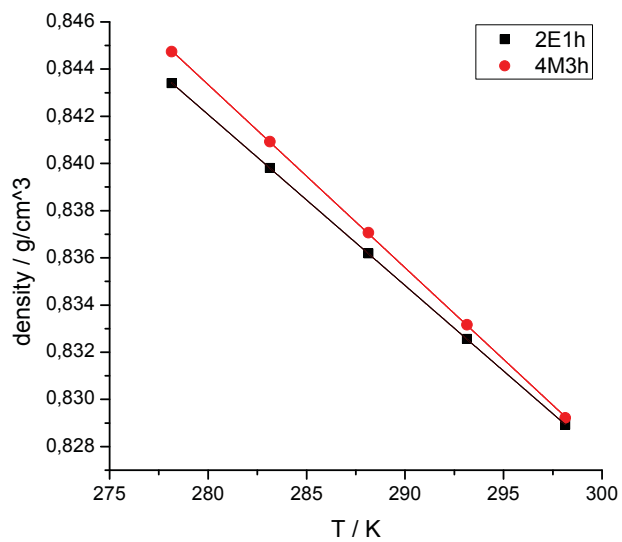
**Figure 5.15:** Density of 2E1H and 4M3H measured in the temperature range from 278 K to 298 K and linear regression curves.

### 5.5.1 2E1H and 4M3H at high pressure

As described in the experimental section, the high pressure is transmitted by water that surrounds the sample cell. Ergo, a superposition of scattering from water and alcohol was measured, which was considered in the data analysis. First, the background scattering of an empty capillary was subtracted from all the diffraction patterns as described in the experimental section. Figure 5.16 shows the resulting diffraction patterns of 2E1H (raw 2E1H) at ambient pressure at $298\,$K as well as the pure water signal at the same pressure and temperature.
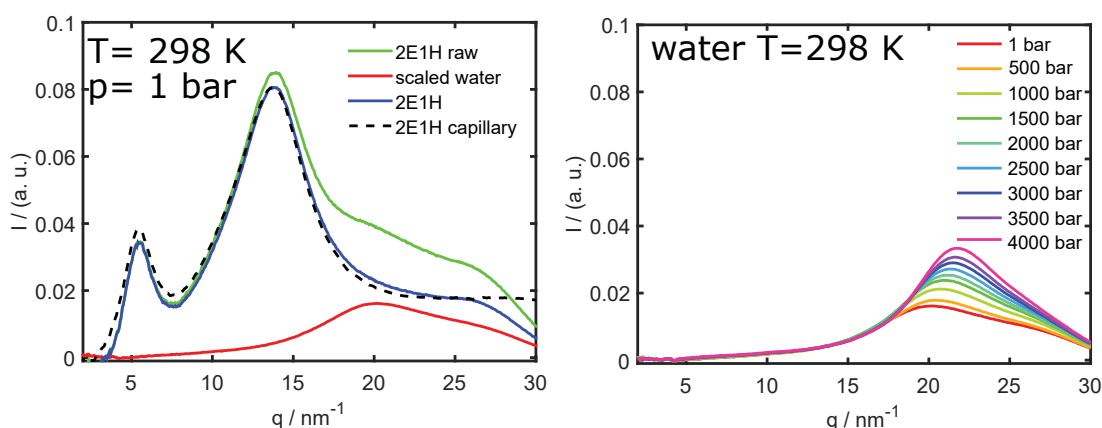


**Figure 5.16:** Subtraction of the water signal from the measured intensity (left). XRD patterns of water in the range from $1 - 4000\,$bar at $298\,$K (right).

Before the subtraction, the water signal was scaled in a way that the difference signal is most similar to a diffraction pattern measured by employing a capillary. The scaling factor was chosen in a way that the resulting intensity has a similar value at $q = 20\,$nm$^{-1}$. As presented in figure 5.16, the shape of the water signal changes with increasing pressure and the ratio of water to alcohol increases because of the lower compressibility of alcohol compared to water. If the scaling factor of water increased too strongly from one pressure point to the next it was evidence for a broken Kapton window because the alcohol mixed with the surrounding water, which was clearly distinguishable from the effect of different compressibilities of water and alcohol. During the analysis, it could be noticed as a discontinuously increasing portion of scattering contribution originating from the water. The broken Kapton windows were also noticed when the sample cell was opened after the measuring series. Such diffraction patterns were not considered in the following data analysis (2E1H $T = 343\,$K $p > 3000\,$bar, 4M3H $T = 276\,$K $p > 3500\,$bar, $T = 303\,$K $p > 2000\,$bar, $T = 343\,$K $p > 3000\,$bar). It has to be emphasized that this is defective and thus it was tested that the obtained final results are stable against small changes of the background subtraction. This can be rationalized

by the fact that the main scattering contribution of water arises at $q > 15\,\mathrm{nm}^{-1}$ and consequently there is nearly no effect on the prepeak. The effect of the water subtraction on the main peak is more significant. After background subtraction, the diffraction patterns were normalized and fitted by two Pearson VII functions as described before to determine the peaks' positions, intensities, and widths. Figure 5.17 shows the diffraction patterns of 2E1H and figure 5.18 the diffraction patterns of 4M3H at temperatures of $276\,\mathrm{K}$, $298\,\mathrm{K}$, $303\,\mathrm{K}$ and $343\,\mathrm{K}$ normalized to constant area in the range from $4-20\,\mathrm{nm}^{-1}$. At each temperature the pressure was increased in steps of $500\,\mathrm{bar}$ until the maximal pressure of $4500\,\mathrm{bar}$ was reached. The measurements at $298\,\mathrm{K}$ were only performed at pressures up to $4000\,\mathrm{bar}$.
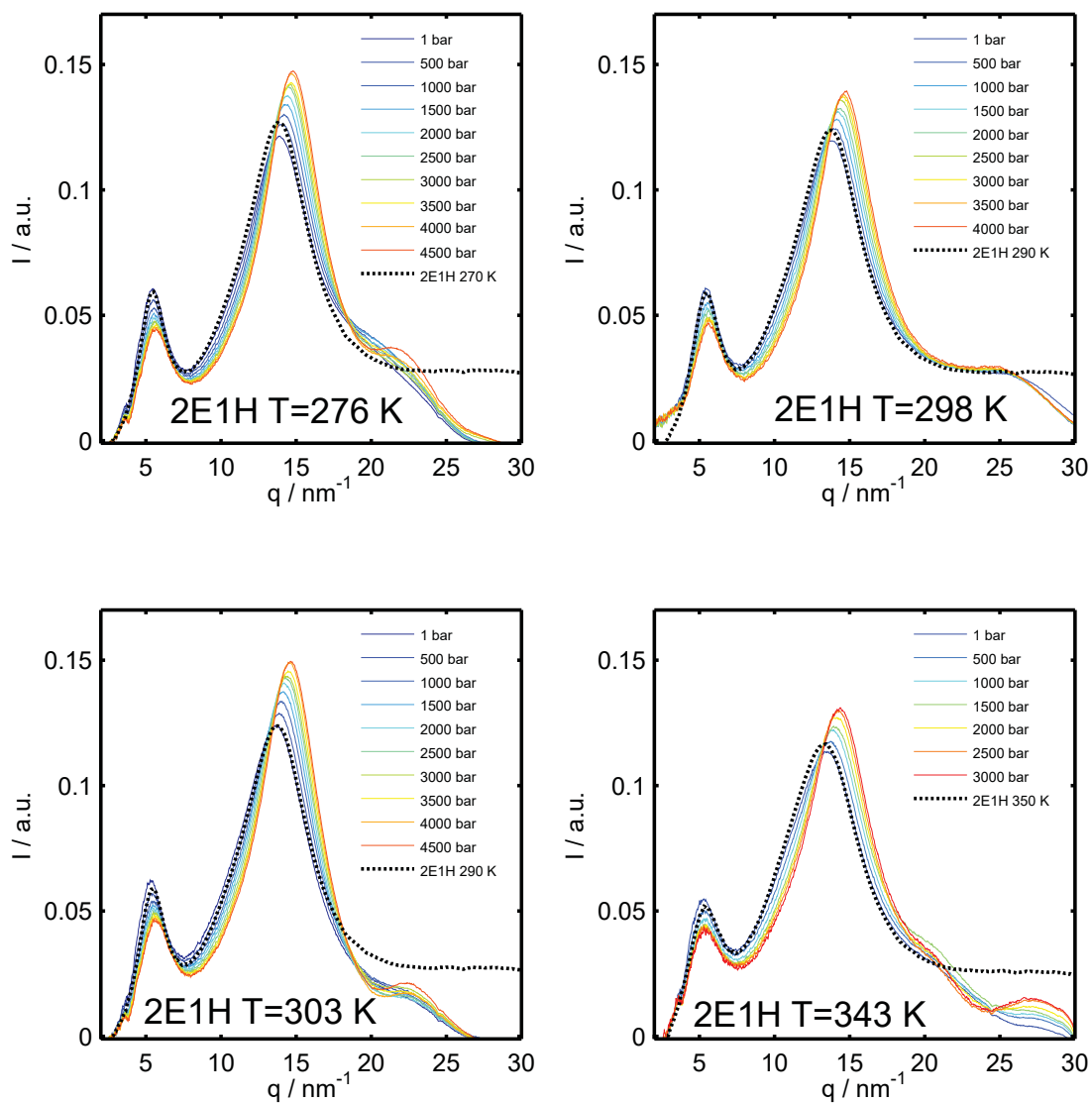
**Figure 5.17:** Diffraction patterns of 2E1H at temperatures of 276 K, 298 K, 303 K and 343 K and pressures up to 4500 bar.

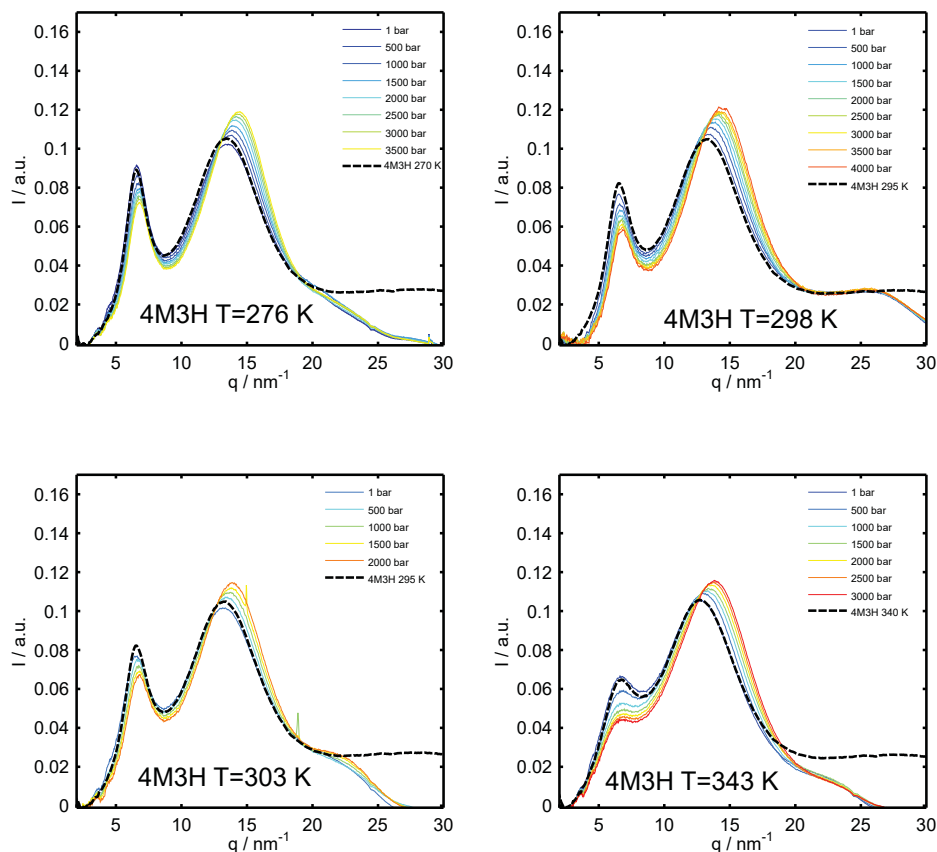**Figure 5.18:** Diffraction patterns of 4M3H at temperatures of $276\,\text{K}$, $298\,\text{K}$, $303\,\text{K}$ and $343\,\text{K}$ and pressures up to $4500\,\text{bar}$.

In the following, the fitting parameters extracted from the measurements at $298\,\text{K}$ and $303\,\text{K}$ are presented as an averaged data set at $300\,\text{K}$ since the relative changes of the fitting parameters do not differ significantly. First, the focus is set on the main diffraction peak at $q \approx 14\,\text{nm}^{-1}$ which is due to the correlation between carbon atoms and therefore the microscopic volume calculated from its position $V_{\text{mp}} = (2\pi/q_{\text{mp}})^3$ correlates with the overall density $\rho_{\text{mac}}$ of the liquid. The relative change of the microscopic volume $V_{\text{mp}}/V_{\text{mp}}(\text{p=1 bar})$ from ambient conditions at increasing pressure is presented in figure 5.19. A solid line displays the expected behavior which can be calculated by using the isothermal compressibilities $\chi_{\text{T,2E1H}} = 7.532 \cdot 10^{-5}\,\text{bar}^{-1}$ and $\chi_{\text{T,4M3H}} = 8.202 \cdot 10^{-5}\,\text{bar}^{-1}$ at $T = 298\,\text{K}$ (Yaws, 2014). As expected, the volume change is stronger at higher temperatures. A good agreement with the theoretical value

52

is observed up to pressures of 1500 bar. At higher pressures, the compression is weaker, which is simply explained by the fact that the model of a linear compression is not sufficient anymore. In general, the volume, respectively the density, is connected to pressure and temperature via the Tait equation (Dymond and Malhotra, 1988). The work of (Reiser et al., 2010) deals with 2E1H at high pressures and the authors determined the Tait equation for the volume change of 2E1H at a constant temperature $T_0$

$$\frac{V(T)}{V_0(p_0,T_0)} = 1 - A \cdot \log((B(T) + p)/(B(T) + p_0)) \tag{5.4}$$

with the constants $A = 0.091$ and $B = 348\mathrm{MPa} - 0.786\mathrm{MPa/K} \cdot T$. Figure 5.19 a) shows that the nonlinear behavior of the relative volume change is reasonably reproduced by the Tait equation but the changes are underestimated. The reason for this is that the overall density is dependent on all distances in the liquid and not the carbon correlations only. As a nearby next step, the oxygen distances obtained from the prepeak can be used to complement the model by using a superposition of the microscopic volumes extracted from both diffraction peaks $V_{\mathrm{mp}}$ and $V_{\mathrm{pp}} = (2\pi/q_{\mathrm{pp}})^3$. Figure 5.19 b) shows that a weighted sum of $0.85 \cdot V_{\mathrm{mp}} + 0.15 \cdot V_{\mathrm{pp}}$ fits the Tait equation quite well and even better than a weighting with the percentage of oxygen and carbon atoms in the liquid. For an exact determination of the density, it would be necessary to consider all distances, which is not possible with this technique. However, the results encourage the interpretation that the main peak tracks the density changes in MAs but not the absolute density. This motivates to fit these function to the data measured for 4M3H to obtain the values for $A$ and $B(T)$. These fits are presented in figure 5.19 c). This allows to determine the Tait equation parameters via averaging $A = 0.091$ and $B = 348 \pm 0.1\mathrm{MPa} - (0.845 \pm 0.005\,\mathrm{MPa/K}) \cdot T$. The Tait equation determined for 4M3H exhibits a stronger temperature dependence than in 2E1H. In summary, it can be said that the structure formation in the liquid is responsible for the deviation from the behavior measured with other macroscopic techniques and can be explained partly taking the prepeak into account. More importantly, the good agreement with the theoretical curve verifies that the subtraction of the underlying water signal was done correctly.

The behavior of the main diffraction peak is in line with former neutron diffraction studies (Trabelsi et al., 2008; Bellissent-Funel et al., 1997; Weitkamp et al., 2000) on hydrogen-bonded liquids. These studies have shown a weak pressure dependence of the static structure factor, a shift of the main diffraction peak to higher $q$-values and a slight increase in intensity. The increase of the main peak's intensity corresponded to the increased density of the liquid at high pressure and was also observed in all diffraction patterns of 2E1H and 4M3H (see figure 5.20).
Surprisingly, the prepeak behaves quite differently. Figure 5.20 shows the relative changes of the correlation length $d$, intensity $I$ and FWHM $\sigma$ of the prepeak, which are displayed with icons. The corresponding values of the main peak, except for the main peak's correlation lengths, are displayed with lines. There are only a few studies dealing with the prepeak in hydrogen bonded liquids at high pressures. These studies have
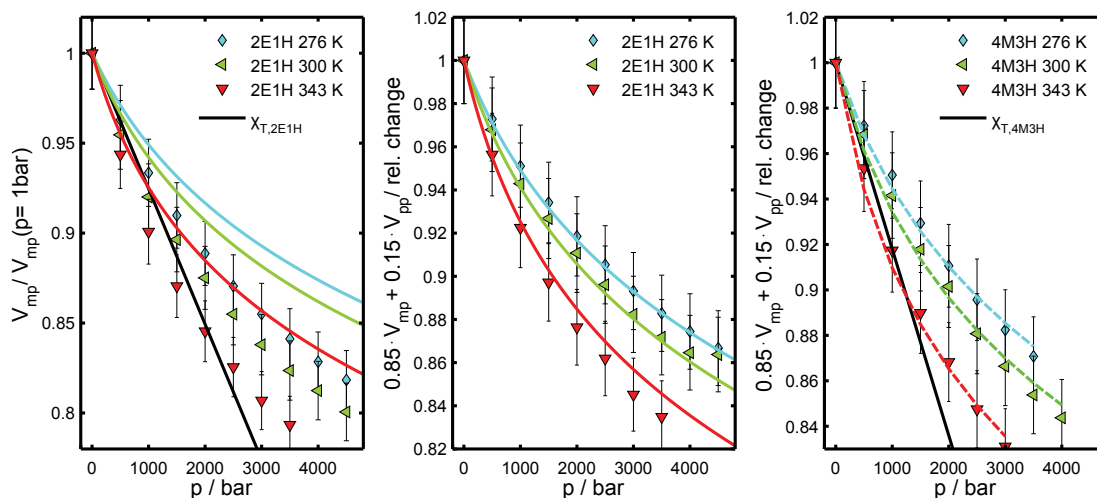
**Figure 5.19:** The figure on the left shows the relative change of the volumes $V_{\mathrm{mp}}$ calculated from the main peak's position $q_{\mathrm{mp}}$ of 2E1H at temperatures of 276 K, 300 K and 343 K at pressures up to 4500 bar and the reduction of the volume calculated from the isothermal compressibility $\chi$ at 298 K of 2E1H and 4M3H. The continuous lines depict the volume change measured by (Reiser et al., 2010) employing the Tait equation. The figure in the middle shows the same data as the figure on the left and proportionally added volumes corresponding to the main and the prepeak $0.85 \cdot V_{\mathrm{mp}} + 0.15 \cdot V_{\mathrm{pp}}$ as lines, which are in agreement with the results. On the right-hand side of the figure the corresponding data for 4M3H is diagrammed, the dashed lines are fits employing the Tait equation.

found that the prepeak is hardly affected by high pressure. For example, in m-toluidine a small decrease of its intensity at increasing pressure has been observed (Morineau and Alba-Simionesco, 1998). Figure 5.20 shows, that clear changes can be observed in the prepeak of 2E1H and 4M3H with increasing pressure, especially compared to the main peak. The typical distance calculated from the prepeak's position $d_{\mathrm{pp}}$ shrinks with increasing pressure, which implies a shortening of the distance between H-bonded clusters in both MAs. This is the same behavior as observed for the main peak and was discussed in terms of $V_{\mathrm{mp}}$. The increased pressure reduces the volume and consequently all distances in the liquid.

In contrast to the similar behavior of the shift of both peaks, leading to a relative decrease of $d_{\mathrm{pp}}$ and $V_{\mathrm{mp}}$, an oppositional behavior of the peak intensities $I_{\mathrm{mp}}$ and $I_{\mathrm{pp}}$ was observed. Figure 5.20 shows that $I_{\mathrm{pp}}$ decreases about 20 %, while $I_{\mathrm{mp}}$ increases slightly or remains more or less at a constant level over the whole pressure range. The decrease of about 20 % indicates a reduction of the mean number of H-bonded clusters (Hédoux et al., 2013) and so an increase of unbounded monomers at all temperatures in both liquids.

The FWHM $\sigma$ of a diffraction peak defines the degree of local order of the structure that causes the peak in the liquid (Shmyt'ko et al., 2010). The main peaks become narrower

in 2E1H with increasing pressure because the alkyl chains become more densely packed if the available space is reduced. This effect is weaker in 4M3H and at the highest temperature 343 K a broadening of the main peak can be observed. Now the prepeaks FWHMs $\sigma_{\mathrm{pp}}$ are discussed. Except for the data series taken at 343 K a narrowing of the prepeak in 4M3H and a broadening in 2E1H at increasing pressures is observed at all temperatures. 4M3H is at 343 K so far disintegrated that nearly no prepeak can be observed anymore.
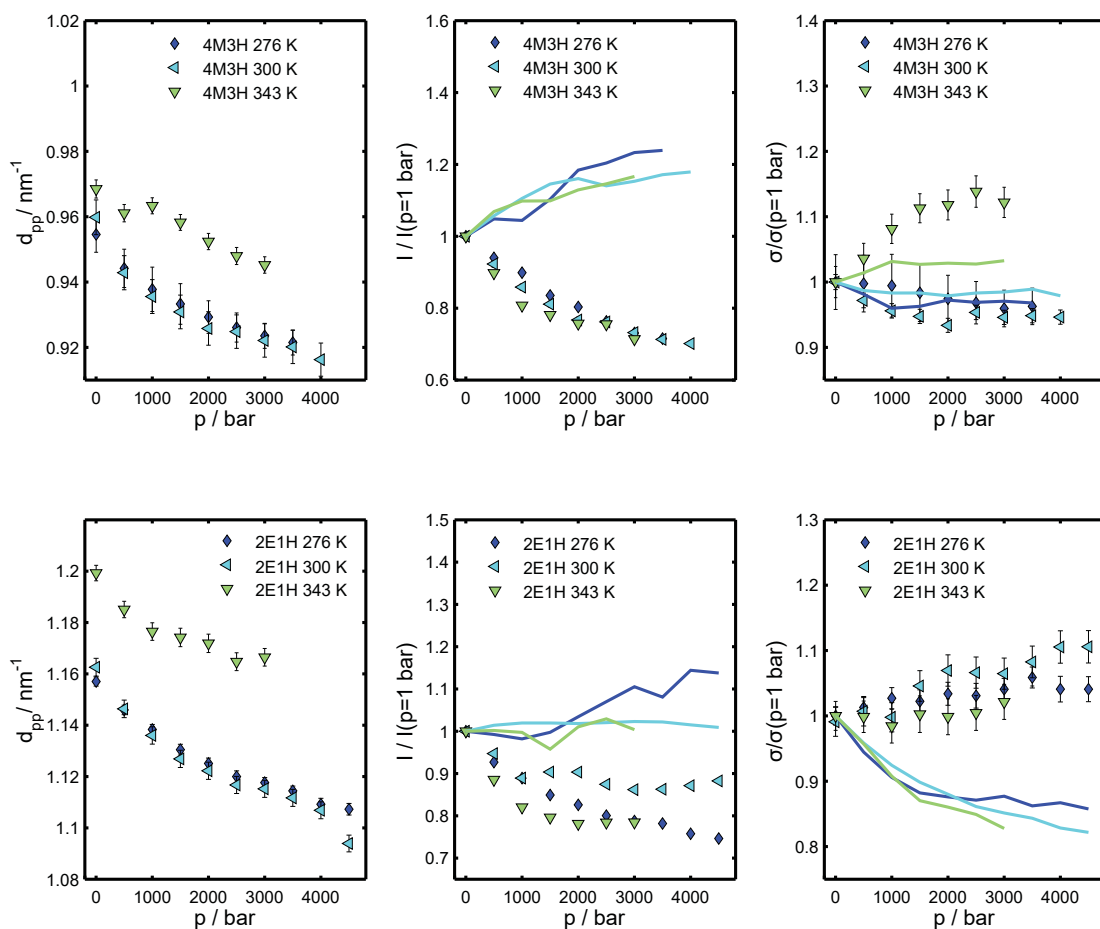


**Figure 5.20:** Prepeak correlation length $d_{\mathrm{pp}}$, relative change of main and prepeak intensity $I$ and relative change of FWHM $\sigma$ of 2E1H and 4M3H in the range from $1 - 4500\,\mathrm{bar}$ at temperatures of $276\,\mathrm{K}$, $300\,\mathrm{K}$ and $343\,\mathrm{K}$.

This can be rationalized by considering the prepeaks' widths on an absolute scale (see figure 5.21 a). The widths of the prepeaks converge each other at increasing pressure at a temperature of $276\,\mathrm{K}$. At 3500 bar the width of the prepeak is $\approx 1.98\,\mathrm{nm}^{-1}$ in both MAs. It was not possible to determine the evolution for pressures higher than 3500 bar at this

temperature because of a broken Kapton window. Intuitively, one would suggest that the destruction of supramolecular structures and therefore the increase of monomers due to the application of high pressure, as indicated by the decreasing prepeak intensity, would increase the FWHM as seen for 2E1H. However, the prepeak's FWHM of 4M3H shows the opposite trend and the FWHMs of 2E1H and 4M3H approach each other at high pressure. This can be understood by cutting structures. The local disorder increases in 2E1H due to the destruction of the supramolecular chainlike structure. The local order increases in 4M3H because small chainlike fragments are formed on cost of ringlike structures, which show in general a larger FWHM, as pictured in figure 5.21 b). The original structure at ambient conditions differs significantly between the two MAs, while the structures disturbed by the influence of pressure are more alike. This is also in line with the observation of an increasing Debye process in 4M3H and a decreasing Debye process in 2E1H (Pawlus et al., 2013). Figure 5.21 b) shows, that at 300 K a similar behavior can be observed, the widths converged each other up to 4000 bar but the same value is not reached. This can be explained by temperature-induced disturbance of supramolecular structures which reduces the number of clusters and increases the number of monomers. Finally, at the highest temperature of 343 K the width of both peaks differ significantly. The difference increases with increasing pressure because of the increased amount of unbounded molecules which is also indicated by the strong decrease of the prepeak intensity. This strong temperature dependence for 4M3H will be discussed in more detail in the next section. It is important to mention that the structures are significantly smaller at high pressures than at ambient conditions, which is an information that is only accessible with XRD. Because of the limited scattering angle of the high-pressure cell, it was not possible to obtain data over a wide $q$-range to do a PDF analysis at high pressures. This might be interesting for further analysis because these results do not yield the information which fundamental mutual reaction causes this reorganization. A destabilization of H-bonds or a disturbance by the unfavorable arranged alkyl chains are possible explanations.
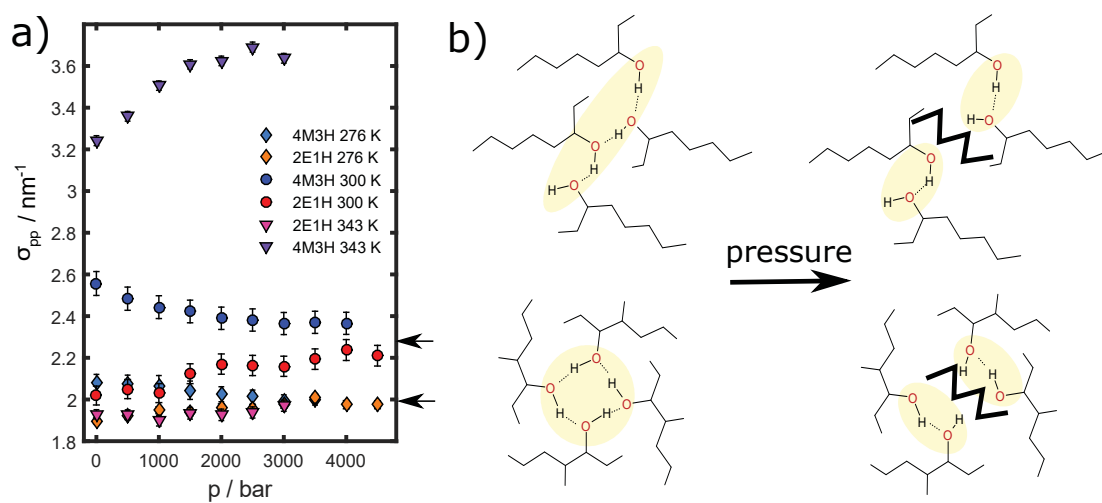
**Figure 5.21:** a) Absolute values of $\sigma_{pp}$ of 2E1H at temperatures of 276 K, 300 K and 343 K and the low temperature data of 4M3H at 276 K, and 300 K, b) Illustration of the model system. H-bonds are painted with dotted lines, the oxygen cores of supramolecular arrangements are colored in yellow. Pressure cuts H-bonds in MAs. The resulting fragments are more similar than the original clusters.

### 5.5.2 2E1H and 4M3H over a wide range of temperature

The previous chapter indicated that the structuring in 4M3H and 2E1H is strongly dependent on the temperature. This motivated to measure XRD patterns of 2E1H and 4M3H in the temperature range of $135-380\,\mathrm{K}$ at ambient pressure. Furthermore, 2E1H exhibits a nonlinear temperature dependence of the Debye process asking for a structural explanation on molecular level (Gainaru et al., 2011). The XRD patterns were collected at ID22 at the ESRF, allowing to access a wide $q$-range up to $160\,\mathrm{nm}^{-1}$, and are presented in figure 5.22. The typical two-peak structure of MAs is well resolved but due to the wide $q$-range more information about the short range order is accessible. In the following, the medium range order is discussed and the focus of the next chapter is on the additional short range order information. The medium $q$-range is presented as an inset of figure 5.22. After a background subtraction of the contributions of scattering from the capillary and the surrounding air, the XRD patterns were normalized to a constant area in the range of $4-20\,\mathrm{nm}^{-1}$. Both peaks of the medium $q$-range were analyzed as it was done for the pressure measurements and the results are presented in figure 5.23. Similarly to the effect of increasing pressure, the characteristic distances assigned to the main peak $d_{\mathrm{mp}}$ and prepeak $d_{\mathrm{pp}}$ shift to smaller values due to cooling, indicating an increasing density and denser packing of supramolecular arrangements due to the less thermal motion. Surprisingly, a clear change of slope is observed at about $250\,\mathrm{K}$ in $d_{\mathrm{pp}}$ as shown in figure 5.23. Beyond $250\,\mathrm{K}$ $d_{\mathrm{pp}}$ decreases more rapidly in 2E1H, while in 4M3H the position of the prepeak hardly varies until a further decrease sets in below $160\,\mathrm{K}$. The Latter is suggested to be due to the glass transition of 4M3H at $164\,\mathrm{K}$ (Singh et al., 2013) causing a different compressibility of supramolecular arrangements. The glass transition of 2E1H occurs at $145\,\mathrm{K}$ (Wang and Richert, 2005), which is at the limit of the temperature range studied in this work and thus difficult to observe. A change of slope at $\approx 250\,\mathrm{K}$ is well resolved in both MAs. The oppositional change of the alteration rate leads to the assumption that different kinds of supramolecular arrangements with different compressibilities are formed.

The intensity of the main peak $I_{\mathrm{mp}}$ decreases due to heating in 2E1H and 4M3H like the Debye-Waller factor predicts and is observed in non-associating molecular liquids like e.g. benzene and octane (Skinner, 1930) until a temperature of $\approx 290\,\mathrm{K}$ is reached. This is caused by the thermal movement of the molecules. A further increase of the temperature leads to an increase of $I_{\mathrm{mp}}$ in 4M3H but not in 2E1H, which might be due to the formation of monomers on the cost of supramolecular structures. Interestingly, the temperature dependence of $I_{\mathrm{pp}}$ differs significantly from a Debye-Waller-like behavior in both MAs. $I_{\mathrm{pp}}$ increases up to a temperature of $250\,\mathrm{K}$ in 4M3H and $300\,\mathrm{K}$ in 2E1H. Such a non Debye-Waller-like behavior has been observed for various amorphous materials and is interpreted as a signature of a medium range structuring beyond the usual short-range order, for example in covalent amorphous solids (Elliott, 1991). The microscopic origin of the increasing scattering intensity in the prepeak at increasing temperature is not conclusively enlightened. This oppositional behavior has been observed in molten sodium carbonate (Wilding et al., 2016), liquid m-toluidine (Morineau and Alba-Simionesco, 1998) and ionic liquids (Kashyap et al., 2012) and is
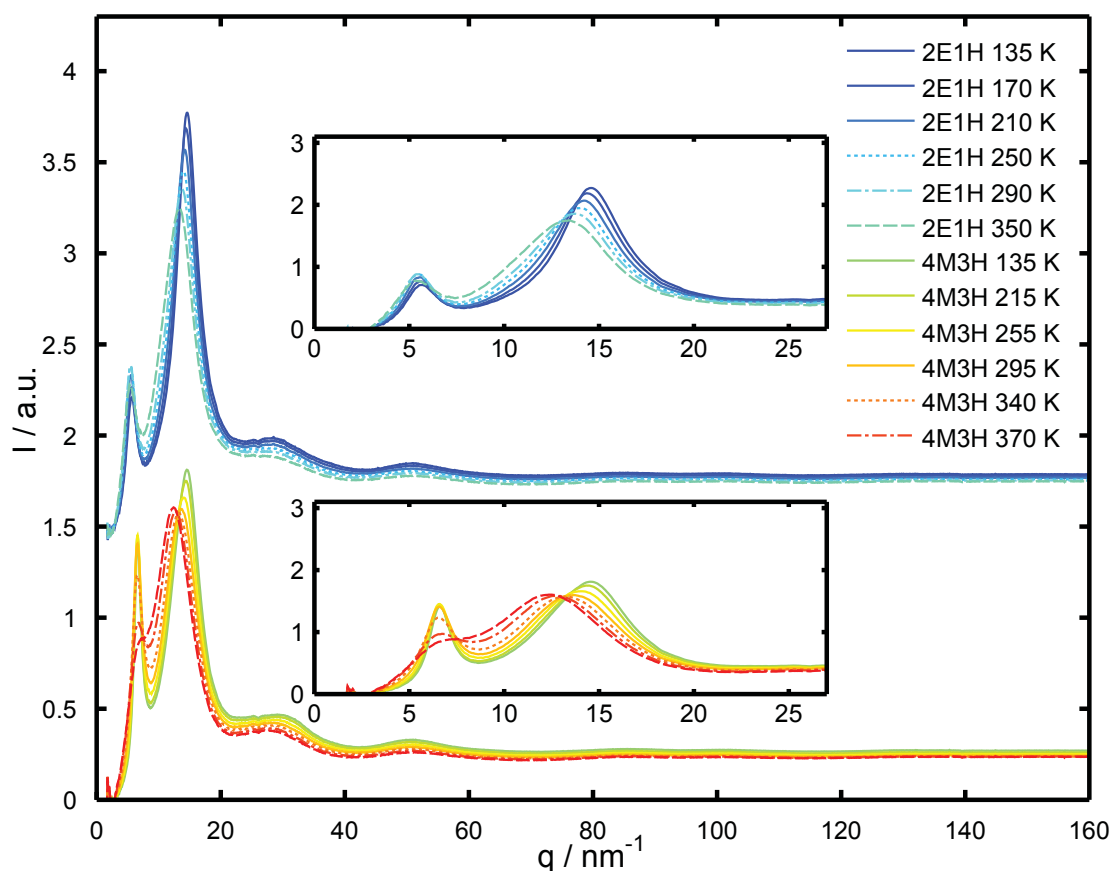
**Figure 5.22:** Selected XRD patterns of 2E1H and 4M3H over a wide $q$-range measured at temperatures as indicated. The insets show the medium $q$-range which was used for peak fitting to analyze the prepeak.

typical for medium range structures in amorphous matter. At temperatures above 250 K and 300 K, respectively, a normal Debye-Waller-like behavior sets in which indicates a strong increase of monomers at high temperatures due to a destruction of supramolecular structures which is more pronounced in 4M3H.

The main diffraction peak becomes wider with increasing temperature in both alcohols, $\sigma_{\text{mp}}$ raises linearly over the whole temperature range because of rising thermal disorder causing less defined structures. So the ordering in the liquid increased slightly in 4M3H and stays constant in 2E1H which is also supported by the fact that the main peak of both alcohols becomes narrower over the whole temperature range. The prepeak's width $\sigma_{\text{pp}}$ increases in 4M3H and changes hardly in 2E1H with increasing temperature up to 250 K. The ordering of the supramolecular structures seems to be hardly dependent on temperature in 2E1H in the range of $150-250$ K while they get disturbed in 4M3H. At temperatures above 250 K the prepeak becomes broader in both alcohols. The overall

alteration rate is significantly higher in 4M3H which, together with the strong intensity decrease, indicates a destabilization of supramolecular structures by the formation of monomers that is more pronounced in 4M3H. It can be concluded, that in the high-temperature regime the structures get disturbed leading to an increasing amount of monomers, which is consistent with the change of the Kirkwood-factor of both alcohols (Bauer et al., 2013; Böhmer et al., 2014). The different slopes of $d_{\mathrm{pp}}$, $I_{\mathrm{pp}}$ and $\sigma_{\mathrm{pp}}$ are suggested to originate from the different geometrical properties of H-bonded clusters exhibiting different compressibility and local structuring constrained by the alkyl chains.
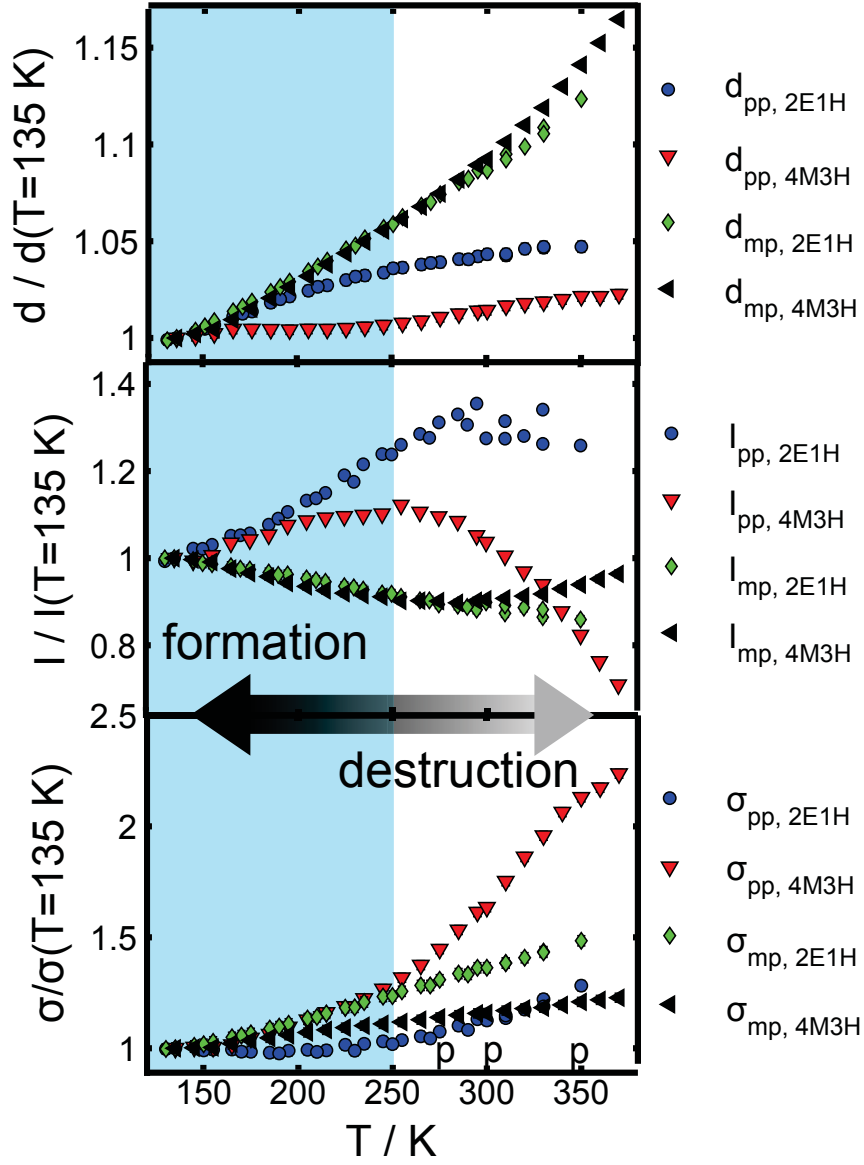
**Figure 5.23:** Properties of the mainpeak and the prepeak (position $d$, intensity $I$, and FWHM $\sigma$ normalized to the value measured at the lowest temperature $T_{\min} = 135\,\text{K}$: $d_{\text{pp,2E1H}}(T = 135\,\text{K}) = 1.1001\,\text{nm}$, $d_{\text{pp,4M3H}}(T = 135\,\text{K}) = 0.9433\,\text{nm}$, $d_{\text{mp,2E1H}}(T = 135\,\text{K}) = 0.4307\,\text{nm}$, $d_{\text{mp,4M3H}}(T = 135\,\text{K}) = 0.4410\,\text{nm}$, $I_{\text{pp,2E1H}}(T = 135\,\text{K}) = 0.1021$, $I_{\text{pp,4M3H}}(T = 135\,\text{K}) = 0.2043$, $I_{\text{mp,2E1H}}(T = 135\,\text{K}) = 1.0555$, $I_{\text{mp,4M3H}}(T = 135\,\text{K}) = 0.8824$, $\sigma_{\text{pp,2E1H}}(T = 135\,\text{K}) = 1.8846\,\text{nm}^{-1}$, $\sigma_{\text{pp,4M3H}}(T = 135\,\text{K}) = 1.4542\,\text{nm}^{-1}$, $\sigma_{\text{mp,2E1H}}(T = 135\,\text{K}) = 4.3328\,\text{nm}^{-1}$, $\sigma_{\text{mp,4M3H}}(T = 135\,\text{K}) = 5.6178\,\text{nm}^{-1}$) gained by a fitting procedure as discussed within the text.

### 5.5.3 Short range order in 2E1H and 4M3H

The analysis of the medium $q$-range presented in the previous chapter indicated different supramolecular structures in the low-temperature regime and their disintegration at increasing temperature above $\approx 300\,\text{K}$. In the following, a PDF analysis with Angstrom resolution of the corresponding XRD patterns is presented. The PDFs were extracted from the measured data employing PDFgetX3 (Kieffer and Karkoulis, 2013) which is a well-suited tool for analyzing data of a sample at different conditions such as varying temperature or pressure. Figure 5.24 shows the PDFs $G(r)$ of 2E1H and 4M3H at $330\,\text{K}$, $245\,\text{K}$, and $135\,\text{K}$. The first peaks are due to intramolecular distances ($\approx 1\,\text{Å}$ O-H and C-H distance, $\approx 1.5\,\text{Å}$ C-O and C-C distances) which do not change with temperature in both alcohols. The region of intra-molecular distances is highlighted in gray. There are clear differences between both alcohols in the region of $\approx 2.2 - 3.2\,\text{Å}$ in the vicinity of the peak at $2.55\,\text{Å}$. This maximum is mainly related to the distance between two H-bonded oxygen atoms (Narten and Habenschuss, 1984). However, it contains also contributions from intramolecular C··O and C··C distances (Vahvaselkä et al., 1995). A deconvolution via a fitting routine would be necessary to extract the oxygen-oxygen coordination number which was not feasible with the current data set and probably for long chained alcohols in general (Vahvaselkä et al., 1995). Nevertheless, a reduced intensity around of $\approx 2.2 - 3.2\,\text{Å}$ in 2E1H compared to 4M3H is observed. The peak arising from the distance between two H-bonded oxygen atoms at $2.55\,\text{Å}$ is more pronounced and slightly shifted to smaller $r$-values in 4M3H which supports the idea of different supramolecular arrangements in 2E1H and 4M3H causing this different bond length. Interestingly, the difference of the $G(r)$ functions between both alcohols becomes smaller with increasing temperature if the $r$-ranges at which O-O distances play a role ($\approx 2.2 - 3.2\,\text{Å}$ and $\approx 4.5 - 6.5\,\text{Å}$) are considered. This supports formation of more similar structures of both alcohols at high temperatures in line with the fragmentation suggested from the prepeak study.

Interpretation of this data together with molecular dynamic (MD) simulations might help to gain further insights into the fascinating topic of structuring in 2E1H and 4M3H but is beyond the scope of this thesis.
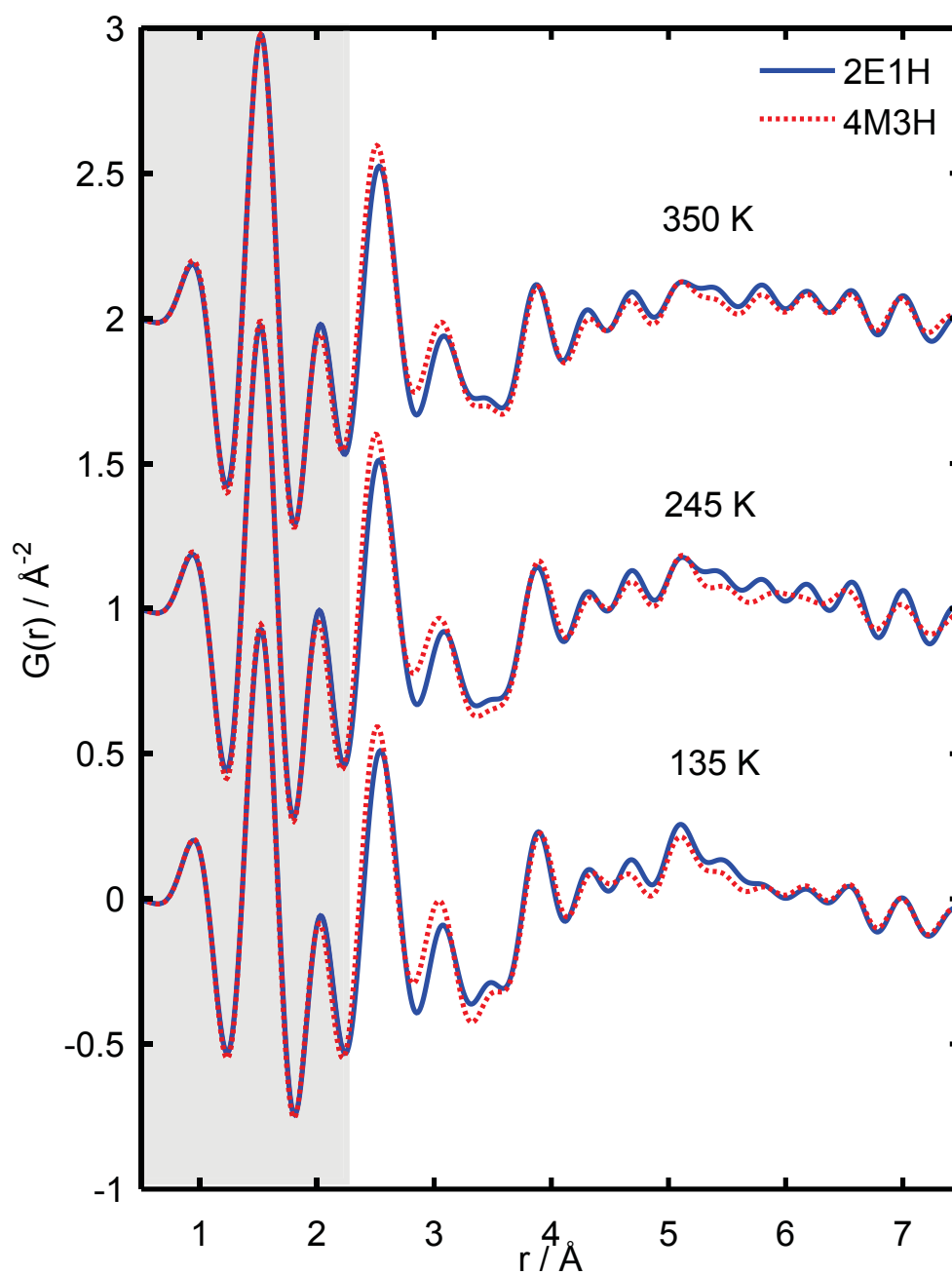
**Figure 5.24:** Reduced pair distribution functions $G(r)$ of 2E1H and 4M3H at temperatures of 350 K, 245 K and 135 K. The intramolecular $r$-region is marked in gray.

## 5.6 X-ray Raman scattering at the oxygen K-edge of mono-hydroxy alcohols

In the following, a study of the oxygen K-edge of MAs and MA mixtures exhibiting different Debye processes is presented. The oxygen K-edge's shape is sensitive to the hydrogen bond network in water (Nilsson et al., 2010; Lehmkühler et al., 2016) and alcohols (Juurinen et al., 2014; Pylkkänen et al., 2010). DFT calculations on methanol clusters (Tamenori et al., 2008) predict a distinct difference between chain- and ringlike bonded molecules. These calculations indicate a slight shift of the main feature at 539 eV to higher energies in the trimer-ring and an increased contribution in the pre-edge region around $535 - 537.5$ eV compared to the trimer-chain. XRS measurements on linear alcohols and their isomers combined with molecular dynamic simulations were used to distinguish between intra- and intermolecular contributions to the oxygen K-edge. A blueshift and broadening of the edge combined with a damping of the pre-edge have been found as a signature of hydrogen bonding (Pylkkänen et al., 2010). This can be seen for example in the spectral differences of 1-butanol, 2-butanol, and isobutanol.

The comparison with octanols might not be perfectly applicable but it demonstrates that the position and the pre-edge region of the oxygen K-edge should be sensitive to differences between chains and rings in MAs. Certainly, a mixture of different structures and monomers will be measured in a real liquid leading to a weaker footprint of a special type of structure in the signature.

XRS was applied on the ring building alcohol 4M3H and the chain building alcohol 2E1H at 273 K. The $S(q,\omega)$ and their differences are presented in figure 5.25. The main absorption



**Figure 5.25:** Oxygen K-edge of chain forming 2E1H and ring building 4M3H measured at ambient conditions.

edge is broadened in 2E1H and the pre-edge feature is less pronounced. The most significant difference between the two alcohols is the damped prepeak intensity in 2E1H. This is in agreement with the expectations for a chainlike supramolecular arrangement (Tamenori et al., 2008) but it has to be mentioned that the differences between 2E1H and 4M3H are weak. Moreover, this can be interpreted as an increase of hydrogen bonding in 2E1H compared to 4M3H (Pylkkänen et al., 2010), which can be explained by the position of the hydroxyl group in the molecule. But there are also intramolecular contributions that strongly affect the XRS spectral shape.
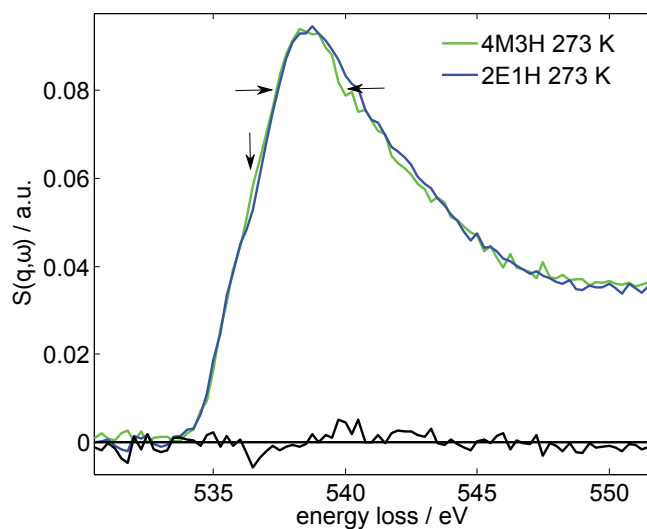
To classify the changes of the spectrum, different isomers of octanols were measured at room temperature. The spectra of 1-octanol, 2E1H, 4M3H, and 4M3H are presented in figure 5.26 together with the molecular structure of these molecules. The differences from the 1-octanol spectrum show that the shape of the oxygen K-edge differs most significantly in 4M4H. The pre-edge is more pronounced, the main edge is slightly sharper and shifted to lower energies compared to 1-octanol. This is similarly observed in the difference between 2E1H and 4M3H and in the difference between 1-butanol and 2-butanol (Pylkkänen et al., 2010). This indicates less hydrogen bonding in the liquid, which might be rationalized by the fact that it the hydroxyl group is positioned in the center of the molecule. Therefore, hydrogen bonding is hindered by the alkyl chain. Calculations of XRS spectra based on molecular dynamic simulations are necessary to distinguish between inter- and intramolecular contributions to the XRS spectral shape. The beam damage increases at lower temperatures because the x-ray beam burns a hole
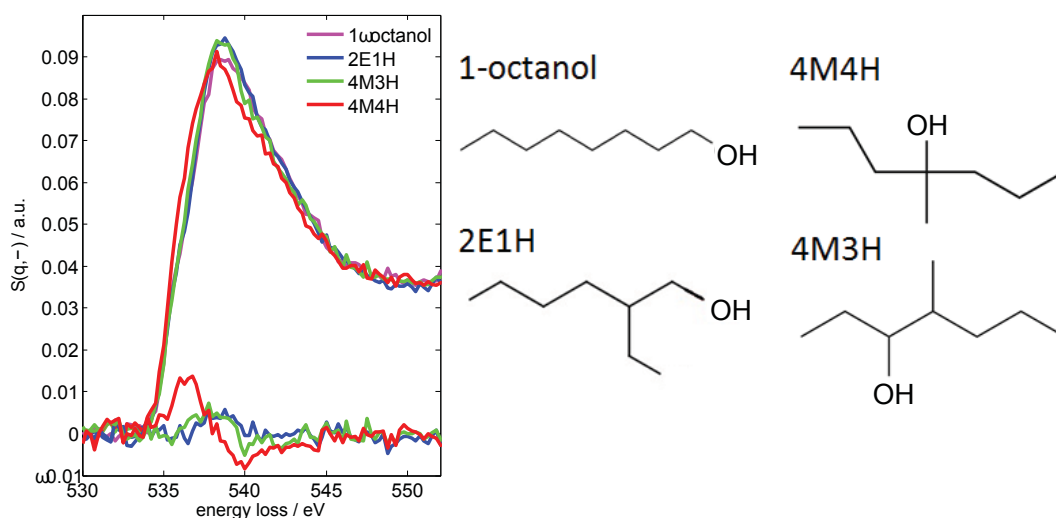


**Figure 5.26:** Oxygen K-edge of 1-octanol, 2E1H, 4M3H, 4M3H and the differences of these spectra from the 1-octanol spectrum which are displayed in the same color (left), molecular structure of 1-octanol, 2E1H, 4M3H and 4M3H (right).

into the highly viscous liquids after a short time. This limited the exposure times to 20 minutes per spectrum at temperatures lower than 273 K and therefore it was not possible to track the changes of the oxygen K-edge with a sufficient statistic at decreasing temperatures (see figure 5.27). Nevertheless, differences in the pre- and main-edge region are indicated. Therefore, it would be interesting to advance the setup to track the oxygen K-edge in these octanol isomers over a wider temperature range. Improvements to this experimental setup require some kind of flow cell (Sahle et al., 2015a) or liquid jet system to prevent beam damage effects.
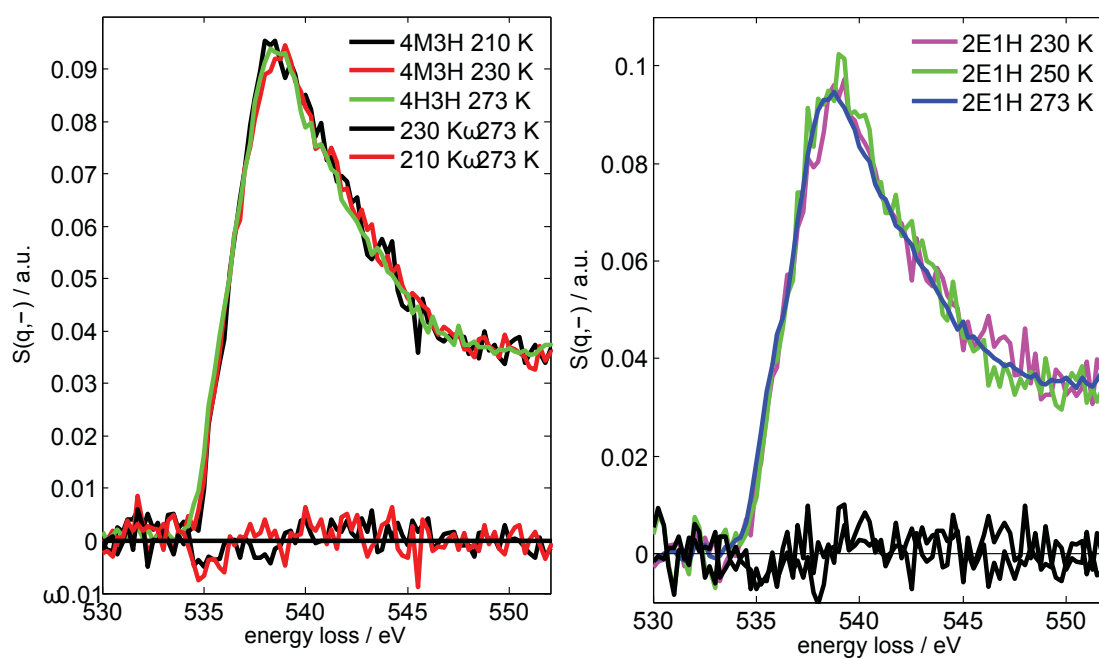
**Figure 5.27:** Oxygen K-edge of 2E1H and 4M3H at temperatures of 210 K, 230 K and 273 K and the corresponding difference curves.

# Chapter 6

# Setup for time-resolved inelastic x-ray scattering on liquids

An ultimate goal of modern science is to understand reaction dynamics on a femtosecond timescale and a sub-nanometer resolution. To this purpose, a new kind of light source has been developed that combines the advantages of modern synchrotron radiation facilities delivering hard x-rays with the advantages of laser sources which are able to generate very short pulses with a high degree of coherence. These highly coherent hard x-ray Free Electron Lasers (XFEL) have opened up a completely new field of science. Usually, time-resolved experiments on the femtosecond timescale require certain spectroscopy methods such as the pump-probe technique (Zewail, 2000). Here, a pump pulse excites a non-equilibrium state that is probed by a delayed pulse measuring the dynamic behavior of the system. The delay between the pulses can be varied to track the time evolution. The until now unrivaled brilliance and coherence of the European XFEL will allow performing e.g. laser pump, x-ray probe experiments. The FXE endstation (Bressler, 2011; Bressler et al., 2012) of the European XFEL will be dedicated to ultrafast pump-probe studies of solid and liquid samples. For this purpose, there will be several elastic and inelastic x-ray scattering probes available. Especially, experiments to determine the structure and dynamics in liquid samples are a goal of the XFEL science. Such experiments require a rethinking of how experiments can be done.

One limitation of the time resolution is the thickness of the sample since a light pulse needs a finite time to cross the sample. Therefore, a very thin sample with a thickness of a few microns is necessary to obtain femtosecond resolution. On the other hand, a thin sample is less scattering, leading to a weakly detectable signal and a smaller signal to noise ratio. One way to overcome this problem is to increase simply the power of the x-ray pulse. This leads to dramatic beam damage effects due to the high dose of radiation. While the scattering process of one femtosecond pulse is faster than the typical motion of atoms and molecules, this signal is not influenced by beam damage effects as it is detected before the sample is destroyed but for the next pulse, the sample has to be replaced. A device for replacing the sample could be a fast liquid jet. The speed that is necessary to exchange the sample fast enough can be estimated by knowing the size of

the x-ray focus on the sample and the time between two pulses. In the special case of European XFEL, the focus will be in the order of $10\,\mu$m and the pulses will be separated by $220\,$ns. Hence, a speed of $\approx 50\,$m/s will be necessary to provide a fresh sample for each x-ray pulse. In a nutshell, a device delivering a sample thickness of a few microns and a replacement of the sample as fast as possible is needed. One possibility is a liquid jet system with a very fast and thin liquid sheet from two colliding liquid jets. Such a device was purchased from *Microliquids* GmbH in Goettingen. In this chapter, a short introduction into experiments with a fast liquid *FlatJet* is given. The setup is described and the characteristics of its liquid sheet are presented. Finally, first applications are introduced. Colliding liquid jets offer the possibility to do x-ray scattering experiments without the influence of a sample container on very thin and flat targets (Ekimova et al., 2015). There are several studies on the resulting sheet shape and its spatial extension (Savart, 1833; Taylor, 1959; Lin and Lian, 1990). In technological context, colliding jets are often used to produce spray by impacting jets. The formation and fragmentation of liquid sheets from such colliding jets was investigated by N. Bremond et al. (Bremond and Villermaux, 2006).

## 6.1 Theoretical introduction

In the following, a short introduction to the theory of impacting jets is given. A good overview of the topic has been given by (Eggers and Villermaux, 2008). A complete introduction would be too extensive, so just a short discussion of the most important parameters such as speed, thickness and stability is given.

Two identical cylindrical jets form a liquid sheet because the liquid expands rapidly from the colliding point into horizontal direction. The sheet is surrounded by a liquid rim. Figure 6.1 shows a sketch of the liquid sheet and introduces the coordinate system used to describe the sheet.
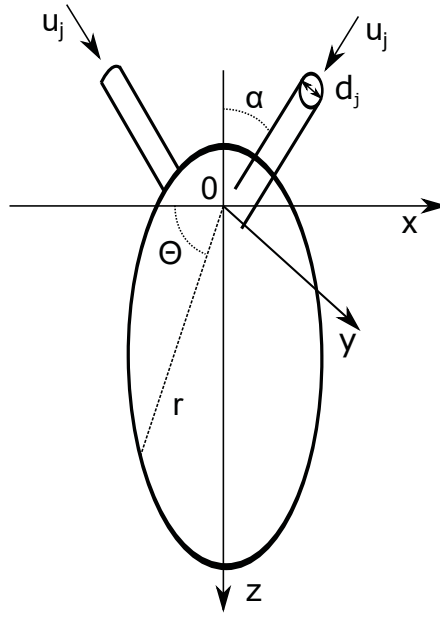


**Figure 6.1:** Coordinates employed to describe the liquid sheet.

It was found by Hasson and Peck (Hasson and Peck, 1964) that the speed of the jet $u_j$ is equal to the speed of the sheet $u$. The mean velocity is calculated from the volumetric flow rate $Q$ and the diameter of the nozzles $d_j$ by using the equation

$$u_j = \frac{1}{2} \cdot \frac{Q}{\pi(d_j/2)^2}.$$ (6.1)

The factor of 0.5 considers that the flow is split up to feed two nozzles. Typical parameters used in the following are $Q = 80\,\text{mL/min}$ and $d_j = 130\,\mu\text{m}$, leading to a mean jet velocity of $\approx 50\,\text{m/s}$. The distribution of the sheet's thickness $h$ is given by

$$h = \frac{d_j^2 \sin(\alpha)^3}{4r(1 + cos(\theta)\cos(\alpha))^2}.$$ (6.2)

In this formula, $\alpha$ is the colliding angle of the jets, $r$ the distance from the colliding point and $\theta$ the angle that $r$ encloses with the horizon. This formula shows that the thickness decreases with decreasing $r$ and $\theta$ but it is only applicable for the liquid sheet and not for the rim that surrounds the sheet which is usually thicker. The stability of a liquid sheet is given by its Weber number which is a dimensionless number in fluid mechanics and measures the relative importance of the fluid's interia compared to its surface tension. It is defined as

$$W_{\mathrm{e}} = \frac{\rho d_j u^2}{\sigma} \tag{6.3}$$

with $\sigma$ the surface tension and $\rho$ the density of the liquid. The surface tension for water is $\sigma = 0.072 \, \mathrm{kg \, s^{-2}}$ at $T = 293 \, \mathrm{K}$. The Weber number for the parameters introduced before is $W_{\mathrm{e}} = 4513$, which is in principle too high to form a smooth sheet (Bush and Hasha, 2004; Li and Ashgriz, 2006). Nevertheless, a smooth sheet is formed as will be shown later which might be due to a flat angle collision angle. The Weber number is important to consider if different liquids are used. In other words, the stability of the liquid sheet depends on the surface tension which can be compensated by the speed of the jet or the diameter of the nozzles. The Reynolds number of the jet is given by

$$R_{\mathrm{e}} = u_j d_j / \nu \tag{6.4}$$

in which $\nu$ is the dynamic viscosity of the liquid, for example $\nu = 10^{-6} \mathrm{m^2 s^{-1}}$ in water. It is defined as the ratio of inertial forces to viscous forces and is used in fluid dynamics to determine dynamic similitude between laminar and turbulent flow. Laminar flow occurs at low $R_{\mathrm{e}}$, where viscous forces are dominant and turbulent flow occurs at high $R_{\mathrm{e}}$, where inertial forces produce chaotic instabilities. The fast jet is characterized by a Reynolds number of $R_{\mathrm{e}} \approx 6500$. If the Reynolds number is too high, the initial jets get disturbed and naturally no stable sheet can be formed. Compared to the literature this value allows a stable cylindrical jet in vacuum (Otendal et al., 2005). Since the Reynolds number depends on the dynamic viscosity of the sample liquid, the nozzle diameter or the jet speed has to be adjusted if a sample with a different viscosity is used.

## 6.2 Setup of a *Microliquid FlatJet* system

In this section, a *Microliquid FlatJet* is described which is supposed to be set up at the FXE endstation of the XFEL in Hamburg (Bressler, 2011; Bressler et al., 2012). Figure 6.2 a) shows a picture of the upper part of the *FlatJet* system. It consists of a 3-axis manipulator flange on which the *FlatJet* unit is mounted. The *FlatJet* can be moved along this three axes for 2 cm in each direction with micrometer precision, which is necessary to place the liquid sheet in the overlap region of pump laser and probe XFEL pulse. The liquid for the sheet is delivered by a high-pressure capillary from a *Shimadzu LC-20AP* piston pump with a maximum pressure of 300 bar, but a pressure higher than 150 bar is not feasible because of the layout of the high-pressure connections. The liquid is split into two different capillaries to feed both of the two quartz nozzles. The breakup

can be tuned with two outlets. After passing the outlets the capillaries get cooled or heated by a chiller that can be connected via two 4 mm tube connections. The chiller and the materials for liquid transport allow a temperature range from $-30-100\,°$C. A picture of the nozzle holder is presented in figure 6.2 b). It is made of Polyether ether ketone (PEEK) which has excellent mechanical and chemical resistance properties and holds the nozzles at a fixed angle of $2\alpha = 20\,°$. It is quite challenging to mount the nozzles so that the installation should be conducted under the supervision of experts from *Microliquids GmbH* at the first time. One of the nozzles is mounted on an adjustable stage to correct the horizontal and vertical position in order to align the colliding point. This is necessary because of inaccuracies during manufacture of the nozzles that lead to slightly different lengths and shapes. To produce a smoothly flat liquid sheet, the nozzles need to be positioned as close as possible to each other and perfectly adverse. This can be done by moving one of the nozzles employing a piezo motor until a well-defined leaf is observed. Additionally, it is important to adjust the flow of the nozzles in a way that the flow from both nozzles is the same. To check if the correct position is found, there is a microscope camera monitoring the liquid leaf during the experiment. The complete setup of the *Microliquid FlatJet* system is pictured in Figure 6.2 c). It consists of the jet generating system, a catcher unit collecting the liquid of the sheet and delivering it to a dump or back to the reservoir of the pump, the pump itself and a pulsation damper which will be described later. If the recycling option is used, a minimum of 10 m/L sample liquid is required to fill the whole liquid circle. The *FlatJet* is usually covered by a tubing and a cross-chamber with six openings holding the jet and the catcher unit. A different mount would also be possible if it fits the experimental conditions in a better way. The tubing and the cross-chamber cannot be evacuated but flushed with dry nitrogen gas. The *FlatJet* can be equipped with four different sets of quartz nozzles with different diameters ($d_\mathrm{j} = 100\,\mu$m, $130\,\mu$m, $400\,\mu$m, $500\,\mu$m) allowing experiments both, at liquid sheets and at cylindrical jets of a single nozzle with steadily refreshed liquid solutions. To generate a smoothly flat liquid sheet, it is necessary that the nozzles are perfectly clean which can be reached by employing an ultrasonic bath and flushing with dust free isopropanol or ethanol. An inline filter is used to prevent congestion of the nozzles by small particles during the experiment. This filter should be changed after each experiment. Right before the experiment, the whole system should be flushed with the sample liquid to avoid contamination. Referring to the specification sheet, the demand on the *FlatJet* is to deliver a liquid sheet with a speed of $25-50$ m/s and a thickness of $5-20\,\mu$m. This will be checked in the following.
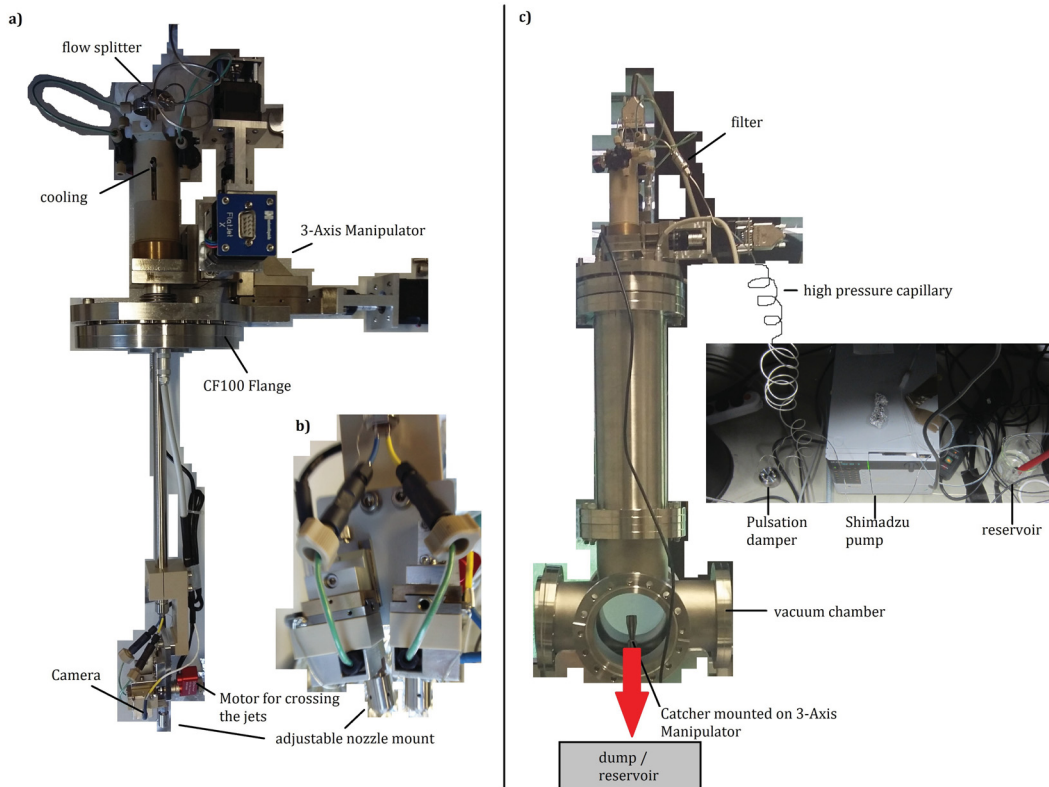
**Figure 6.2:** Picture taken of the *Micorliquids FlatJet* system (a), a closeup view of the nozzle holder (b), the *FlatJet* in its containment and the *Shimadzu* pump arranged like employed in an experiment (c).

## 6.3 Characterisation of a liquid sheet

In the following chapter, a setup for the characterization of the liquid sheet is described. The main aim was to measure the thickness and the position of the sheet with high precision. This is necessary because the thickness limits the possible time resolution and the position has to be stable to realize the correct scattering geometry. The ultimate goal is an online characterization of the jet during an experiment. For this purpose, the liquid jet system was set up at a laser laboratory at DESY in Hamburg where a *Polytec TopSense* device is available. The *TopSense* device is employing the Chromatic Confocal Sensing (CCS) which was invented by *STIL* (STIL, 1995) and is an accurate and reliable technique for distance and thickness measurements. Therefore, a white light is imaged through a chromatic objective on the surface but only one wavelength is perfectly focused. The backscattered light passes a pinhole and is detected by a spectrometer where the specific wavelength is calculated to determine the position of the surface. In the case of a transparent object, there are two images, one reflected

from the front and one from the back of the sheet. The distance is calculated for both surfaces and its difference is the thickness of the sample. The main advantage of this technique is that thickness and distance measurements are possible at the same time without any contact or other disturbances. Also, the spot is small and easily visible which allows measuring the sheet at different well-defined positions. The *TopSense* has to be positioned at a distance of 2.7 mm and is able to measure the thickness in a range from $3-100\,\mu$m and distance variations from $30-100\,\mu$m behind the working point. Therefore it was mounted on a translation stage to move it carefully to the correct position. To control the position of the light spot on the liquid sheet a microscope and a bright LED was mounted on the opposite of the *TopSense*. A picture of the setting is presented in Figure 6.3 as well as a picture of the liquid sheet.
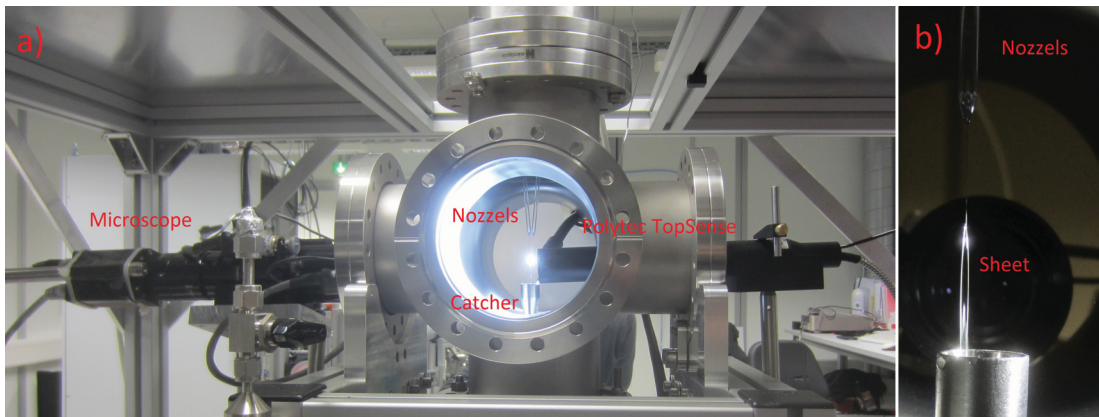


**Figure 6.3:** Liquid *FlatJet* setup at XFEL laser laboratory at DESY in Hamburg. The *Polytech TopSense* device is used to measure the thickness and position of the sheet and the microscope is used to control the position.

Figure 6.4 shows a closeup view of the liquid jet taken with the microscope and the white light spot of the *TopSense*. The diameter of the *TopSense* is 27 mm which allows to calibrate the axes. First, the variation of the thickness in the horizontal direction (x-axis) was measured while the vertical coordinate was kept constant (z-axis). This was done for different distances and at different flow rates of the jet. The jet was moved horizontally by employing its translation stage. Because the horizontal axis is not perfectly perpendicular to the axis of the *TopSense* (y-axis) it had to be moved as well to be positioned at the working point of the *TopSense*. The results are presented in figure 6.5. There are two different kinds of profiles depending on the $z$-position on the sheet. The thickness measured on top of the leaf at $z = 5, 6, 11$ mm are larger in the center than at the edges like formula 6.2 predicts. At the center of the leaf ($z = 18$ mm) the bend is in the opposite direction and less pronounced which can be explained by the rim of the sheet. The center of the sheet at a flow of 80 mL/min is thinner than measurable but there is still liquid which was tested by pulling a thin wire
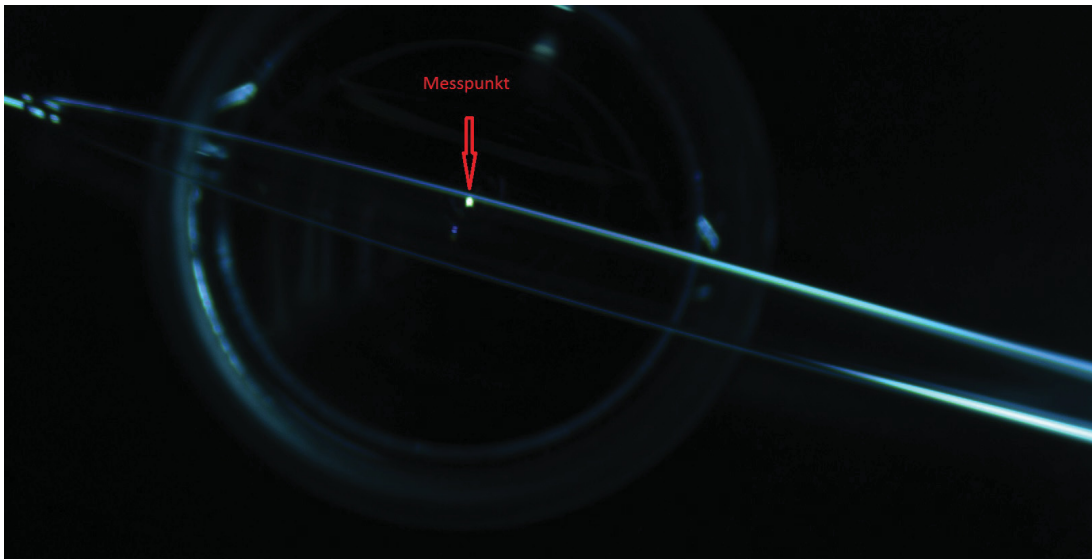
**Figure 6.4:** Sheet generated by the Liquid Flat Jet system in front of a *Polytec TopSense*. The white spot is the white light spot of the polychromatic measuring tool.

into the sheet. Compared to the measurement at the same position but with a flow of 60 mL/min one notices that the sheet gets thinner if the flow rate is increased. A higher flow rate increases the speed of the jet, such a dependence was not considered in formula 6.2. Due to the limitations of the *TopSense*, it was not possible to measure at flow rates higher than 80 mL/min. Afterward, the thickness of the leaf was measured at the center of the sheet but at different vertical positions. Figure 6.6 shows that the leaf got thinner if the distance to the colliding point increases, as predicted by formula 6.2. The decay of the thickness is quite linear and could be observed at three different flow rates. Theoretical observations predict that the leaf closes at the bottom which could not be verified by measurements because the bottom of the leaf was covered by the catcher but the picture of the leaf confirms its theoretical shape.

Since a piston pump is used, its pulsation is transferred to the *FlatJet*. This hinders the formation of a smooth sheet and is obviously not desirable in an x-ray scattering experiment. The *Microliquids* pulsation damper settles the beating of the piston pump employing the Windkessel effect that describes the damping of the fluctuation in blood pressure by an elastic reservoir realized by elastic arteries in the human body (Sagawa et al., 1990). This effect was also used in fire engines in the 18th century. The fire fighting water was pumped against a reservoir filled with air, which is quite similar to the *Microliquid* solution that uses a gas volume of 3 mL which is coupled by a membrane to the pumped liquid (see figure 6.7). The advantage of such a system is that it is small and easy to handle. It just has to be built in the liquid circle behind the pump and in front of the liquid Jet. In order to increase the stability, the capillary is passed to a
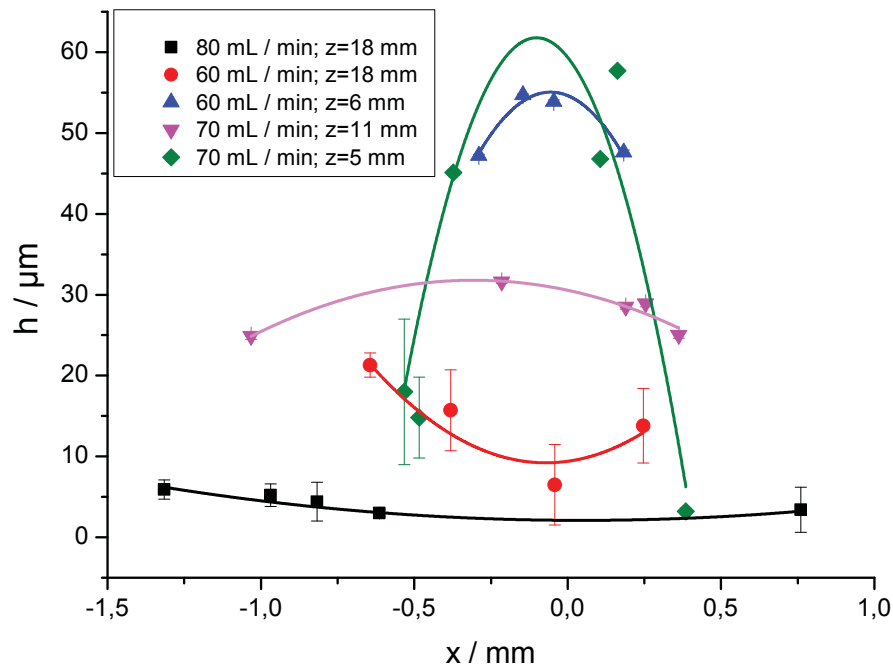
**Figure 6.5:** Thickness profile of the liquid sheet in horizontal direction at different heights and flow rates.

400 g massive block of steel. Furthermore, it is important that the pump and the jet are decoupled, i.e. the pump should be placed on a different table than the *FlatJet*. The best results were achieved when the pump was placed on the ground around one meter away from the *FlatJet*. A disadvantage of the Windkessel is that it works best at a flow of 80 mL/min. To illustrate that effect, a measurement with increasing flow rate was done at the same spot of the leaf. Figure 6.7 shows the distance deviation of the liquid sheet in dependence of the flow rate, which is a good marker for the stability. There is a trend to less distance deviation when the flow approaches 80 mL/min but it was not possible to further increase the flow because the sheet got too thin to be measured. The effect of the pulsation damper is also presented in figure 6.8. The distance was measured with a read out frequency of 100 Hz for 10 seconds at a flow of 60 mL/min without the pulsation damper. Afterward, the pulsation damper was installed and the measurement was repeated. The absolute position changed for $\approx 20\,\mu$m during the installation of the damper. The reason for this remained unclear, which underlines the necessity for online control of the position during an experiment. Nevertheless, a significant reduction of the pulsation could be obtained. As presented in figure 6.8 the distance deviation could be reduced from $0.93\,\mu$m to $0.52\,\mu$m. At a flow of 80 mL/min the effect should be even better but the jet was too thin to allow any measurements. It is also important to mention that this was just one measurement at a distinct position on the liquid sheet. In general, the pulsation could be reduced which is even visible to the naked eye but the exact values for the stability have to be checked for each measurement because it
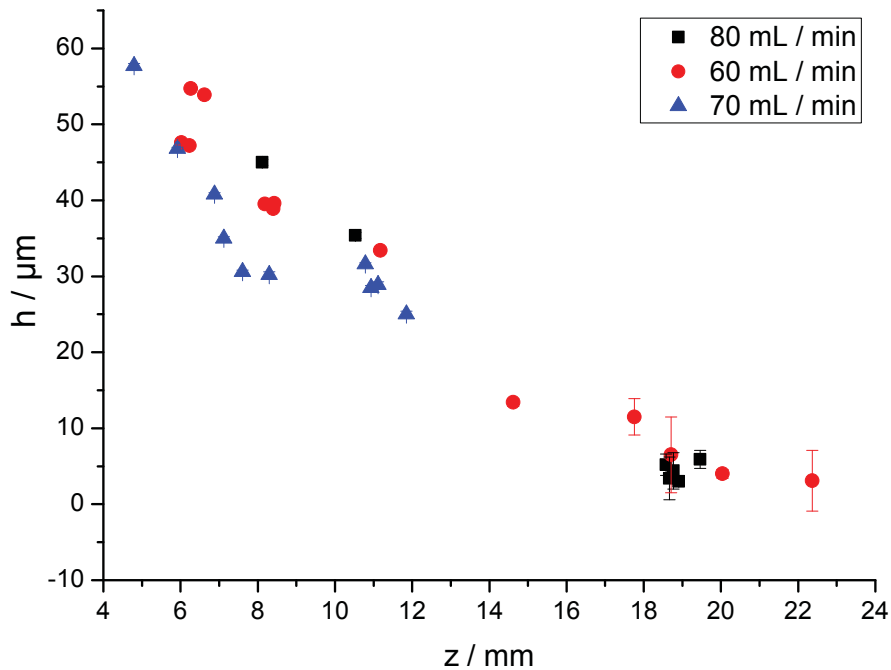
**Figure 6.6:** The thickness of the sheet in the vertical direction and at three different flow rates.

strongly depends on the viscosity of the liquid, the temperature and the position of the nozzles. Therefore, the *TopSense* and the microscope should be mounted to a permanent translation stage in the future in order to be able to repeat the characterization before an experiment is done. It might be helpful to have different pulsation dampers available in order not to be limited in the flow rate. A different solution would be a pulsation damper with adjustable gas pressure. Such a device is already available for this system. Furthermore, a way to measure the thickness of a very thin sheet has to be figured out. However, the *Microliquids FlatJet* is a device that delivers a smooth sheet at a speed of $50\,\mathrm{ms/s}$ and a thickness of $5 - 20\,\mu\mathrm{m}$ can easily be realized. The device was transferred to Hamburg where it will be part of experiments at the FXE endstation in the future.
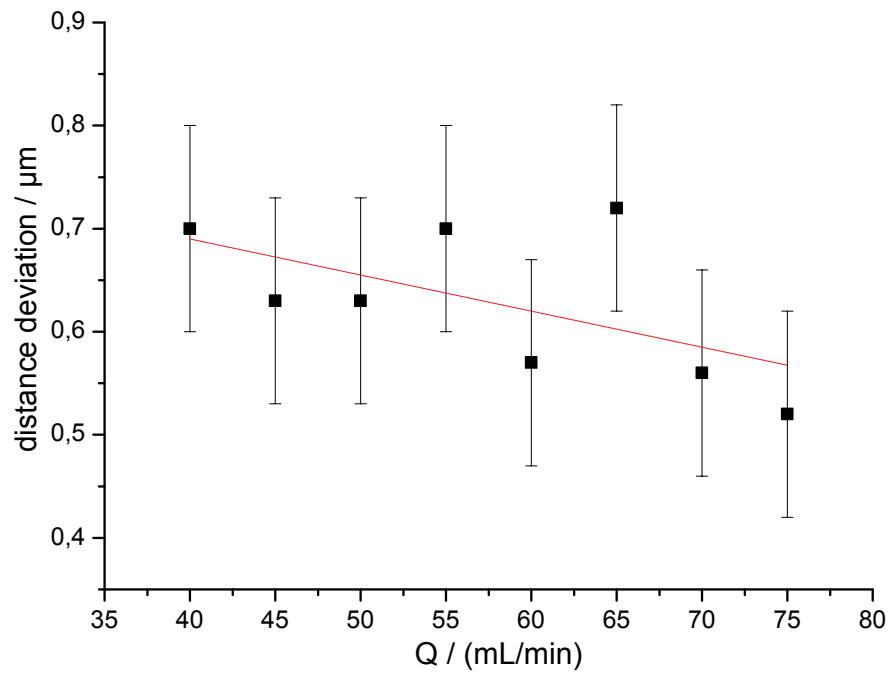
**Figure 6.7:** Distance deviation in dependence of the liquid flow in the range from $Q = 40 - 75 \, \text{mL/min}$ by employing the *Microliquid* pulsation damper.
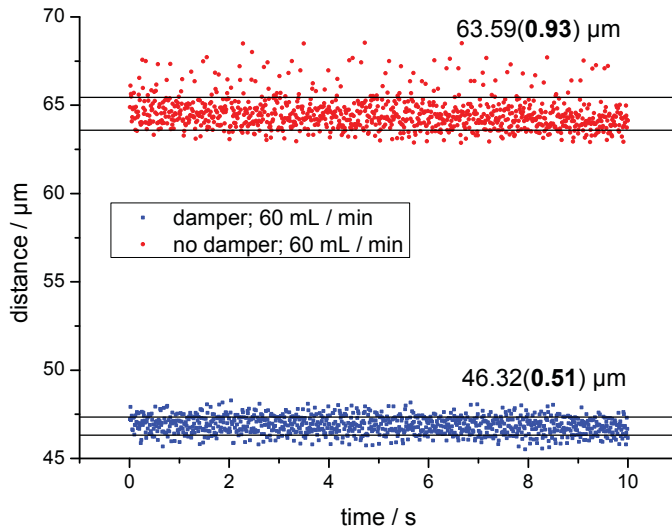
**Figure 6.8:** Example of the time evolution of the distance deviation at a constant flow of $Q = 60\,\text{mL/min}$ with and without pulsation damper.

## 6.4 Combination of liquid jet and von Hamos spectrometer at P01 at PETRA III

PETRA III is a synchrotron with an extent of 2.3 kilometers located in Hamburg, Germany. It runs with a beam current of 100 mA at an energy of 6 GeV. PETRA III is the most brilliant synchrotron of the world. The experimental setup for inelastic x-ray scattering at beamline P01 allows doing XRS. The beamline setup includes a Si(311) monochromator. The flux on the sample is $5 \cdot 10^{12}$ photons per second at a beam size of $180x190\,\mu\text{m}$. The scattered photons were focused by 12 analyzer crystals on four point detectors (avalanche photodiode, three analyzers per diode). All the crystals are located in one array on a 1 m Rowland circle and the scattering angle was chosen to be 30° in forward scattering leading to a low-$q$ energy transfer. The elastic line of the analyzer crystals was located at 9693 eV and was scanned before each scan of the oxygen K-edge. The overall energy resolution was $\Delta E > 1\,\text{eV}$. The energy transfer was scanned from 520 eV to 532 eV in steps of 0.2 eV with 3 seconds per point, in the range from 532 eV to 540 eV with a step size of 0.16 with 8 seconds and from 540 eV to 555 eV with a step size of 0.23 eV and 6 seconds per data point. At the same time, a dispersive von Hamos spectrometer (Alonso-Mori et al., 2012) was set up at an angle of $\approx 130°$. This device allows measuring XRS spectra at fixed incident energy. The scattered x-rays are focused in one direction by cylindrical bend analyzer crystals. In the other direction the scattering angle depends on the wavelength. Therefore, each analyzer crystal acts like

a prism for visible light. A sketch of the scattering geometry is presented in figure 6.10. The spectrometer was equipped with eight crystals focusing the x-rays on a Pilatus 100K detector. The crystals were positioned on a 50 cm Rowland circle. The Si(440) reflex of the analyzer crystals was used to measure the oxygen K-edge of water. The distance between sample and Pilatus detector was $\approx 50$ cm because of the Bragg angle of the analyzer crystals of $\approx 63°$ at an incident energy of 7 keV. A picture of the whole setup is presented in figure 6.9. The spectrum gained by the von Hamos spectrometer was of bad quality. This can be improved in further experiments if the von Hamos spectrometer and the detector are getting shielded and mounted on adjustable stages to find the best focusing position. Moreover, the signal to noise ratio can be improved if the x-ray path gets evacuated or flushed by helium to decrease the air scattering and by overlapping the signal of all analyzer crystals on the detector. An improved experiment was performed by Manuel Harder. After optimizing the von Hamos setup, the scattering angle was $90°$, eight Si(111) analyzer crystals were overlapped and the sample was exposed to the x-rays with an energy of 7590 eV for 390 minutes. The energy resolution of this setup was $> 1.5$ eV. The resulting oxygen K-edge is presented in figure 6.10 and compared to the data measured with the usual XRS setup.

The slight differences are due to the different wave vector transfer. Apart from that, both curves are in good agreement. It can be concluded, that in future this setup will allow doing time resolved inelastic scattering experiments on liquid samples.
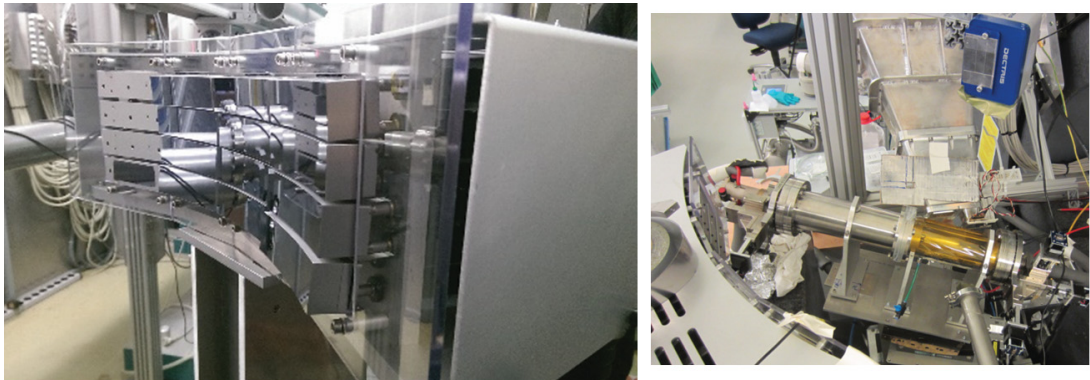


**Figure 6.9:** Picture of the von Hamos spectrometer equipped with eight spherical bend analyzer crystals (left). Picture of the whole setup at P01 at DESY including the von Hamos spectrometer, the *FlatJet* and the XRS setup (right).
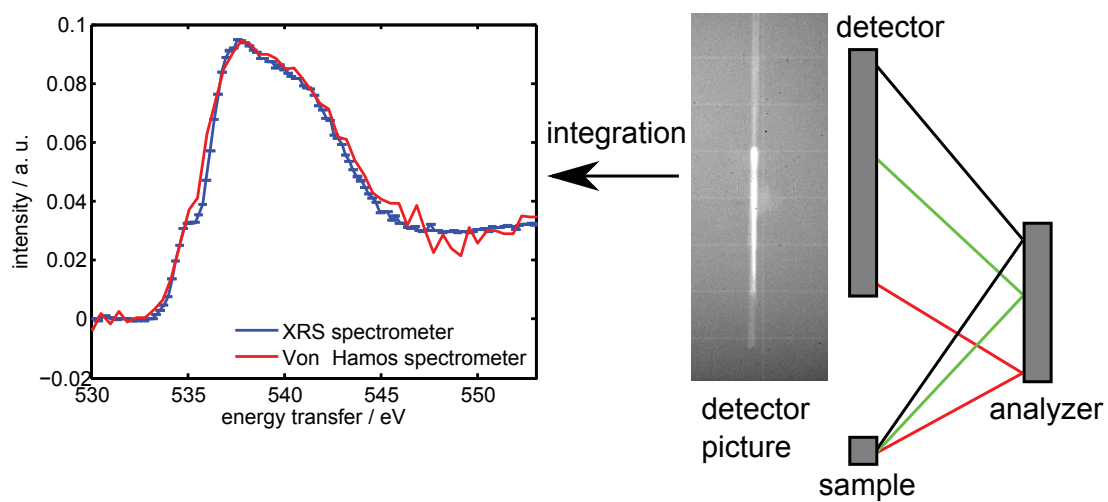
**Figure 6.10:** Oxygen K-edge of water measured with the Von Hamos spectrometer, provided by Manuel Harder, and the usual XRS setup and a sketch of the experimental setup including a detector picture.

# Chapter 7

# Summary and outlook

In this thesis, the formation and disturbance of supramolecular structures in MAs, mixtures of MAs, and mixtures of MAs and halogen alkanes were investigated by x-ray diffraction. Furthermore, x-ray Raman scattering was applied to several octanol isomers and a setup for time-resolved inelastic x-ray scattering on liquids was commissioned and tested.

The disintegration of supramolecular structures in 2E1H by mixing with the halogen alkanes 2E1Cl and 2E1Br was monitored via the prepeak of the static structure factor. It was found that the supramolecular arrangements get disturbed rapidly until a critical concentration beyond H-bonded structuring is suppressed efficiently. Moreover, the surprisingly strong enhancement of dielectric absorption in mixtures of ring building MAs was investigated by XRD systematically and clear structural evidence for a ring to chain transformation was found. This knowledge about the fingerprint on structuring in the medium range structure factor was applied to get insights into hydrogen bonding at high hydrostatic pressure and to explain the oppositional behavior of the Debye process in 2E1H and 4M3H at a molecular level. It turned out that pressure disintegrates supramolecular structures in both alcohols and the resulting fragments are more alike at high pressures. In particular, the chain-like structures in 2E1H get shortened and the ring-like structures are transformed into chain like ring fragments. As a next step, it is planned to perform x-ray diffraction measurements at pressures in the range of $10 - 20$ kbar employing diamond anvil cells. Furthermore, the temperature dependence of the static structure factor of 2E1H and 4M3H was investigated over a wide range of temperature and wave vector transfer at ambient pressure. The study showed clear evidence for different properties of H-bonded clusters at temperatures beyond $\approx 250$ K exhibiting different thermal expansion and local structuring constrained by the alkyl chains, and a disturbance of supramolecular structures at high temperatures leading to an increased amount of monomers. Since the measurements were performed over a wide range of wave vector transfer, it was possible to obtain the PDFs of both alcohols over a wide range of temperature for the first time and therefore to get valuable information about the short range order in these liquids, which might be the basis of further investigations employing molecular dynamic simulations to gain detailed insights into

the short range order of hydrogen bonding in these systems.

Moreover, the first XRS spectra of isomers of octanols, e.g. 2E1H, 4M3H, and 4M4H, which exhibit different dielectric absorption properties are presented. These spectra lead to the conclusion that the amount of hydrogen bonding is dependent on the symmetry of the molecules. In 4M4H the hydroxyl group is shielded the most efficiently, which leads to significantly less hydrogen bonding. However, small but distinct differences between 2E1H and 4M3H do also support the concept of different supramolecular arrangements. This also motivates to conduct molecular dynamic simulations, complementing x-ray diffraction and x-ray Raman scattering, in order to find a model that explains the structure formation on a molecular level.

The investigation of the formation and disturbance of H-bonds on a femtosecond timescale would be of high relevance. Such experiments will become possible in the near future because of the rapid development of free electron lasers in the x-ray region. This asks for a new concept of how experiments can be done. Especially, the sample injection is an issue. To this purpose, a fast liquid *FlatJet* system was purchased from *Microliquids* GmbH, successfully commissioned, tested and transferred to DESY. This system, in combination with a dispersive von Hamos spectrometer, will allow performing time-resolved inelastic x-ray scattering experiments at the new European XFEL. This may have relevance for many disciplines of science such as physics, chemistry and biology and probably new industrial applications.

# Bibliography

Abdel Hamid, A. R., Mhanna, R., Lefort, R., Ghoufi, A., Alba-Simionesco, C., Frick, B., and Morineau, D. (2016). Microphase separation of binary liquids confined in cylindrical pores. *The Journal of Physical Chemistry C*, 120(17):9245–9252.

Akiyama, I., Ogawa, M., Takase, K., Takamuku, T., Yamaguchi, T., and Ohtori, N. (2004). Liquid structure of 1-propanol by molecular dynamics simulations and x-ray scattering. *Journal of Solution Chemistry*, 33(6-7):797–809.

Alonso-Mori, R., Kern, J., Sokaras, D., Weng, T.-C., Nordlund, D., Tran, R., Montanez, P., Delor, J., Yachandra, V. K., Yano, J., et al. (2012). A multi-crystal wavelength dispersive x-ray spectrometer. *Review of Scientific Instruments*, 83(7):073114.

Als-Nielsen, J. and McMorrow, D. (2011). *Elements of Modern X-ray Physics*. John Wiley & Sons.

Amann-Winkel, K., Böhmer, R., Fujara, F., Gainaru, C., Geil, B., and Loerting, T. (2016). Colloquium: Water's controversial glass transitions. *Reviews of Modern Physics*, 88(1):011002.

Anton-Paar (2014). Dsa 5000 m, bedienunsanleitung. `http://http://www.anton-paar.com/de-de/produkte/details/dichte-und-schallgeschwindigkeitsmessgeraet-dsa-5000-m/`.

Arunan, E., Desiraju, G. R., Klein, R. A., Sadlej, J., Scheiner, S., Alkorta, I., Clary, D. C., Crabtree, R. H., Dannenberg, J. J., Hobza, P., et al. (2011). Definition of the hydrogen bond (iupac recommendations 2011). *Pure and Applied Chemistry*, 83(8):1637–1641.

Bauer, S., Wittkamp, H., Schildmann, S., Frey, M., Hiller, W., Hecksher, T., Olsen, N., Gainaru, C., and Böhmer, R. (2013). Broadband dynamics in neat 4-methyl-3-heptanol and in mixtures with 2-ethyl-1-hexanol. *The Journal of Chemical Physics*, 139(13):134503.

Bellissent-Funel, M.-C., Nasr, S., and Bosio, L. (1997). X-ray and neutron scattering studies of the temperature and pressure dependence of the structure of liquid formamide. *The Journal of Chemical Physics*, 106(19):7913–7919.

Benmore, C. (2012). A review of high-energy x-ray diffraction from glasses and liquids. *ISRN Materials Science*, 2012.

Benmore, C. J. and Loh, Y. L. (2000). The structure of liquid ethanol: a neutron diffraction and molecular dynamics study. *The Journal of Chemical Physics*, 112(13):5877–5883.

Berghaus, M., Paulus, M., Salmen, P., Al-Ayoubi, S., Tolan, M., and Winter, R. (2016). Near-surface and bulk behavior of bicontinuous microemulsions under high-pressure conditions. *The Journal of Physical Chemistry B*, 120(29):7148–7153.

Bierwirth, S., Büning, T., Gainaru, C., Sternemann, C., Tolan, M., and Böhmer, R. (2014). Supramolecular x-ray signature of susceptibility amplification in hydrogen-bonded liquids. *Physical Review E*, 90(5):052807.

Böhmer, R., Gainaru, C., and Richert, R. (2014). Structure and dynamics of monohydroxy alcohols—milestones towards their microscopic understanding, 100 years after debye. *Physics Reports*, 545(4):125–195.

Böttcher, C. J. F. (1973). Theory of electric polarization, 2nd ed. 1(40).

Bradley, J., Moore, K., van der Laan, G., Bradley, J., and Gordon, R. (2011). Core and shallow-core d-to f-shell excitations in rare-earth metals. *Physical Review B*, 84(20):205105.

Bragg, W. H. and Bragg, W. L. (1913). The reflection of x-rays by crystals. *Proceedings of the Royal Society of London. Series A, Containing Papers of a Mathematical and Physical Character*, 88(605):428–438.

Bremond, N. and Villermaux, E. (2006). Atomization by jet impact. *Journal of Fluid Mechanics*, 549:273–306.

Bressler, C. (2011). Scientific instrument fxe. *CDR*.

Bressler, C., Galler, A., and Gawelda, W. (2012). Technical design report: Scientific instrument fxe. *XFEL. EU TR-2012-008*.

Brot, C. (1989). Hydrogen bonded clusters of alcohol molecules in inert solvents: a chain statistics approach. *Zeitschrift für Physik D Atoms, Molecules and Clusters*, 11(3):249–255.

Bush, J. W. and Hasha, A. E. (2004). On the collision of laminar jets: fluid chains and fishbones. *Journal of Fluid Mechanics*, 511:285–310.

Cai, Y., Mao, H.-K., Chow, P., Tse, J., Ma, Y., Patchkovskii, S., Shu, J., Struzhkin, V., Hemley, R., Ishii, H., et al. (2005). Ordering of hydrogen bonds in high-pressure low-temperature h 2 o. *Physical Review Letters*, 94(2):025502.

ChemicalBook (2016). chemicalbook.com. `http://www.chemicalbook.com/`.

Choi, K. H. and Morais, M. (2014). Use of small-angle x-ray scattering to investigate the structure and function of dengue virus ns3 and ns5. *Dengue: Methods and Protocols*, pages 241–252.

Cri (2012). *Rdf schematic*. Wikimedia Commons, Creative Commons Attribution-Share Alike 3.0 Unported.

Dannhauser, W. (1968a). Dielectric relaxation in isomeric octyl alcohols. *The Journal of Chemical Physics*, 48(5):1918–1923.

Dannhauser, W. (1968b). Dielectric study of intermolecular association in isomeric octyl alcohols. *The Journal of Chemical Physics*, 48(5):1911–1917.

Debye, P. and Scherrer, P. (1916). Interferenzen an regellos orientierten teilchen im röntgenlicht. i. *Nachrichten von der Gesellschaft der Wissenschaften zu Göttingen, Mathematisch-Physikalische Klasse*, 1916:1–15.

Debye, P. J. W. (1929). *Polar molecules*. Chemical Catalog Company, Incorporated.

Dymond, J. and Malhotra, R. (1988). The tait equation: 100 years on. *International Journal of Thermophysics*, 9(6):941–951.

Eggers, J. and Villermaux, E. (2008). Physics of liquid jets. *Reports on Progress in Physics*, 71(3):036601.

Ekimova, M., Quevedo, W., Faubel, M., Wernet, P., and Nibbering, E. T. (2015). A liquid flatjet system for solution phase soft-x-ray spectroscopy. *Structural Dynamics*, 2(5):054301.

Elliott, S. R. (1991). Medium-range structural order in covalent amorphous solids. *Nature*, 354:445–452.

Franks, F. (1972). Water: a comprehensive treatise. volume 1. the physics and physical chemistry of water.

Franks, N., Abraham, M., and Lieb, W. (1993). Molecular organization of liquid n-octanol: An x-ray diffraction analysis. *Journal of Pharmaceutical Sciences*, 82(5):466–470.

Fukasawa, T. and Sato, T. (2011). Versatile application of indirect fourier transformation to structure factor analysis: from x-ray diffraction of molecular liquids to small angle scattering of protein solutions. *Physical Chemistry Chemical Physics*, 13(8):3187–3196.

Gainaru, C., Kastner, S., Mayr, F., Lunkenheimer, P., Schildmann, S., Weber, H., Hiller, W., Loidl, A., and Böhmer, R. (2011). Hydrogen-bond equilibria and lifetimes in a monohydroxy alcohol. *Physical Review Letters*, 107(11):118304.

Gainaru, C., Meier, R., Schildmann, S., Lederle, C., Hiller, W., Rössler, E., and Böhmer, R. (2010). Nuclear-magnetic-resonance measurements reveal the origin of the debye process in monohydroxy alcohols. *Physical Review Letters*, 105(25):258303.

Gómez-Álvarez, P., Romaní, L., and González-Salgado, D. (2013). Association effects in pure methanol via monte carlo simulations. i. structure. *The Journal of Chemical Physics*, 138(4):044509.

Gong, H., Chen, Z., Bi, D., Sun, M., Tian, Y., and Wang, L.-M. (2012). Unusual dielectric strength of debye relaxation in monohydroxy alcohols upon mixing. *The Journal of Physical Chemistry B*, 116(37):11482–11487.

Hämäläinen, K. and Manninen, S. (2001). Resonant and non-resonant inelastic x-ray scattering. *Journal of Physics: Condensed Matter*, 13(34):7539.

Hammersley, A., Svensson, S., Hanfland, M., Fitch, A., and Hausermann, D. (1996). Two-dimensional detector software: from real detector to idealised image or two-theta scan. *International Journal of High Pressure Research*, 14(4-6):235–248.

Hansen, J. S., Kisliuk, A., Sokolov, A. P., and Gainaru, C. (2016). Identification of structural relaxation in the dielectric response of water. *Physical Review Letters*, 116(23):237601.

Hasson, D. and Peck, R. E. (1964). Thickness distribution in a sheet formed by imping-ing jets. *AIChE Journal*, 10(5):752–754.

Hédoux, A., Guinet, Y., Paccou, L., Derollez, P., and Danède, F. (2013). Vibrational and structural properties of amorphous n-butanol: A complementary raman spectroscopy and x-ray diffraction study. *The Journal of Chemical Physics*, 138(21):214506.

Henke, B. L., Gullikson, E. M., and Davis, J. C. (1993). X-ray interactions: photoab-sorption, scattering, transmission, and reflection at e= 50-30,000 ev, z= 1-92. *Atomic Data and Nuclear Data Tables*, 54(2):181–342.

Huotari, S., Pylkkänen, T., Verbeni, R., Monaco, G., and Hämäläinen, K. (2011). Direct tomography with chemical-bond contrast. *Nature Materials*, 10(7):489–493.

Jü (2013). *MethanolHydrogenBridge*. Wikimedia Commons, Creative Commons license.

Juurinen, I., Pylkkänen, T., Sahle, C. J., Simonelli, L., Hämäläinen, K., Huotari, S., and Hakala, M. (2014). Effect of the hydrophobic alcohol chain length on the hydrogen-bond network of water. *The Journal of Physical Chemistry B*, 118(29):8750–8755.

Kashyap, H. K., Santos, C. S., Annapureddy, H. V., Murthy, N. S., Margulis, C. J., and Castner Jr, E. W. (2012). Temperature-dependent structure of ionic liquids: X-ray scattering and simulations. *Faraday Discussions*, 154:133–143.

Kieffer, J. and Karkoulis, D. (2013). Pyfai, a versatile library for azimuthal regrouping. In *Journal of Physics: Conference Series*, volume 425, page 202012. IOP Publishing.

Kramers, H. A. and Heisenberg, W. (1925). Über die streuung von strahlung durch atome. *Zeitschrift für Physik A Hadrons and Nuclei*, 31(1):681–708.

Kratky, O. (1982). A survey. In *Small angle X-ray scattering*.

Krywka, C. (2008). *Ein Aufbau für Röntgenkleinwinkelstreuung an Protein-Lösungen an der Synchrotronstrahlungsquelle DELTA*. PhD thesis.

Krywka, C., Sternemann, C., Paulus, M., Javid, N., Winter, R., Al-Sawalmih, A., Yi, S., Raabe, D., and Tolan, M. (2007). The small-angle and wide-angle x-ray scattering set-up at beamline bl9 of delta. *Journal of Synchrotron Radiation*, 14(3):244–251.

Krywka, C., Sternemann, C., Paulus, M., Tolan, M., Royer, C., and Winter, R. (2008). Effect of osmolytes on pressure-induced unfolding of proteins: A high-pressure saxs study. *ChemPhysChem*, 9(18):2809–2815.

Kunnus, K., Rajkovic, I., Schreck, S., Quevedo, W., Eckert, S., Beye, M., Suljoti, E., Weniger, C., Kalus, C., Grübel, S., et al. (2012). A setup for resonant inelastic soft x-ray scattering on liquids at free electron laser light sources. *Review of Scientific Instruments*, 83(12):123109.

Lehmkühler, F., Forov, Y., Büning, T., Sahle, C. J., Steinke, I., Julius, K., Buslaps, T., Tolan, M., Hakala, M., and Sternemann, C. (2016). Intramolecular structure and energetics in supercooled water down to 255 k. *Physical Chemistry Chemical Physics*, 18(9):6925–6930.

Lehtola, J., Hakala, M., and Hamalainen, K. (2010). Structure of liquid linear alcohols. *The Journal of Physical Chemistry B*, 114(19):6426–6436.

Li, R. and Ashgriz, N. (2006). Characteristics of liquid sheets formed by two impinging jets. *Physics of Fluids (1994-present)*, 18(8):087104.

Li, X.-Z., Walker, B., and Michaelides, A. (2011). Quantum nature of the hydrogen bond. *Proceedings of the National Academy of Sciences*, 108(16):6369–6373.

Lin, S. and Lian, Z. (1990). Mechanisms of the breakup of liquid jets. *AIAA Journal*, 28(1):120–126.

Lueg, J. (2014). *Dielektrische und rheologische Untersuchungen an Monoalkoholen mit Debye-Prozess*. TU Dortmund.

MacCallum, J. L. and Tieleman, D. P. (2002). Structures of neat and hydrated 1-octanol from computer simulations. *Journal of the American Chemical Society*, 124(50):15085–15093.

Manninen, S. and Hämäläinen, K. (1992). High-resolution inelastic x-ray scattering study of the boron k absorption edge. *Physical Review B*, 45(7):3878.

Matisz, G., Kelterer, A.-M., Fabian, W. M., and Kunsági-Máté, S. (2011). Application of the quantum cluster equilibrium (qce) model for the liquid phase of primary alcohols using b3lyp and b3lyp-d dft methods. *The Journal of Physical Chemistry B*, 115(14):3936–3941.

Mizuno, Y. and Ohmura, Y. (1967). Theory of x-ray raman scattering. *Journal of the Physical Society of Japan*, 22(2):445–449.

Morineau, D. and Alba-Simionesco, C. (1998). Hydrogen-bond-induced clustering in the fragile glass-forming liquid m-toluidine: Experiments and simulations. *The Journal of Chemical Physics*, 109(19):8494–8503.

Murthy, S. and Tyagi, M. (2002). Experimental study of the high frequency relaxation process in monohydroxy alcohols. *The Journal of Chemical Physics*, 117(8):3837–3847.

Nagasawa, H., Mourikis, S., and Schülke, W. (1989). X-ray raman spectrum of li, be and graphite in a high-resolution inelastic synchrotron x-ray scattering experiment. *Journal of the Physical Society of Japan*, 58(2):710–717.

Narten, A. and Habenschuss, A. (1984). Hydrogen bonding in liquid methanol and ethanol determined by x-ray diffraction. *The Journal of Chemical Physics*, 80(7):3387–3391.

Nielsen, A. I., Christensen, T., Jakobsen, B., Niss, K., Olsen, N. B., Richert, R., and Dyre, J. C. (2009). Prevalence of approximate t relaxation for the dielectric $\alpha$ process in viscous organic liquids. *The Journal of Chemical Physics*, 130(15):154508.

Nilsson, A., Nordlund, D., Waluyo, I., Huang, N., Ogasawara, H., Kaya, S., Bergmann, U., Näslund, L.-Å., Öström, H., Wernet, P., et al. (2010). X-ray absorption spectroscopy and x-ray raman scattering of water and ice; an experimental view. *Journal of Electron Spectroscopy and Related Phenomena*, 177(2):99–129.

Nowak, B., Paulus, M., Nase, J., Salmen, P., Degen, P., Wirkert, F. J., Honkimaki, V., and Tolan, M. (2016). Solid-supported lipid multilayers under high hydrostatic pressure. *Langmuir*, 32(11):2638–2643.

Otendal, M., Hemberg, O., Tuohimaa, T., and Hertz, H. M. (2005). Microscopic high-speed liquid-metal jets in vacuum. *Experiments in Fluids*, 39(5):799–804.

Pauling, L. and Corey, R. B. (1951). Configurations of polypeptide chains with favored orientations around single bonds two new pleated sheets. *Proceedings of the National Academy of Sciences*, 37(11):729–740.

Pauling, L., Corey, R. B., and Branson, H. R. (1951). The structure of proteins: two hydrogen-bonded helical configurations of the polypeptide chain. *Proceedings of the National Academy of Sciences*, 37(4):205–211.

Pawlus, S., Wikarek, M., Gainaru, C., Paluch, M., and Böhmer, R. (2013). How do high pressures change the debye process of 4-methyl-3-heptanol? *The Journal of Chemical Physics*, 139(6):064501.

Pierce, W. and MacMillan, D. (1938). X-ray studies on liquids: the inner peak for alcohols and acids. *Journal of the American Chemical Society*, 60(4):779–783.

Ponchut, C., Rigal, J., Clément, J., Papillon, E., Homs, A., and Petitdemange, S. (2011). Maxipix, a fast readout photon-counting x-ray area detector for synchrotron applications. *Journal of Instrumentation*, 6(01):C01069.

Preuß, M., Gainaru, C., Hecksher, T., Bauer, S., Dyre, J., Richert, R., and Böhmer, R. (2012). Experimental studies of debye-like process and structural relaxation in mixtures of 2-ethyl-1-hexanol and 2-ethyl-1-hexyl bromide. *The Journal of Chemical Physics*, 137(14):144502.

Pylkkänen, T., Lehtola, J., Hakala, M., Sakko, A., Monaco, G., Huotari, S., and Hamalainen, K. (2010). Universal signature of hydrogen bonding in the oxygen k-edge spectrum of alcohols. *The Journal of Physical Chemistry B*, 114(41):13076–13083.

Reiser, A., Kasper, G., Gainaru, C., and Böhmer, R. (2010). Communications: High-pressure dielectric scaling study of a monohydroxy alcohol. *The Journal of Chemical Physics*, 132(18):181101.

Roger Eckert, R. A. (2002). Tierphysiologie. *Georg Thieme Verlag*, Ausgabe 4:47.

Sagawa, K., Lie, R. K., and Schaefer, J. (1990). Translation of otto frank's paper "die grundform des arteriellen pulses" zeitschrift für biologie 37: 483–526 (1899). *Journal of Molecular and Cellular Cardiology*, 22(3):253–254.

Sahle, C. J., Henriquet, C., Schroer, M., Juurinen, I., Niskanen, J., and Krisch, M. (2015a). A miniature closed-circle flow cell for high photon flux x-ray scattering experiments. *Journal of Synchrotron Radiation*, 22(6).

Sahle, C. J., Mirone, A., Niskanen, J., Inkinen, J., Krisch, M., and Huotari, S. (2015b). Planning, performing and analyzing x-ray raman scattering experiments. *Journal of Synchrotron Radiation*, 22(2):400–409.

Sahle, C. J., Sternemann, C., Schmidt, C., Lehtola, S., Jahn, S., Simonelli, L., Huotari, S., Hakala, M., Pylkkänen, T., Nyrow, A., et al. (2013). Microscopic structure of water at elevated pressures and temperatures. *Proceedings of the National Academy of Sciences*, 110(16):6301–6306.

Sarnitskiy, G. (2015). *Lennard-Jones Radial Distribution Function*. Wikimedia Commons, Creative Commons Attribution-Share Alike 3.0 Unported.

Savart, F. (1833). Mémoire sur le choc d'une veine liquide lancée contre un plan circulaire. *Annales de Chimie et de Physique*, 54(56):1833.

Schülke, W. (1991). Inelastic scattering by electronic excitations. *Handbook of Synchrotron Radiation*, 3:565.

Schülke, W., Berthold, A., Kaprolat, A., and Güntherodt, H.-J. (1988). Evidence for interlayer band shifts upon lithium intercalation in graphite from inelastic x-ray scattering. *Physical Review Letters*, 60(21):2217.

Shmyt'ko, I., Jiménez-Riobóo, R., Hassaine, M., and Ramos, M. (2010). Structural and thermodynamic studies of n-butanol. *Journal of Physics: Condensed Matter*, 22(19):195102.

Sillrén, P., Bielecki, J., Mattsson, J., Börjesson, L., and Matic, A. (2012). A statistical model of hydrogen bond networks in liquid alcohols. *The Journal of Chemical Physics*, 136(9):094514.

Singh, L. P., Alba-Simionesco, C., and Richert, R. (2013). Dynamics of glass-forming liquids. xvii. dielectric relaxation and intermolecular association in a series of isomeric octyl alcohols. *The Journal of Chemical Physics*, 139(14):144503.

Singh, L. P. and Richert, R. (2012). Watching hydrogen-bonded structures in an alcohol convert from rings to chains. *Physical Review Letters*, 109(16):167802.

Skinner, E. W. (1930). Diffraction of x-rays in liquids: Effect of temperature. *Physical Review*, 36(11):1625.

Sternemann, C. and Wilke, M. (2016). Spectroscopy of low and intermediate z elements at extreme conditions: in situ studies of earth materials at pressure and temperature via x-ray raman scattering. *High Pressure Research*, 36(3):275–292.

Sternemann, H., Sternemann, C., Seidler, G., Fister, T., Sakko, A., and Tolan, M. (2008). An extraction algorithm for core-level excitations in non-resonant inelastic x-ray scattering spectra. *Journal of Synchrotron Radiation*, 15(2):162–169.

Stewart, G. and Morrow, R. M. (1927). X-ray diffraction in liquids: primary normal alcohols. *Physical Review*, 30(3):232.

STIL (1995). Chromatic confocal sensing. `http://www.stilsa.com/EN/prin.htm`.

Tamenori, Y., Okada, K., Takahashi, O., Arakawa, S., Tabayashi, K., Hiraya, A., Gejo, T., and Honma, K. (2008). Hydrogen bonding in methanol clusters probed by inner-shell photoabsorption spectroscopy in the carbon and oxygen k-edge regions. *The Journal of Chemical Physics*, 128(12):124321.

Taylor, G. (1959). The dynamics of thin sheets of fluid. part i-water bells. In *Proceedings of the Royal Society of London A*, volume 253, pages 289–295.

Tomsic, M., Jamnik, A., Fritz-Popovski, G., Glatter, O., and Vlcek, L. (2007). Structural properties of pure simple alcohols from ethanol, propanol, butanol, pentanol,

to hexanol: comparing monte carlo simulations with experimental saxs data. *The Journal of Physical Chemistry B*, 111(7):1738–1751.

Trabelsi, S., Hammami, F., Nasr, S., and Bellissent-Funel, M.-C. (2008). Neutron and x-ray scattering experiments on fully deuterated liquid n-methylacetamide cd 3 condcd 3 at various temperatures and under pressure. *Journal of Molecular Structure*, 891(1):388–395.

Vahvaselkä, K., Serimaa, R., and Torkkeli, M. (1995). Determination of liquid structures of the primary alcohols methanol, ethanol, 1-propanol, 1-butanol and 1-octanol by x-ray scattering. *Journal of Applied Crystallography*, 28(2):189–195.

Verbeni, R., Pylkkänen, T., Huotari, S., Simonelli, L., Vanko, G., Martel, K., Henriquet, C., and Monaco, G. (2009). Multiple-element spectrometer for non-resonant inelastic x-ray spectroscopy of electronic excitations. *Journal of Synchrotron Radiation*, 16(4):469–476.

Vij, J., Scaife, W., and Calderwood, J. (1981). The pressure and temperature dependence of the complex permittivity of heptanol isomers. *Journal of Physics D: Applied Physics*, 14(4):733.

Vrhovšek, A., Gereben, O., Jamnik, A., and Pusztai, L. (2011). Hydrogen bonding and molecular aggregates in liquid methanol, ethanol, and 1-propanol. *The Journal of Physical Chemistry B*, 115(46):13473–13488.

Wang, J., Sagar, R. P., Schmider, H., and Smith, V. (1993). X-ray elastic and inelastic scattering factors for neutral atoms z= 2-92. *Atomic Data and Nuclear Data Tables*, 53(2):233–269.

Wang, L.-M. and Richert, R. (2005). Debye type dielectric relaxation and the glass transition of alcohols. *The Journal of Physical Chemistry B*, 109(22):11091–11094.

Wang, L.-M., Shahriari, S., and Richert, R. (2005). Diluent effects on the debye-type dielectric relaxation in viscous monohydroxy alcohols. *The Journal of Physical Chemistry B*, 109(49):23255–23262.

Warren, B. E. (1969). *X-ray Diffraction*. Addison-Wesley Publishing Company.

Watson, J. D., Crick, F. H., et al. (1953). Molecular structure of nucleic acids. *Nature*, 171(4356):737–738.

Weitkamp, T., Neuefeind, J., Fischer, H., and Zeidler, M. (2000). Hydrogen bonding in liquid methanol at ambient conditions and at high pressure. *Molecular Physics*, 98(3):125–134.

Wilding, M. C., Wilson, M., Alderman, O. L., Benmore, C., Weber, J., Parise, J. B., Tamalonis, A., and Skinner, L. (2016). Low-dimensional network formation in molten sodium carbonate. *Scientific Reports*, 6.

Yamaguchi, T., Benmore, C., and Soper, A. (2000). The structure of subcritical and supercritical methanol by neutron diffraction, empirical potential structure refinement, and spherical harmonic analysis. *The Journal of Chemical Physics*, 112(20):8976–8987.

Yaws, C. L. (2014). *Thermophysical Properties of Chemicals and Hydrocarbons*. Elsevier Inc.

Zetterström, P., Dahlborg, U., and Howells, W. (1994a). A systematic study of the structure of liquid iso-propanol by time-of-flight neutron diffraction. *Molecular Physics*, 81(5):1187–1204.

Zetterström, P., Dahlborg, U., and Wannberg, A. (1994b). Structural studies of liquid 2-bromopropane and 2-chloropropane by neutron diffraction. *Molecular Physics*, 83(5):971–981.

Zewail, A. H. (2000). Femtochemistry. past, present, and future. *Pure and Applied Chemistry*, 72(12):2219–2231.

# Acknowledgment

## Eidesstattliche Erklärung

Hiermit erkläre ich an Eides Statt, dass ich die vorliegende Arbeit ausschließlich unter Anleitung meiner wissenschaftlichen Betreuer und Verwendung der angegebenen Hilfsmittel angefertigt habe. Ich habe keine anderen als die angegebenen Quellen und Hilfsmittel benutzt sowie wörtliche und sinngemäße Zitate kenntlich gemacht. Die Arbeit wurde weder ganz noch in Teilen an anderer Stelle im Rahmen eines Prüfungsverfahrens vorgelegt.

_____          _____
Ort, Datum                                Unterschrift